NeuroD1-Based Therapeutic Strategies for Acquired Brain Injuries and Novel Neuroimaging Techniques

A Dissertation Submitted to the Faculty of the Graduate School of Minnesota By

Isaac Heath Clark

In Partial Fulfillment of the Requirements for the Degree of Doctor of Philosophy

Advisor: Walter Low, PhD
Co-Advisor: Andrew Grande, MD

March, 2025

Acknowledgements

I would like to thank my advisors Walter Low, PhD and Andrew Grande, MD for persistent encouragement and support of my journey through countless struggles. I must also thank my labmates for providing valuable insights to my research and much needed mental breaks. Lastly, for continually supporting and challenging me to further my research and personal understanding, I would like to thank my committee members R. Scott McIvor, PhD, Wei Chen, PhD, and Wei Shen, PhD.

Dedication

This dissertation is dedicated to my loving parents. They have been in my corner even before I knew I had a love of science and engineering. Every small step, I knew they would be there to help in any way they could. I know that they have always been proud of me, and it's taken a long time, but I’m proud of me too.

Abstract

Acquired Brain Injuries (ABI) affect millions of people each year and often lead to long term neurological deficits with little to no treatment options. NeuroD1 is a transcription factor that has potential treatment applications for ABI's. We sought to explore its effectiveness in traumatic brain injury (TBI) and stroke models and found enhanced neurological recoveries. The routes used to study these injuries however, can often be inefficient and inaccessible to many labs. As such, we developed pipelines to improve efficiency of TBI lesion quantification and improve accessibility of whole brain connectome analysis.

Table of Contents:

List of Tables

List of Figures

Chapter 1. Introduction:

1.1 Acquired Brain Injury:

Acquired brain injury (ABI) is a blanket term that covers any brain injury acquired after birth. This includes injuries that occur due to an outside factor such as external trauma, and injuries that occur due to internal factors such as stroke, neoplasm, infection, and anoxia. (Feigin, Valery L., et al. 2010), (Goldman, Liam, et al. 2022). As ABI's cover a wide array of injuries, not all forms of it are recorded as hospital visits, some get lumped in with other forms of injuries, and overall statistics can vary greatly from source to source. Two of the most prevalent forms of ABI in the USA are traumatic brain injury, which result in an estimated 2.8 million incidences per year, and stroke, which over 795,000 people sustain each year (Taylor, Christopher A. 2017), (Tsao CW, Aday AW, Almarzooq ZI, et al. 2023).

1.2 ABI Importance:

These injuries can often result in neurological deficits ranging from sensory impairment, motor deficits, personality changes, loss of memory, to reduced ability to concentrate. These all significantly impact an individual's quality of life and can also place an emotional, physical, and/or financial strain on their loved ones. As these conditions can affect millions of people over time, it poses a burden to society as well. Healthcare systems must allocate substantial resources for treatment and rehabilitation, while workplaces and communities face challenges in supporting those affected. From a moral and societal perspective, it is imperative that we develop better treatment, diagnosis, and prevention methods for these injuries.

Researching ABIs and how to treat, diagnose, and prevent them, are main focuses of the scientific community. ABIs can affect the brain in different ways depending on their location, severity, type, duration, and various other factors. Understanding why particular

injuries lead to specific deficits, advances the field of neuroscience and ultimately assists in giving us a better understanding of the brain as a whole. In this thesis, we sought to explore treatment options for ABI and expand upon existing analysis methods used to assess its severity and progression.

Chapter 2. Background & Significance

2.1 ABI Recovery:

Depending on the type of injury, the brain can recover through varying levels and forms of neuroplasticity. Neuroplasticity is the ability of the brain to adjust, grow, and change its neural networks over time (Johnson, Brian P., and Leonardo G. Cohen. 2023). Neuroplasticity occurs through structural and functional changes in the brain. These changes can vary from molecular and synaptic changes to cellular adjustments and broader network reorganizations (Su, YouRong Sophie, et al. 2016). My thesis focused on cellular and broader network reorganizations.

On the network level, the injured brain areas will experience disruption of their axonal fiber tracts and functional connectivity. Methods that can assess changes to these networks are useful for diagnosis. In this thesis, we sought to expand upon the methods used to assess neural networks and make them more accessible to researchers. On the cellular level, neurogenesis serves as a method for regeneration. This process is believed to primarily occur in the sub ventricular zones and dentate gyrus of the hippocampus (Paredes, Mercedes F., et al. 2015). The full extent of its abilities are not yet well understood, but it is believed to be severely limited, with damage further away from the lateral ventricles being too far to benefit from the process. As such, treatments that could assist these spatially further damaged brain areas on a cellular level, could be of great benefit. We sought to study the delivery of the transcription factor NeuroD1 for the purpose of neuroprotection and cellular reprogramming in TBI and Stroke models.

2.2 NeuroD1 for NeuroProtection & Cell Reprogramming:

NeuroD1 is a transcription factor protein, able to modulate the expression of genes involved in the development and maturation of neuronal cells (Gao, Zhengliang, et al.

2009). It has been proposed as a potential treatment method for neuronal damage. Current literature suggests that NeuroD1 is responsible for the regulation of neurotrophin receptors, and regulation of cytoskeletal rearrangement (Kim, Woo-Young, et al. 2001) (Seo, Seongjin, et al. 2007). These both can assist in development of axons, dendrite growth, and synapse formation. If expressed in damaged endogenous neurons, it can promote axonal regeneration and even functional recovery (Lai, Muhua, et al. 2020). This gives it potential for use as a neuroprotective treatment of conditions that damage neuronal tissues.

Additionally, if expressed in non-neuronal cells such as astrocytes, it has the potential to be used as a cell reprogramming therapy, in which the astrocytes are reprogrammed into neuronal cells (Clark, Isaac H., et al. 2022). Astrocytes are the largest population of glial cells, which are very prevalent throughout the brain with an average ratio of 1.4 glial cells for every neuron in humans (Herculano-Houzel, Suzana. 2014). The astrocyte population is replenished through radial glia in the ventricular zone, progenitors in the subventricular zone, and local proliferation of differentiated astrocytes (Ge, Woo-Ping, et al. 2012). Proliferation of glial cells occurs regularly, and is greatly increased in response to injury (Dimou, Leda, and Magdalena Götz. 2014). Due to this cell population's prevalence throughout the brain, and their rapid proliferation in response to injury, it is an optimal target for reprogramming. In cases where the damage to neuronal cells is too severe for neuroprotection, cell reprogramming provides an alternative to restore the damaged tissue.

2.3 AAV Gene Delivery:

One method of delivery for NeuroD1 to neurons and/or astrocytes is using an Adeno Associated Viral (AAV) vector. AAV is a dependovirus capable of delivering single

stranded DNA to a cell, but incapable of replication without a helper virus (Carter, Barrie J. 2004). Normally, these viruses contain single stranded DNA including Cap and Rep genes necessary for their capsid formation and partial replication. These viruses can be engineered to form without the Rep and Cap genes inside, making them incapable of replication even with the presence of a helper virus. This makes them a safe method to transduce cells with little risk of killing the cell and no risk of replicating and spreading. During production, if the desired gene(s) are flanked by inverted terminal repeats within a plasmid and then introduced, these viruses can be engineered to deliver specific genes such as NeuroD1 for therapeutic purposes, provided the gene is 4.7 kilobases or less to fit within the capsid.

2.4 Cell Reprogramming Conflict:

If the concentration of AAV delivered is too high, it can become toxic to the transduced cells and promote cell death, as such careful consideration is needed when determining optimal delivery parameters (Hordeaux, Juliette, et al. 2020). Excessive levels of AAV, overexpression of the delivered genes, and consequential cell death can lead to apparent off target transduction. This has led to some conflict in the field of cell reprogramming, whether cell reprogramming is truly occurring in the first place, and if it is truly beneficial. We sought to explore this and verify prior literature by testing the transduction specificity of varying levels of AAV and the anatomical and neurological effects of varying levels of AAV mediated delivery of NeuroD1.

2.5 Traumatic Brain Injury:

Traumatic brain injury (TBI) is a form of ABI that is induced by some external event. Some of the most common events that cause TBI are external impacts to the head, rapid acceleration and deceleration resulting in the brain impacting the inside of the skull, or a

shockwave due to an explosion. These injuries can vary greatly in severity, and one assessment used to evaluate them within the first 24 hours is the Glasgow Coma Scale (GCS), which scores them on a scale of 3-15 (Jain, Shobhit, and Lindsay M. Iverson. 2025). The severity is typically divided into 3 categories: Mild TBI with a GCS score of 13-15, Moderate TBI with a GCS score of 9-12, and Severe TBI with a GCS score of <9 (Steyerberg, Ewout W., et al. 2008). Mild TBI is the most common by far, accounting for 81% of TBI diagnosed individuals and resulting in permanent disability ~10% of the time, while moderate TBIs occur in 11.04% and result in permanent disability ~66% of the time, and severe TBIs occur in 7.95% and result in permanent disability ~100% of the time (Dewan, Michael C., et al. 2018) (Frey, Lauren C. 2003). For our studies, we focused on moderate TBI, as that model allowed for easily detectable neurological, anatomical, and cellular differences between sham and injured models while not significantly increasing mortality rate. In this thesis we sought to explore the use of NeuroD1 as a neuroprotection and cellular reprogramming treatment for TBI.

2.6 TBI Primary Injury:

All of the varying severity levels of TBI can result in physical deformation of the brain that can cause permanent damage. The physical deformation directly results in a primary injury, which can consist of hematomas (pooling of blood, typically due to broken blood vessels) in the epidural, subdural, or cortical areas, microvascular injuries (weakening or breaks in blood vessel walls), and damaged or sheared neurons (Mechanical stretching/compressing resulting in altered structure and/or broken axons) (Najem, Dema, et al. 2018).

2.6.1 TBI Primary Injury Cellular Response:

Mechanical stress on a neuron can disrupt the structure of its cytoskeleton resulting in protein breakdown (proteolysis) and/or shearing of the axon (Mesfin, Fassil B., et al. 2025). Proteolysis of proteins can lead to various secondary injuries or even long term diseases as a result of altered signal cascades. If the mechanical stress is great enough, the axon of a neuron will tear completely and become sheared. This shearing can lead to secondary injuries such as axonal degeneration and neuronal cell death.

2.7 TBI Secondary Injury:

Primary injuries caused by TBI can influence and prompt the occurrence of secondary injuries, which further degrade the tissue. Secondary injuries would include exacerbated immune response, toxic levels of excitatory molecules (Excitotoxicity), proteolysis, axonal degeneration and cell death, cerebral edema, and hydrocephalus (Mckee, Ann C., and Daniel H. Daneshvar., 2015).

2.7.1 TBI Secondary Injury Inter-Cellular Response:

An intensified immune response in the brain can promote the proliferation of more activated astrocytes and microglia which can introduce an excess of proinflammatory cytokines, reactive oxygen intermediates, proteinases and complement proteins which can all be toxic to cells (Dheen, S. Thameem, et al. 2007). Additionally, an excess of activated microglia can inhibit regrowth of brain tissue via the formation of a glial scar and upregulation of myelin-associated inhibitory factors (Yiu, Glenn, and Zhigang He. 2006).
In some cases, the glial cells are unable to clear the excitatory molecules in an area. In addition to the extra release of excitatory molecules from dying neurons, this leads to a buildup of said molecules. These molecules then lead to excessive activation of the

glutamate receptors which prompts excessive influx of calcium ions which interferes with numerous cell processes and leads to cell death (Bangar, Annu, et al. 2024).

2.7.2 TBI Secondary Injury Intra-Cellular Response:

A neuron's ability to regenerate its axon post injury is largely dependent on its subtype and location, with peripheral nervous system neurons commonly possessing the ability to regrow their axons, and central nervous system neurons commonly not possessing the ability (Wang, Fei, et al. 2023). If a neuron is unable to regenerate or reconnect with the portion of the axon separated from its cell body, that separated portion will typically degrade via Wallerian Degeneration, a process by which the axon is fragmented and the fragments are broken down and cleared by immune and glial cells (Conforti, Laura, et al. 2014). This permanently severs the direct connection that previously existed and can result in neurological deficits. If the neuron's cell body survives, it may form new connections with neighboring cells, allowing indirect pathways to develop and aiding neurological recovery through brain plasticity. In many cases however, the cell body will die as a result of the mechanical damage. In these cases, often calcium influx through the severed axon may activate apoptosis which will degrade the cytoskeleton of the cell and kill it. Neurological deficits from neuron death may be compensated for through brain plasticity and new pathway formation, but the loss of neuronal cells is typically permanent.

2.8 TBI Lesions:

The various forms of damage caused by TBI can result in a physical loss of tissue or lesion that is visible on the brain. The size and location of this lesion can be used to further assess the severity of the TBI and its potential impact on neurological function, guiding prognosis and treatment strategies. Current research methods often assess the lesion size in animal models through processes such as cryosectioning/staining or MRI scans.

These methods however can be time and resource intensive. In this thesis, we sought to find more efficient alternatives to these methods to expedite the research process.

2.9 TBI Neurological Deficits & Network Alterations:

Depending on the TBI location and severity, the severity and type of network alterations and neurological impairments will vary. Typically, impacted areas will experience abnormalities such as interruption or degradation of their axonal fiber tracts (Hayes, Jasmeet P., et al. 2016). Areas that have long bundles of axons connecting hemispheres, such as the corpus callosum and fornix, are more likely to experience these issues than others. In terms of functional connectivity, interestingly, increases and decreases can be observed in various regions post TBI. Specifically, studies have shown both posterior cingulate cortex and precuneus regions experienced reduced functional connectivity, while regions such as the thalamus, hippocampus, amygdala, and frontal lobe experienced increases in functional connectivity (Iraji, Armin, et al. 2015). These can result in various neurological deficits, such as cognitive impairments, to motor/sensory impairments, to emotional and behavioral changes. For this thesis project, we focused on motor impairments, as TBI models that reliably produced these deficits already existed, and methods to analyze the progression and recovery from these deficits were easily accessible in our lab.

2.10 Stroke:

Stroke is another form of ABI, that is induced from internal events rather than external. Stroke can be categorized as ischemic stroke in which blood flow is blocked often due to a blood clot, or hemorrhagic stroke in which bleeding occurs in the brain often due to a ruptured blood vessel (Knight-Greenfield, Ashley, et al. 2019). Both of these conditions lead to a lack of proper blood flow to some region of the brain, which leads to tissue death

in that area. For this thesis project, we focused on ischemic stroke and sought to explore the use of NeuroD1 as a cell reprogramming treatment in stroke models. At the time of our research conduction, this therapy has been explored by other labs for the treatment of stroke models in mice and rats. Mouse models provide an easily accessible model that are genetically similar to humans, cost effective, provide a quick experimental timeline, have extensive prior literature researching their neuroanatomy, and have numerous established models for various ABIs. Canine models on the other hand are not as easily accessible, but provide an advantage of having brain vasculature more similar to humans. This makes them a more translatable stroke model of cerebral ischemia for human trials. We sought to explore the use of NeuroD1 cell reprogramming specifically in canine stroke models to further visualize how the treatment may function in humans.

2.11 Ischemic Stroke:

Ischemic stroke can be a result of numerous things, with the most common being large artery atherosclerosis (buildup of plaque in major vessels), or cardioembolic (lodging of a blood clot, originating from the heart, in major vessels) (Knight-Greenfield, Ashley, et al. 2019). When a vessel is occluded in the brain, the downstream brain regions experience ischemia. Depending on how long the blood flow is prevented, the level of damage can vary significantly. On a cellular level, irreversible damage from ischemia can occur as early as 30 minutes (Ames, A., and F. B. Nesbett. 1983). On a neurological functionality level, every additional hour from stroke onset to reperfusion was associated with a 7.7% decreased probability of functional independence (Mulder, Maxim J. H. L., et al. 2018). Reperfusion therapy is an early intervention treatment in which the offending blockage is removed by medicinal or mechanical means (Widimsky, Petr, et al. 2022). If no early treatments are administered, the ischemic area may eventually have some blood flow

restored through collateral circulation, in which alternative unblocked vessels provide additional blood flow, or angiogenesis of new vessels into the ischemic area. The brain may still recover some neurological functionality through brain plasticity.

2.12 Stroke Neurological Deficits:

Similar to TBI, the type of neurological deficits that stroke victims can experience vary depending on the stroke location and severity. For this thesis study, we focused on moderate stroke in the cortex regions supplied by the distal middle cerebral artery such as the primary motor and somatosensory cortical areas. These would induce motor and sensory deficits that could be assessed with the resources and personnel accessible in our lab.

2.13 Brain Connectome:

One method to study acquired brain injuries is to analyze their effect on functional connectivity within the brain. Functional connectivity is defined as the temporal correlation of neurophysiological events between distinct brain regions (Friston, Karl J. 1994). This means, if two distinct regions of the brain have similar patterns of activity and inactivity over time, they can be considered functionally connected. Higher levels of blood oxygen have been correlated with increased brain activity in that region. As such brain activity can be detected by blood oxygenation levels. If brain activity is recorded throughout various regions of the brain, those regions can be correlated against each other to generate a brain connectome, describing the functional connectivity throughout the brain. The most prevalent method for detecting blood oxygenation levels in the brain for the purpose of determining functional connectivity is through the use of functional magnetic resonance imaging (fMRI). fMRI however, is not accessible to all researchers as it is expensive, requires significant space, and experienced personnel. Photoacoustic ultrasound (PAU)

is a much more accessible technology that can also be used to detect blood oxygenation levels. This method has been used to visualize functional connectivity, however its use has thus far been limited to single coronal slice analysis. We sought to expand this and develop methods to visualize connectivity of the entire brain using PAU.

Chapter 3: NeuroD1 Delivery in Mouse TBI Models

3.1 Introduction:

This chapter was adapted from a manuscript in progress. Traumatic brain injury (TBI) remains a leading cause of morbidity and mortality worldwide (Maas, Andrew I R et al. 2017). This has prompted various investigations into potential therapeutic options. TBI is inflicted by external trauma to the head, which over time yields dysfunction in brain activity. This condition has two mechanisms as part of its pathophysiology: the primary mechanism that occurs at the time of insult and the secondary mechanism that involves a cascade of immunological processes that exacerbates tissue damage over time. Therapeutic options mostly focus on symptomatic management, rehabilitation, surgical or thrombolytic therapy, mechanical thrombectomy, and rehabilitation.

NeuroD1 is a transcription factor that plays a crucial role in the development and differentiation of neuronal cells, and has been proposed as a potential treatment for neuronal tissue damage in brain injuries (Gao, Zhengliang et al. 2008). Studies have shown that NeuroD1 may have the potential to reprogram non-neuronal cells such as astrocytes into functional neurons. This reprogramming could offer a novel approach for repairing damaged neuronal tissues in TBI (Liu, Hong, et al. 2008). However, controversy exists regarding reprogramming capabilities and optimal therapeutic concentrations. It is unclear whether these beneficial effects are primarily due to cellular reprogramming or due to other confounding factors.

While some studies have demonstrated its efficacy in neuronal protection, others have suggested a potential for cellular reprogramming (Matsuda-Ito, Kanae et al. 2022; Chen, Yu-Chen, et al. 2020; Ma, Ning-Xin et al. 2022). The controversy surrounding NeuroD1's role in cellular reprogramming versus neuroprotection poses challenges in determining the optimal concentrations for therapeutic efficacy (Guillemot, François, and

Bassem A Hassan. 2017). Balancing neuroprotection with reprogramming potential is crucial to maximizing NeuroD1 therapeutic benefits in TBI (Falk, Sven, and Magdalena Götz. 2017). This study aimed to examine the existing methods of NeuroD1 delivery in TBI models, explore the effect of virus dose on transduction specificity, and deduce the potency of each variation and where future directives can proceed.

3.2 Methods:

3.2.1 Animals:

All animals in this project were C57BL/6 mice. Animals in the neuroprotection in TBI model experiments were male aged 3-6 months. Animals in the astrocyte to neuron reprogramming with high dose in TBI model experiments were evenly split male/female and aged 3-6 months. Animals in the alternate dose transduction experiment were male aged 2-4 months. Animals in the astrocyte to neuron reprogramming with low dose in TBI model experiment were evenly split male/female and aged 2-4 months.

3.2.2 Viruses:

3.2.2.1 AAV9-hSyn-NeuroD1-T2A-mRuby: 2.32E13 GC/mL:

This construct was designed to induce neuroprotection in endogenous neurons by delivering the genes for NeuroD1 and mRuby2 with a neuron specific promoter, enabling their expression within the cells. (Figure 3.1). Serotype 9 Adeno Associated Virus (AAV9) was chosen because of its ability to target delivery to both neuronal and non-neuronal cells (Issa, Shaza S., et al. 2023). Human Synapsin 1 gene promoter (hSyn) was chosen due to its demonstrated potency in promoting transgene expression in the corticospinal tract, targeting specific neuronal cells, both in vivo and in vitro, and its small size, which allows for larger coding sequences to be spliced in. Neurogenic differentiation factor 1

(NeuroD1) is a NeuroD transcription factor selected as a part of this virus due to its ability to initiate neuronal development and the reprogramming of various types of cells into neurons (Pataskar, Abhijeet, et al. 2016). T2A is a self-cleaving peptide from the 2A class of peptides, which allows the simultaneous promotion of NeuroD1 and mRuby2. Finally, mRuby was chosen as our red fluorescent protein which provided a biomarker to identify transduced cells (Kredel, Simone, et al. 2009).

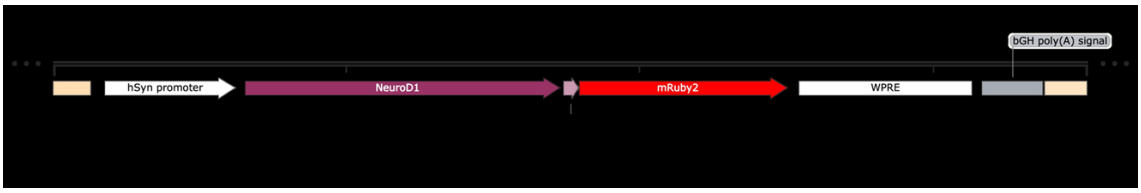

Figure 3.1: Transgene for Viral System. AAV9-hSyn-NeuroD1-T2A-mRuby.

3.2.2.2 AAV9-GFAP(short)-Cre: 2.4E13 GC/mL + AAV9-CAG-DIO-NeuroD1-T2A-mRuby2: 2.5E13 GC/mL:

These constructs were designed for the purpose of inducing cellular reprogramming in endogenous astrocytes (Figure 3.2). These were mixed evenly prior to injection. Glial fibrillary acidic protein promoter (GFAP) is a promoter sequence prior to the GFAP sequence. The GFAP protein is found commonly in astrocytes over other cell types, and as such, the GFAP promoter is more active in astrocytes. Cre recombinase (Cre) is a bacteria-derived, Type I Topoisomerase that can be used with LoxP to make site based genetic switches (Nagy A. 2000). Cre recombinase can be used for genetic modifications such as excising DNA segments or flipping sequences by mediating site-specific recombination between LoxP sites. To prevent unintended transcription, the genes of interest in the second vector were inverted within double-floxed inverted open reading frames (DIO). Cre recombinase would then flip the sequences into a readable orientation and subsequently remove the LoxP sites, locking the modification in place permanently.

The CAG promoter (CAG) was selected due to its capabilities in driving high amounts of expression in all mammalian cells (Dou, Yuanyuan, et al. 2020). CAG paired with the genetic switch, ensures that the genes of interest will continue to be expressed, regardless of the cell type and resulting regulation of the GFAP promoter. Without this switch, a cell identity change could reduce activity of the GFAP promoter, halting NeuroD1 production and potentially leading to partial reprogramming. NeuroD1 was included due to its potential in converting responsive glial cells into viable neurons in mouse brains (Guo, Ziyuan, et al. 2014). Finally, mRuby was added to this vector to allow its tracking and the identification of transferred cells.

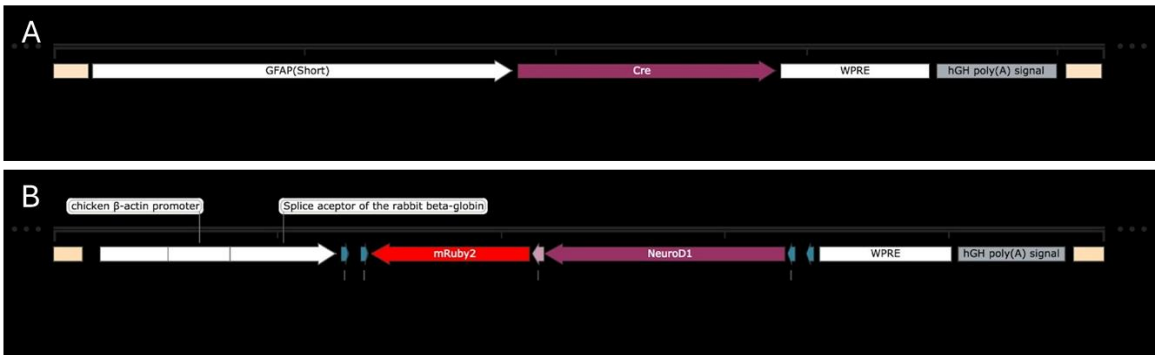

Figure 3.2: Transgenes for Viral System. A: AAV9-GFAP(short)-Cre. B: AAV9-CAG-DIO-NeuroD1-T2A-mRuby2.

3.2.2.3 AAV9-GFAP(short)-Cre: 2.4E13 GC/mL + AAV9-CAG-DIO--mRuby2: 1.0E13 GC/mL:

These constructs were designed for the purpose of marking endogenous astrocytes in the same manner as the sequences designed for reprogramming (Figure 3.2). These sequences were identical to those previously described with the exception of excluding NeuroD1. Allowing for transduction of the cells and marking, but no reprogramming.

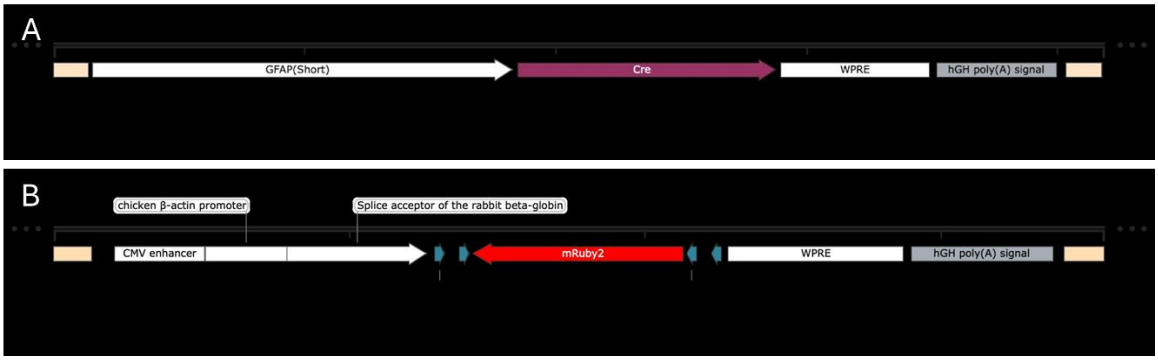

Figure 3.3: Transgenes for Viral System. A: AAV9-GFAP(short)-Cre. B: AAV9-CAG-DIO-mRuby2.

3.2.3 Surgeries:

3.2.3.1 Controlled Cortical Impact:

Surgeries began by prepping mice with an injection of slow-release Buprenorphine (2 mg/kg). After 2 hours, mice were placed into an anesthesia chamber (1.5–5% isoflurane) until fully anesthetized. In the meantime, the Leica Stereotaxic Impactor Control Unit (Model 39463920) was prepped by setting the velocity adjustment to 6 m/s (+/- 0.05), attaching the Lecia Stereotaxic Impactor Actuator to the stereotaxic arm, and then checking that the “retract,” “off,” “extend,” and “impact” functions are working properly. After being anesthetized, mice were then transferred to the surgical field, where ears, bars, and nose cones were secured and lubricants were applied to the eyes. Nair^{tm} hair removal and depilatory cream (active ingredients: potassium thioglycolate and calcium hydroxide) was applied to the heads of the mice for 1 minute. Nair^{tm} hair removal and depilatory cream were then wiped off with betadine and alcohol wipes. Anesthetic depth was then assessed through the pinch method. After confirming the unresponsiveness of the mice to pinches as a result of the anesthesia, incisions were made through the use of a scalpel to the skin of the mice in order to reveal bregma. A >2 mm diameter Craniectomy was then performed at M/L + 1.5mm and 0.5mm A/P. For all experiments prior to the low dose reprogramming

TBI experiment, baseline depth was established by setting the actuator to extend and visually confirming impactor tip contact with the brain. To improve TBI consistency, in the low dose reprogramming TBI experiment, an electronic contact sensor attachment for the impactor was used for confirmation of brain surface. After depth was established, TBI was generated through the controlled cortical impact with velocity 6 m/s, dwell time 100 ms, depth 1 mm, and probe diameter 2 mm. The previously incised skin was then sutured and/or stabled back to conceal the TBI-induced brain. The ear bars and nose cones were then removed, and the mice were placed in a cage with a heating pad underneath.

3.2.3.2 FluoroGold Injection:

Surgical preparation was the same as the TBI procedure. After completion of surgical preparation, the scalp was opened to reveal bregma, the stereotaxic mount was positioned at the coordinates M/L -1.5 and A/P +0.5 of bregma in the contralateral side of the targeted hemisphere. Next, 0.5uL of 2% FluoroGold and sterile saline solution was injected through the craniectomy using a stereotaxic Hamilton syringe at a depth of 1 mm and a rate of .5uL/min. The scalp was then closed with sutures and the animals were placed in their cages to recover.

3.2.3.3 Virus Injection:

Surgical preparation was the same as other surgical procedures. The injector rate and volume were set to 0.5 µL/min and 1.5 µL, respectively. After surgical preparation, incisions were made through the use of a scalpel to the skin of the mice in order to reveal their bregma. The impactor was then utilized to measure the bregma positioned M/L +/- 1.5 and A/P +0.5. The needle was progressively lowered onto the brain's surface, then further lowered to a depth of 2.5 mm into the brain, at which point 1.5 µL of the virus was injected. The needle was carefully raised to 1 mm, and another 1.5 µL of the virus was

injected. The needle and Hamilton syringe were then carefully withdrawn. The previously incised skin was then sutured and/or stabled.

3.2.4 Behavior:

3.2.4.1 Beam Walk:

The beam walk test was utilized to assess individual limb function in mice. We used 1 in and ¼ in thick rectangular beams with start and end markers 2ft apart. A bright light was positioned at one end of the beam, while a box was positioned on the other end. All mice were allowed to acclimate to the room for 30 minutes prior to the beginning of testing. Mice were further acclimated to the box at the end of the test for 15+ seconds before being placed on the far end near the bright light. Time to cross the start to end markers was recorded as well as foot faults for each animal. Foot faults were recorded as general and not specified for each foot. Each animal was given 4 trials per day to walk the length of the beam in 60 seconds or less. Baseline results were recorded for each mouse 7 days prior to any procedures.

3.2.4.2 Rotarod:

The rotarod test was used to assess neurological deficits. All mice were allowed to acclimate to the room for 30 minutes prior to the beginning of testing. Prior to performing this task, mice were trained for 3 days prior to injury. Each animal was given 4 trials per day and at least two minutes of recovery between each trial. Mice were tested on the day after the last training session. The test was performed over a period of one minute, with an acceleration of 4.0-60.0 RPM and a one second delay between accelerations. Results were recorded as the time it takes to fall.

3.2.5 Tissue Processing:

3.2.5.1 Tissue Fixation:

All mice were anesthetized using isoflurane and euthanized through perfusion with PBS and 4% PFA, then decapitated. After being removed, their brains were incubated in 4% PFA for 24 hours at 4°C. The next day, using a shaker, the brains were washed with PBS three times for five minutes each. The brains were incubated in 10% sucrose for 24 hours at 4°C to create a sucrose gradient. The brains were incubated in 20% sucrose for 24 hours at 4°C the next day. The brains were incubated in 30% sucrose for 24 hours at 4°C the last day.

3.2.5.2 Ultrasound Scan:

All brains were scanned using a Vevo 2100 Imaging System with a MS400 transducer attached via stereotaxic arm to a 3D acquisition motor. The brain was removed from the 30% sucrose, placed in a center well culture dish with ultrasound gel to further secure its position, and submerged in water. The transducer was then positioned via the stereotaxic arm the rough anterior/posterior center of the brain and set to acquire a range of +/- 7mm with a step size of 0.1mm.

3.2.5.3 Tissue Cryosectioning:

The mice brains were embedded in OCT the next day, and 20 um thick brain cryo-sections were made using a Leica CM1850 cryostat. Sections were alternated between 10 different slides. Two sets of 10 slides were used per brain, allowing us to section from ~ + 3.2mm bregma to ~ -3.08mm bregma.

3.2.5.4 Tissue Staining:

Sections were dried for 10-30 minutes, permeabilized with PBST (0.3% Triton X-100) for 30 min, and blocked with 5% donkey serum for 45 min. After that, slices were incubated with primary antibodies against NeuroD1 (1:250 Abcam, ab205300), GFAP (1:500, Invitrogen, 13-0300), and NeuN (1:500, Abcam, ab177487) overnight at 4 °C in 5% donkey serum blocking solution. Sections were washed 3x5 min with PBST (0.1% Triton X-100), then incubated with secondary antibodies labeled with Alexa Fluor 488, 555, or 647 (1:1000, Abcam) and DAPI (1:1000) in 5% donkey serum for 1 hour. Sections were rinsed 3x5 min with PBS. Following the final rinsing, the slices were wet mounted and imaged using a Leica DMI6000 B microscope.

3.2.6 Tissue Quantification:

3.2.6.1 TBI Lesion Quantification:

To quantify TBI lesion volumes, 3D Slicer (Fedorov, Andriy, et al. 2012) was used on the ultrasound brain scans. The values for image spacing were 0.0890 mm (165), 0.0189 mm (1204), and 0.0204 mm (988). Segment Editor was used to segment the images. To distinguish between various regions, two segmentations were introduced. Segment 1 was intended to depict the outline of the brain, whereas Segment 2 was intended to include the region surrounding the brain. Every ten slides, Segments 1 and 2 were manually highlighted using the paintbrush tool. Initial segmentation was carried out using the ‘grow from seeds’ tool. The accuracy of the segmentation was double-checked to guarantee quality assurance. Both segments were smoothed using a factor of 0.3. Segment 2 was cropped so that the TBI region was the only area included. The segmentation was improved by performing slide-by-slide trimming. After sufficient trimming, the segmentation values were exported.

3.2.6.2 Ventricle Volume Quantification:

To determine ventricle volume, one glass slide series was tile scanned entirely using a single channel or brightfield. Each section in the series had its visible ventricles annotated using QuPath. The areas of those annotations were then multiplied by the section thickness and number of slides alternated to find the total volume.

3.2.6.3 Cell Quantification:

To determine co-labeling, we used QuPath software for analysis of the stained tissue sections (Bankhead, Peter, et al. 2017). Annotation areas were made around the entire tissue section or specific regions of interest. For cell detection, adjustments for cell size and intensity were made as needed. Single measurement classifiers were used to identify co-labeled cells, in which an appropriate threshold was chosen to identify the majority of co-labeled cells. After all classifiers were made, they were applied to allow for identification of all channel co-labeling.

3.2.7 Statistics:

In all cases comparing animals treated with NeuroD1 to control, single tailed t-tests were used, as the expected result was “better” results in treated groups. In all cases comparing males to females, two tailed t-tests were used, as no differences were expected. In cases comparing differences between alternate dose co-labeling, single tailed t-tests were used, as we had expected results based on prior literature.

3.3 Results:

3.3.1 Neuroprotection in TBI Mouse Models:

3.3.1.1 Experimental Design:

Research in this field is often challenged by the task of targeting specific cell types, such as astrocytes. There are several factors that can affect the specificity of transduction, including dose, lineage traced biomarkers, and even NeuroD1 itself. Consequently, many studies are shrouded with the uncertainty of whether they are indeed observing beneficial effects due to true reprogramming or neuroprotection. Some studies have specifically investigated NeuroD1-based neuroprotection such as Lai et al. which examined accelerated neuronal regeneration post-sciatic nerve injury when treated with a viral system using the synapsin promoter and NeuroD1 sequence (Lai, Muhua, et al. 2020). We designed an experiment to examine if this neuroprotection approach could provide benefits in TBI models. To explore this, we ordered the construction of AAV9-hSyn-NeuroD1-T2A-mRuby from the University of Minnesota Viral Vector and Cloning Core. To validate the ability of our virus to transduce endogenous neurons, we used FluoroGold and 3uL of AAV9-hSyn-NeuroD1-T2A-mRuby at a dose of 2.32E13 GC/mL in a group of 3 sham animals. For this preliminary experiment, a surgical procedure was performed to inject FluoroGold at day 0, an additional surgery was performed at day 2 to inject the virus, and the mice were euthanized at day 9 (Figure 3.4A). Tissue was then processed and stained with GFAP and NeuN. To validate transduction of endogenous neurons, analysis of co-labeling of NeuN, FluoroGold, and mRuby2 was conducted. After validating that the virus could transduce endogenous neurons, we induced TBI in four new mouse groups each originally with a sample size of 6 per group. One control group and one treatment group were scheduled for harvesting one week after injury, while another control group

and treatment group were scheduled for harvesting three weeks after injury (Figure 3.4B). In this experiment, induction of TBI and injection of the virus occurred in the same surgery. 3uL of the virus was injected at a dose of 2.32E13 GC/mL to transduce endogenous neurons and promote neuroprotection. Control groups were not injected with any variation of the virus or any control substances.

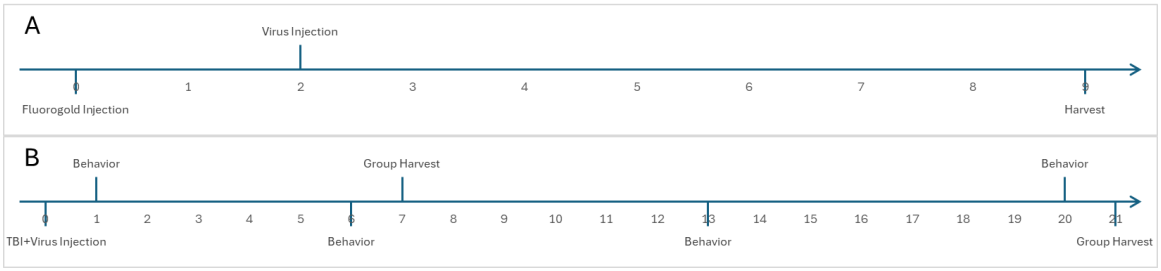

Figure 3.4: Timelines for Neuroprotection in TBI Experiments. A: FluoroGold Timeline. B: Neuroprotection TBI Timeline.

3.3.1.2 FluoroGold Co-Labeling:

FluoroGold has the ability to be traced retrogradely into neurons. Mice injected with FluoroGold will exhibit staining in many endogenous neurons within the injection site, as well as in regions containing neurons whose axons pass through the injected site (Naumann, Thomas, et al. 2000). When examining the mice from the sham group injected with both FluoroGold and our virus, it was noted, as expected, that a majority of the mRuby2 labeled cells were also co-labeled with NeuN (Figure 3.5). However, the FluoroGold did not label all neurons within that area, despite being injected at the same location as the virus. As result, only a small portion of mRuby2 cells were co-labled for both NeuN and FluoroGold. Nevertheless, as FluoroGold should only be present in

endogenous neurons, mRuby2 co-labeling with these FluoroGold positive cells validated the ability of this virus to transduce endogenous neurons.

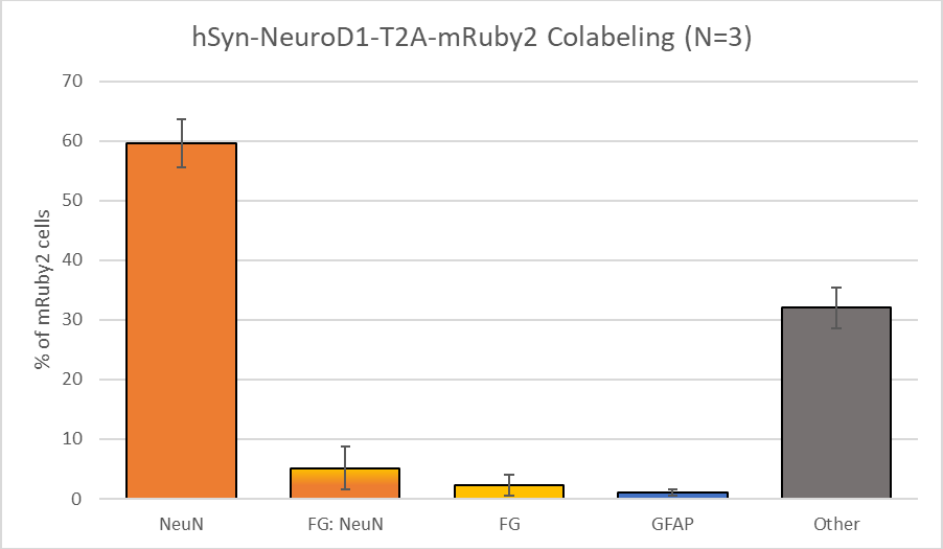

Figure 3.5: Incidence of hSyn-NeuroD1-T2A-mRuby2 Co-Labeling. Determined By Considering the mRuby2 Cells Allocation Across Experimental Groups. ~60% of mRuby2 cells are co-labeled with NeuN and 5% of those are also co-labeled with NeuN, while only ~1% appear co-labeled with GFAP.

3.3.1.3 TBI Lesion Size:

After validation of the virus's ability to transduce endogenous cells, the tests including TBI models were performed. To examine anatomical recovery, the TBI lesions were quantified using a rapid ex vivo ultrasound method established in our lab (Clark, Isaac H., et al. 2024). This allowed the quantification of the total lesion volume (Figure 3.6A). With respect to total lesion volumes, a non-statistically significant increase is observed between 1 and 3 weeks for all groups. Neuronal tissue degeneration is expected to continue for years after the initial injury, and has been observed in prior literature (Johnson, Victoria E., et al. 2013). No statistically significant differences were observed between treated and control groups.

3.3.1.4 Ventricular Volume:

Ventricle volume was quantified after tissue processing (sectioning, staining, and imaging) using QuPath to annotate the ventricular areas within coronal sections (Figure 3.6B). Significant differences were observed between 1 and 3 weeks for contralateral control, ipsilateral control, and ipsilateral treatments. This is in agreement with established literature which indicate that neuronal tissue degeneration further progresses following the onset of the initial injury. No statistically significant differences were observed comparing treated vs control groups nor contralateral vs ipsilateral ventricles.

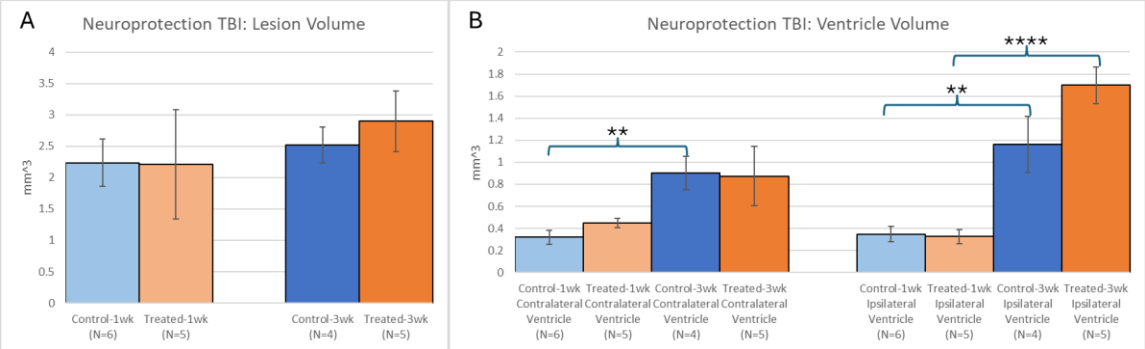

Figure 3.6: Lesion volumes and ventricle volumes. A: Lesion Volumes, Calculated via ex vivo ultrasound. No statistically significant differences observed. B: Ventricle Volumes. Left side = contralateral ventricle, right side = ipsilateral ventricle. P-values for 1 week vs 3 weeks for contralateral control, ipsilateral control, and ipsilateral treatments were respectively 0.0037, 0.0075, and 0.000028.

3.3.1.5 Behavior:

Neurological deficits were quantified through performance evaluation of rotarod and beam walk tasks (Figure 3.7). Data was normalized to the baseline behavior results acquired prior to injury. A statistically significant decrease was observed between baseline and 1 day post injury (DPI) in both groups for both rotarod and beam walk tasks indicating the injury had a negative effect on their motor skills. Recovery over time is present in both groups for both neurological tasks. No statistically significant differences were observed in the rotarod behavioral results. In the beam walk tests, the treated animals crossed faster

at all time points post injury suggesting enhanced recovery. This faster beam walk crossing is shown to be statistically significant at all DPI.

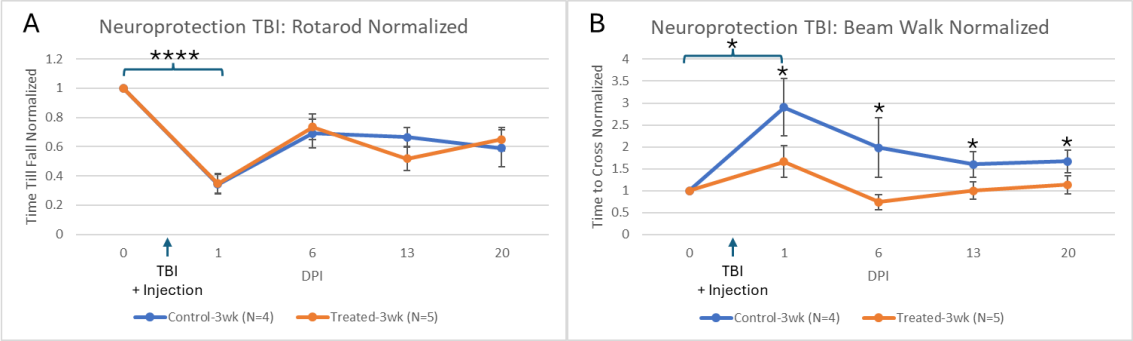

Figure 3.7: Neurological Tests. DPI=Days post injury. A: Rotarod test normalized. P-values comparing baseline vs 1 DPI for control and treatment were respectively 0.000035 and 0.0000053. No Statistically significant differences observed comparing control vs treated. B: Beam Walk Normalized. P-values comparing baseline vs 1 DPI for control and treatment were respectively 0.0076 and 0.043. P-values for control vs treated DPI 1, 6, 13, and 20 were respectively 0.047, 0.046, 0.028, and 0.037.

3.3.2 Astrocyte to Neuron Reprogramming with High Dose in TBI Models:

3.3.2.1 Experimental Design:

Preliminary experiments within our laboratory have yielded promising results suggesting that a reprogramming-based treatment may be beneficial in treating TBI models. Specifically, we found a statistically significant decrease in ventricle enlargement in treated animals. However, the preliminary experiments utilized bilateral TBI impacts, with one side designated as the control and the other as the treatment. These hits were staggered, where one hit was further anterior than the other. This was done to decrease the number of animals required and ensure each impact was sufficiently far away from the other as not to affect it. To mitigate any potential influence of experimental design on the observed differences, we replicated the experiment using single hits rather than bilateral hits. Control TBI mouse models were given a combined 3uL injection with two viral vectors: AAV9-GFAP(short)-Cre: 2.4E13 GC/mL and AAV9-CAG-DIO-mRuby2: 2.5E13 GC/mL, which should allow for transduction and marking of endogenous astrocytes without

inducing reprogramming. The treatment TBI mouse models were given a combined 3uL injection with AAV9-GFAP(short)-Cre: 2.4E13 GC/mL and AAV9-CAG-DIO-NeuroD1-T2A-mRuby2: 1.0E13 GC/mL, which should induce cell reprogramming in endogenous astrocytes. TBI was induced on day zero, virus injections were performed on DPI 7, and animals were euthanized on DPI 14 (Figure 3.8).

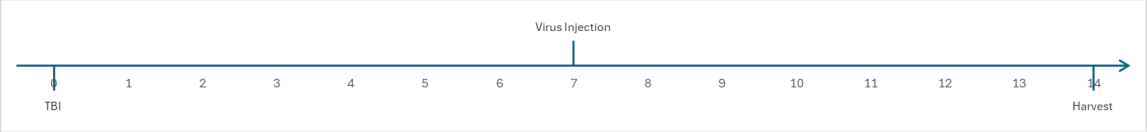

Figure 3.8: Timeline for Astrocyte to Neuron Reprogramming with High Dose in TBI Model Experiment.

3.3.2.2: Expression of NeuroD1:

To show successful expression of NeuroD1 in cells transduced with the treatment virus, tissue was stained for NeuroD1 and analyzed for co-labeling. Qualitative analysis showed that many cells expressing mRuby2, also expressed NeuroD1 (Figure 3.9).

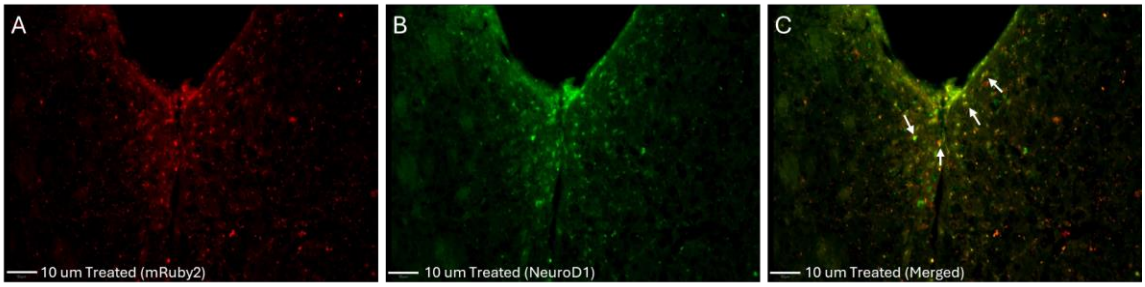

Figure 3.9: Co-labeling in AAV9-CAG-DIO-NeuroD1-T2A-mRuby2 treated animal. A: mRuby2 B: NeuroD1. C: Merged. White arrows showing examples of co-labeling. Scale bar = 10um.

3.3.2.3 TBI Lesion Size:

TBI lesions were quantified using the previously mentioned rapid ex vivo ultrasound method (Clark, Isaac H., et al. 2024). Total lesion volumes revealed no statistically significant differences between treated and control groups nor males and females (Figure 3.10A-B).

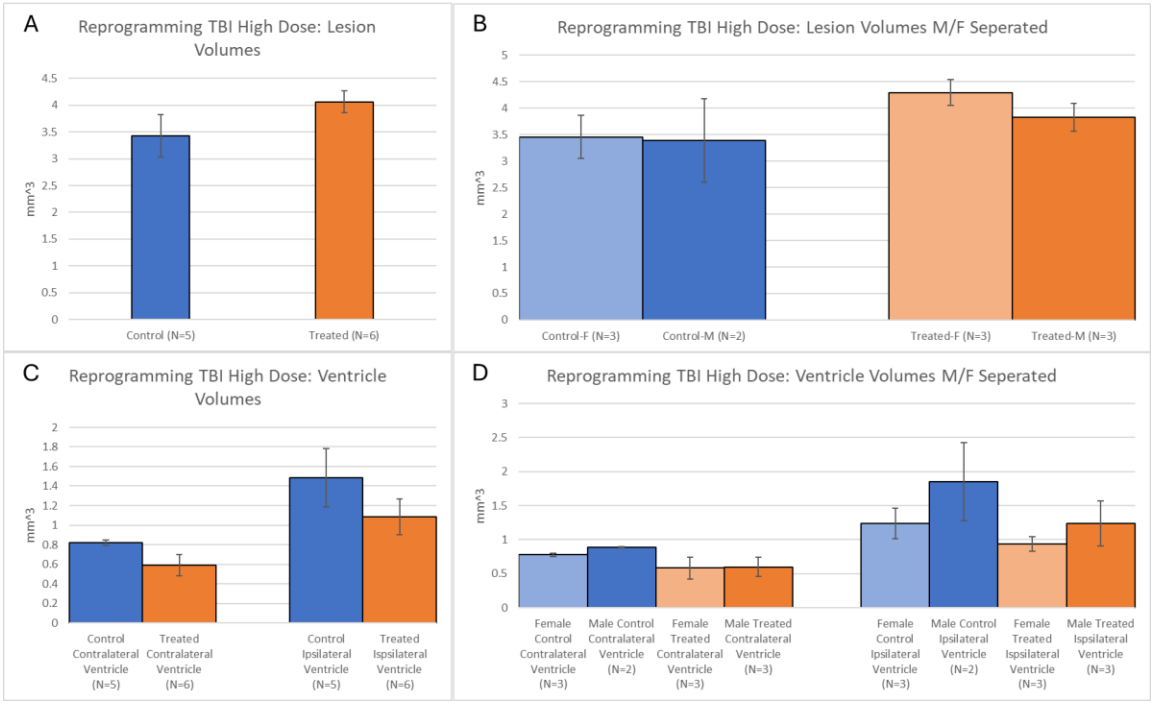

Figure 3.10: Anatomical analysis of control and treated groups. A: TBI Lesion volumes. No statistically significant differences between treated and control. B: TBI Lesion volumes with male and female data separated. No statistically significant differences between males and females. C: Ventricle volumes. No statistically significant differences between treated and control. D: Ventricle volumes with male and female data separated. No statistically significant differences between males and females

3.3.2.4 Ventricle Volumes:

Our preliminary results had indicated significant differences between ventricle size in treated and control mice. If the difference were attributable to the treatment, we would anticipate observing similar results in this experiment. However, no statistically significant differences were present between treated and control nor males and females, suggesting that our preliminary findings likely resulted from the experimental design rather than neurological repair (Figure 3.10C-D).

3.3.3 Alternate Dose Transduction:

3.3.3.1 Experimental Design:

All of the prior experiments up to this point had been explored at high doses (10^13 GC/mL). However, this is not the most appropriate dose, as recent research has shown that the apparent transduction of cells can be drastically altered by the dose of the virus (Chen, Gong, et al. 2020). High doses of AAV can be toxic to the cells transduced, leading to their death and apparent leakage of the expressed proteins. Specifically, it has been found that viral systems with lower doses targeting astrocytes have better transduction specificity rates than higher doses. To validate this, we sought to explore how different doses of our virus would affect which cells expressed our tracking biomarker mRuby2. We injected our control viral system AAV9-GFAP(short)-Cre + AAV9-CAG-DIO-mRuby2, varied the dose from 10^11, 10^12, and 10^13 GC/mL, and harvested all groups 5 days later (Figure 3.11). With this system, expression should be limited to astrocyte cells that naturally have the GFAP promoter highly active.

Figure 3.11: Timeline for Alternate Dose Transduction Experiment.

3.3.3.2 Co-labeling:

To analyze which cells expressed mRuby2, tissue was processed and stained for GFAP and NeuN. In agreement with the existing literature, the results showed an ideal trend with lower doses having greater co-labeling of their target cell type astrocytes. As the dose was increased, the number of GFAP positive co-labeled cells decreased and NeuN positive colabled cells increased (Figure 3.12). Percent of mRuby2 positive cells co-labled with GFAP was statistically significantly greater than percent of those co-labeled with NeuN

when a dose of 10^11 was used, while the inverse was observed with a dose of 10^13. Additionally, a statistically significant increase in percent of NeuN transduced cells was observed when comparing doses 10^11 vs 10^13, while the inverse was observed with GFAP. All of these observations support the notion that higher doses of virus injected will reduce the specificity of transduction intended to target astrocytes. As such, to optimize cellular reprogramming, these virus injections should not exceed doses of 10^11.

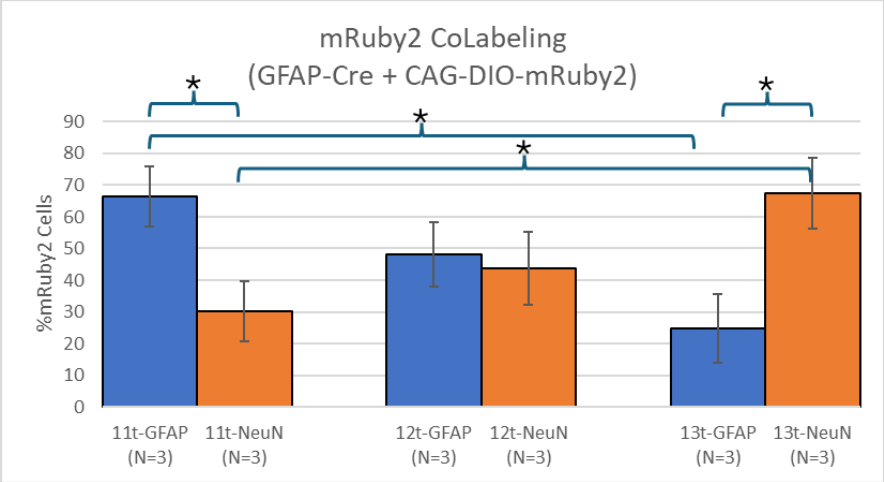

Figure 3.12: mRuby2 Co-labeling with control virus at alternate doses. GFAP vs NeuN 10^11 P-value=0.027, GFAP vs NeuN 10^13 P-value=0.026, 10^11 vs 10^13 GFAP P-value=0.022, 10^11 vs 10^13 NeuN P-value=0.032.

3.3.4 Astrocyte to Neuron Reprogramming with Low dose in TBI Models:

3.3.4.1 Experimental Design:

To capitalize on the findings in the previous experiment, we decided to explore the effects of a low dose NeuroD1 reprogramming treatment in TBI mice. Control TBI mouse models were given two viral vectors: AAV9-GFAP(short)-Cre: 2.4E11 GC/mL and AAV9-CAG-DIO-mRuby2: 2.5E11 GC/mL, while treatment TBI mouse models were given AAV9-GFAP(short)-Cre: 2.4E11 GC/mL and AAV9-CAG-DIO-NeuroD1-T2A-mRuby2: 1.0E11 GC/mL. TBI was induced on day zero, virus injections were performed on day 7, and animals were euthanized on day 28 (Figure 3.13).

Figure 3.13: Timeline for Astrocyte to Neuron Reprogramming with Low Dose in TBI Models Experiment.

3.3.4.2 Qualitative Co-labeling:

To determine if the virus was transducing cells as expected and promoting reprogramming, we processed one treated and one control mouse tissue sample. We found that in the control, evident mRuby2 cells did not have NeuN co-labeling (Figure 3.14 A-C). This was the desired result as it implies that the virus was not transducing endogenous neurons. We also found that in the treated samples, evident mRuby2 cells had faint NeuN co-labeling (Figure 3.14 D-F). We would expect cells transduced with the treatment viral system to express NeuN if they had successfully been reprogrammed into neurons. Additionally, as the signal was much fainter than the neighboring endogenous neurons, this suggests that the reprogrammed neurons were still in the process of maturing.

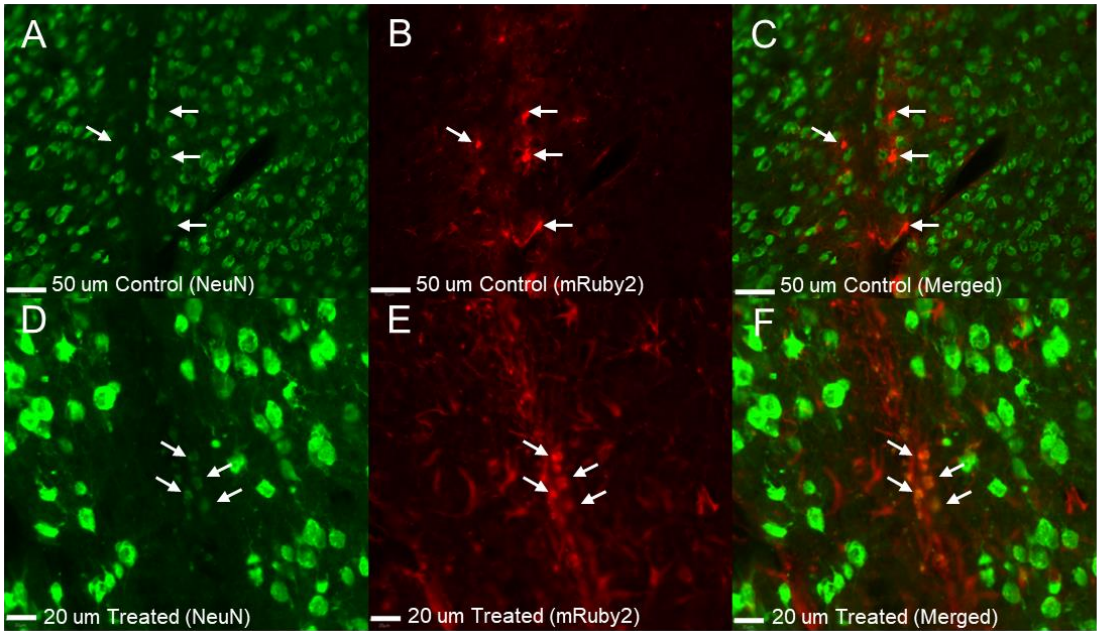

Figure 3.14: Qualitative Depiction of NeuN and mRuby2 co-labeling. White arrows labeling mRuby2 cells. A: Control tissue with NeuN displayed. B: Control tissue with mRuby2 displayed. C: Control tissue with NeuN and mRuby2 displayed. White arrows show mRuby2 cells are NOT co-labeled with NeuN. D: Treated tissue with NeuN displayed. E: Treated tissue with mRuby2 displayed. F: Treated tissue with NeuN and mRuby2 displayed. White arrows show mRuby2 cells are co-labled with NeuN.

We stained the tissue for NeuroD1 to further demonstrate that the virus was functioning as expected. We found that evident mRuby2 cells in control samples, did not have any NeuroD1 co-labeling present (Figure 3.15). This was expected and shows that cells transduced with the control virus did not produce any NeuroD1. We found that, in treated samples, many mRuby2 positive cells also had clear NeuroD1 co-labeling. This showed that the treatment virus was allowing expression of NeuroD1 as expected which would explain how reprogramming was able to occur.

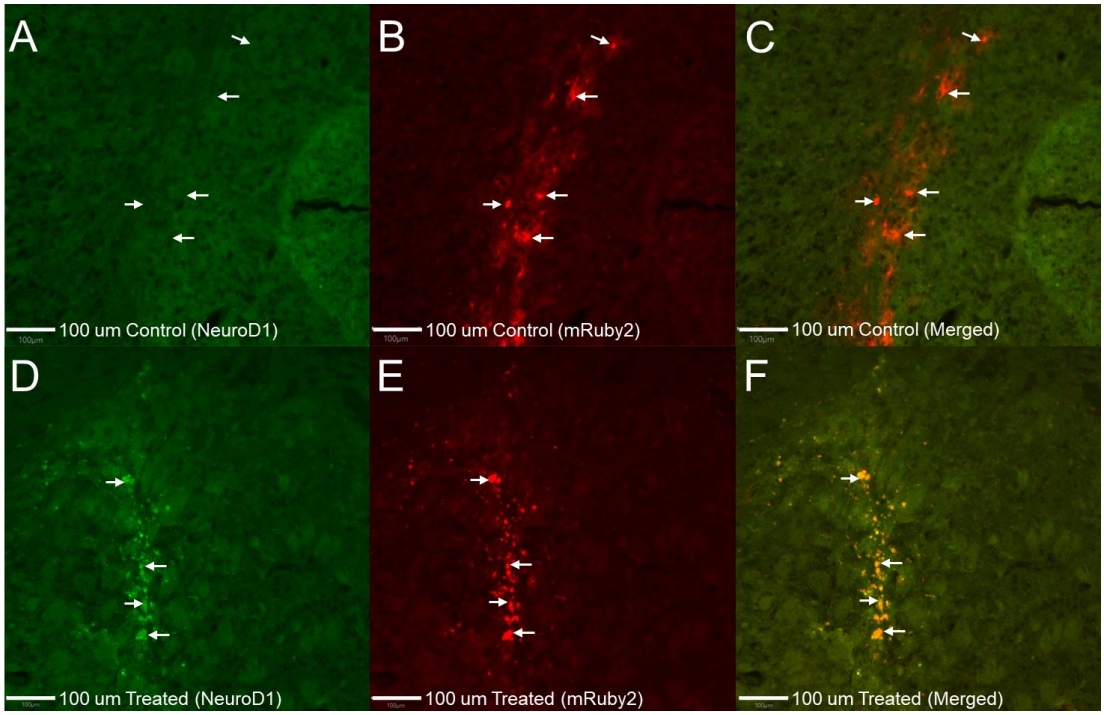

Figure 3.15: Qualitative Depiction of NeuroD1 and mRuby2 co-labeling. White arrows labeling mRuby2 cells. A: Control tissue with NeuroD1 displayed. B: Control tissue with mRuby2 displayed. C: Control tissue with NeuroD1 and mRuby2 displayed. White arrows show mRuby2 cells are NOT co-labeled with NeuroD1. D: Treated tissue with NeuroD1 displayed. E: Treated tissue with mRuby2 displayed. F: Treated tissue with NeuroD1 and mRuby2 displayed. White arrows show mRuby2 cells are co-labled with NeuroD1.

3.3.4.3 Behavior:

Neurological data was collected throughout the experiment in the form of rotarod and beam walk tasks. In both tasks, the treated group tended to recover and perform better than the control. When comparing treated to control in the rotarod, the treated group trended better and stayed on top of the rotarod for a longer period of time (Figure 3.16). This better performance however was not statistically significant. When comparing males to females in rotarod, no statistically significant differences were observed in control or treated groups.

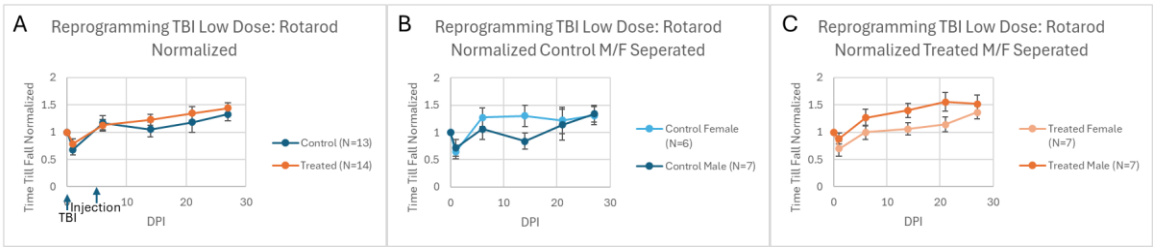

Figure 3.16: Rotarod Results. A: Normalized Rotarod Data. No statistically significant differences. B: Control only normalized rotarod data with male/female separated. No Statistically significant differences. C: Control only normalized rotarod data with male/female separated. No Statistically significant differences.

When comparing treated to control in normalized time to cross beam walk, treated animals had a statistically significant improvement over control at 21 and 27 DPI (Figure 3.17). Comparing males to females in beam walk, no statistically significant differences were observed. Comparing treated to control in beam walk foot faults, treated animals had a non-statistically significant increase in performance at 27 DPI. Comparing males to females in foot faults revealed statistically significant improvements in performance of females over males at 14 DPI for both treated and control groups and 21 DPI for control only groups.

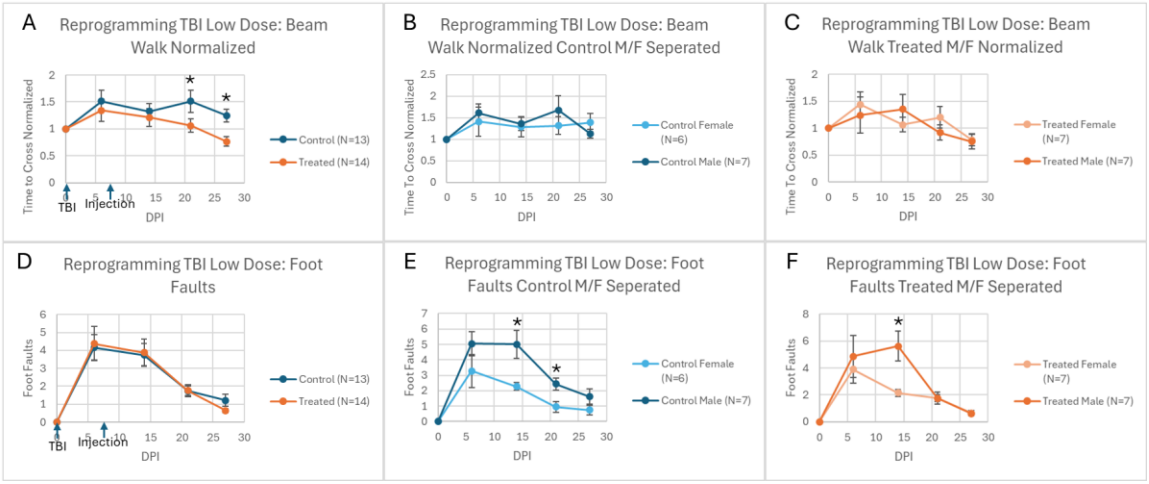

Figure 3.17: Beam Walk Results. A: Normalized beam walk. 21 DPI P-value=0.039, 27 DPI P-value=0.0017. B: Control only normalized beam walk. No Statistically significant differences. C: Treated only normalized beam walk. No Statistically significant differences. D: Foot fault. No Statistically significant differences. E: Control only foot fault. 14 DPI P-value=0.015, 21 DPI P-value=0.015. F: Treated only normalized beam walk. 14 DPI P-value=0.010.

3.4 Discussion:

3.4.1 Neuroprotection in TBI Mouse Models:

Through our experiments using FluoroGold and AAV9-hSyn-NeuroD1-T2A-mRuby in sham mice, we established that our virus had the potential to transduce endogenous neurons. The presence of numerous cells co-labeled with mRuby2 and NeuN but not FluoroGold constitute inconclusive results. While it is possible that these cells could be other cell types that were reprogrammed by the presence of NeuroD1, it is likely that these cells were in fact endogenous neurons that the FluoroGold was unable to reach and label. To further validate the specificity of this virus, future research should be conducted with an alternate virus that does not express NeuroD1, as well as improved FluoroGold labeling.

In agreement with prior literature, we observed increases in TBI lesion volume from 1-3 weeks. With a larger sample size and additional measures to ensure consistent TBI surgeries, this would likely be found to be significant. No significant differences were observed between TBI sizes of mice treated with AAV9-hSyn-NeuroD1-T2A-mRuby and control groups. This suggests that this neuroprotection targeted treatment may not play a role in preserving or restoring overall gross brain structure following TBI.

Ventricle volumes in TBI animals with and without the neuroprotection treatment showed increases from 1-3 weeks. These findings are corroborated by established literature, which have consistently shown that after the initial damage, neural tissue degeneration continues to advance. No differences between treated and control animals were observed however, further supporting that under these conditions this variation of neuroprotection treatment does not provide structural regeneration post TBI.

Interestingly, despite there being no significant differences on a structural level, our behavioral data revealed neurological benefits for this neuroprotection treatment. Beam walk behavioral tests are an effective means to test balance and coordination which would be directly affected by damage to the motor cortex. Rotarod, while also a means of testing coordination and balance, may be more descriptive of a subject's strength and endurance. The neuroprotection treated animals performed better in beam walk than control, but the same in rotarod as control. This indicates that the treated animals had a faster neurological recovery that beam walk was able to identify but rotarod was not.

Given that the treated group showed improved recovery in one of the two neurological assessments and that we did not observe any beneficial neuroprotection in ventricle size, it is reasonable to conclude this neuroprotection treatment is ineffective in gross structural recovery but does slightly improve neurological recovery. Future research for this treatment approach should focus on optimizing the virus dose to minimize any potential toxicity, improving consistency of TBI injuries, increasing the sample size, analyzing other neurological tests, and further studying the morphology of transduced cells.

3.4.2 Astrocyte to Neuron Reprogramming with High Dose in TBI Models:

When exploring the effect of high dose delivery of AAV9-GFAP(short)-Cre and AAV9-CAG-DIO-NeuroD1-T2A-mRuby2 for the promotion of astrocyte to neuron reprogramming in TBI models, our analysis using rapid ex vivo ultrasound showed no significant difference in total lesion volumes between treated and control groups. Similar to the neuroprotection results, this suggests that this high dose reprogramming-based treatment also did not affect the structural recovery of the brain following TBI.

The preliminary results we found in our lab using the high dose reprogramming treatment in TBI models showed significant differences in ventricle volumes between treated and control mice, which we initially attributed to the treatment's efficacy. However, in the replicated experiment, no statistically significant differences in ventricle size were observed. This inconsistency implies that our earlier findings were likely a consequence of the bilateral impact model's design rather than a true effect of the high dose reprogramming treatment. Similar to the TBI lesion results, this further supports that the treatment is ineffective in assisting in gross structural recovery of the brain following TBI.

3.4.3 Alternate Dose Transduction:

In conformity with established literature, when exploring the effects of varying the dose of our virus (AAV9-GFAP(short)-Cre and AAV9-CAG-DIO-mRuby2) from 10^11 to 10^13 GC/mL, our findings revealed an ideal tendency in which lower doses expressed greater co-labeling of their target astrocyte types. We observed statistically significant findings that increases in dose had a positive correlation with NeuN-positive co-labeled cells and a negative correlation with the number of GFAP-positive co-labeled cells. This indicates that to optimize cellular reprogramming of astrocytes into neurons, lower doses such as 10^11 GC/mL should be used. This should be further explored to determine the mechanisms dictating apparent cell transduction and to what degree higher doses are resulting in toxicity that may be killing cells as suggested by prior literature (Xu, Liang, et al. 2022; Chen, Gong, et al. 2020).

3.4.4 Astrocyte to Neuron Reprogramming with Low Dose in TBI Models:

Given the results of our prior studies, it becomes clear that parameters such as dose and bilateral vs single hit TBI models are crucial to consider when studying these NeuroD1 based treatments. In our last study we used that prior information to design a more optimal

experiment in which a low dose delivery of AAV9-GFAP(short)-Cre and AAV9-CAG-DIO-NeuroD1-T2A-mRuby2 was given for the promotion of astrocyte to neuron reprogramming in TBI models. Qualitative analysis of the transduced cells revealed the transduced cells in the treated animals did express both NeuroD1 and NeuN, while transduced cells in control animals did not express NeuroD1 or NeuN, indicating cellular reprogramming occurred in treated animals but not in control animals as desired.

We found no statistically significant differences between treated and control in rotarod tasks but did find significant differences in beam walk tasks, similar to the neuroprotection experiments. This suggests that the motor and sensory skills used in rotarod were unaffected by this treatment post TBI and that alternate neurological tests may be better suited. The significant differences found in beam walk however, indicate that the presence of cellular reprogramming can facilitate neurological recovery. The mechanism behind this likely being that additional neurons increase the rate of natural brain plasticity, allowing new structural and functional connections to be formed for motor and sensory systems. If paired with electrical stimulation used in neuromodulation treatment approaches, this brain plasticity may be further facilitated by encouraging formation of synaptic connections.

3.5. Conclusion:

The results of this study show that AAV-mediated delivery of NeuroD1 intended for neuroprotection or reprogramming can provide neurological benefits when used to treat TBI. To ensure consistent research results, several factors including virus dose, the timing of administration, and the specific injury model used, must be considered and optimized.

While neither neuroprotection nor astrocyte to neuron reprogramming treatments demonstrated gross structural recovery of the brain, both methods resulted in neurological

improvements in beam walk task performance. This suggests that these treatments may enhance functional recovery by promoting neural plasticity rather than directly preserving or restoring brain architecture. Our research also validated and supported the prior literature in the field, showing that lower virus doses result in improved transduction specificity. Further investigation should be conducted to determine if increases in specificity result in improved rates of cellular reprogramming and what the underlying mechanisms are for improved neurological performances.

Future research should focus on optimizing experimental parameters, and incorporating additional behavioral and molecular analyses to better understand the precise neurological benefits and the mechanisms prompting them. Additionally, exploring combinatorial approaches, such as pairing delivery of NeuroD1 for cellular reprogramming with neuroprotection and/or neuromodulation approaches may provide even greater benefits. Our research provides a promising foundation for the continuation of NeuroD1 based treatment approaches in TBI models.

Chapter 4: Astrocyte to Neuron Reprogramming with NeuroD1 for Repair in Canine Stroke

4.1 Introduction:

This chapter was adapted from a finished manuscript, currently in the submission process to the scientific journal “Frontiers in Stroke”. Stroke afflicts more than 700,000 people each year in the US alone (Tsao, Connie W., et al. 2023). Of those who survive stroke, nearly two thirds of them develop a long term disability. Stroke occurs when the supply of blood to the brain tissue is disrupted due to a focal vascular cause, resulting in neuronal damage (Knight-Greenfield, Ashley, et al. 2019). Stroke can be divided into two major categories, ischemic, which occurs when a blockage within the blood vessels prevents blood flow to a portion of the brain, and hemorrhagic stroke, which occurs when a blood vessel ruptures and leaks blood into a portion of the brain. The ischemic form of stroke can be modeled in animals through clamping a major vessel, such as the middle cerebral artery, and preventing blood flow for a period of time. Due to their size, brain structure, and vascular system, canine models can provide an effective representation of the pathophysiological effects of transient occlusions and subsequent molecular events that can be translated to the human condition (Lv, Xianli, et al. 2020).

Neurons have very limited ability to recover post injury due to an inability to divide and regenerate. Processes such as neurogenesis can promote recovery, but little is understood about this process and it is typically limited to the hippocampus and rostral migratory stream (van Strien, Miriam E., et al. 2011; Cameron, Heather A., and Lucas R. Glover. 2015). Astrocyte to neuron reprogramming is a process that has the potential to treat neurological diseases and disorders by replacing damaged or diseased neurons with new neurons originating from astrocytes (Peng, Zhouzhou, et al. 2022). This

process is often performed through the use of an Adeno Associated Viral (AAV) vector and targets astrocytes by using promoters such as those for the expression of the glial fibrillary acidic protein (GFAP) gene. Targeting astrocytes near the stroke injury could replace the damaged or diseased neurons and facilitate neurological recovery.

Cellular reprogramming of astrocytes into neurons has been studied in stroke models such as rats with anatomical and neurological benefits being recorded (Chen, Yu-Chen, et al. 2020). This process has also, however, been riddled with controversy as to the origin of the resulting neurons. Lineage tracing, virus concentration (dose), virus serotype, and alternate promoters all have the potential to affect the apparent transduction and cellular changes. AAV transduction at higher doses has been shown to result in transaminase elevations and cell degeneration (Hinderer, Christian, et al. 2018). If astrocytes are targeted for transduction, this can result in the death of said astrocytes, leakage of the promoted biomarkers, and confounding results regarding the cells that express the promoted biomarkers (Xu, Liang, et al. 2022). To analyze cellular reprogramming in a more translatable stroke model of cerebral ischemia, we induced cellular reprogramming in canine stroke models. In this study, we found promising results of anatomical and behavioral recovery that should encourage further research in the field.

4.2 Methods:

4.2.1 Animals:

The three animals used in this study were male canine beagles with weight 8 to 11 kg. Two served as the treatment group and one served as the control animal.

4.2.2 Virus:

To induce reprogramming, we used a set of serotype 9 Adeno Associated Viral (AAV9) vectors (which have been shown effective in transducing neuronal tissues). The first vector, which was used in both treated and control animals, was AAV9-GFAP(short)-Cre which was given at a dose of 2.4E13 GC/mL. The vector was designed to induce expression of Cre recombinase specifically in astrocytes via a GFAP promoter. Cre recombinase alters DNA with specific sequences known as loxP sites and can invert sequences that are flanked by the sites, viable for protein synthesis. In our case, this was used in combination with a second control or treatment vector containing a transgene with loxP sites, which would allow for the transgene to be expressed.

The control secondary vector was AAV9-CAG-DIO-mRuby2, which was given at a concentration of 2.5E13 GC/mL. The CAG promoter was meant to induce expression of the desired genes in any cells that were also transduced by the first virus. This promoter is independent of cell type, thus allowing the following sequence to continue to be produced even after reprogramming may change the cell phenotype from an astrocyte to a neuron. The mRuby2 biomarker was meant to label all transduced cells. The secondary treatment vector was AAV9-CAG-DIO-NeuroD1-T2A-mRuby2, which was delivered at a concentration of 1.0E13 GC/mL. This viral system was meant to function in the same manner as the control with the addition of allowing expression of NeuroD1 in transduced cells. NeuroD1 is a transcription factor that has been shown in numerous studies to induce cellular reprogramming, and in this study, it was meant to convert astrocytes into neurons.

4.2.3 Canine Stroke:

The canine stroke model we used was established previously within our lab (Vasquez, Ciro A., et al. 2019). On the day of the procedure, each animal is sedated with Acepromazine, 0.05-0.2 mg/kg, IM. Two 18-guage IV's are placed in either fore or hind limbs depending on vein accessibility. Propofol, 4-6 mg/kg, is administered IV. Canines are then intubated and maintained under general anesthesia using isoflurane (1.5-2.5%) for the duration of the procedure. During this time vital signs including pulse, blood pressure, and temperature are monitored according to IACUC specifications and APIC standards. Additionally, prior to beginning the procedure, eye lubricating ointment is applied to both eyes, the eyes are closed, and the animals receive a 30 mg/kg dose of Cefazolin. After each animal was anesthetized, the right frontal region of the head was shaved, and prepped with alcohol then betadine. Sterile towels were then draped around the surgical site in the right frontal area.

A curvilinear incision, measuring between 1-2.5 inches in length, was made approximately 1 cm above the level of the right zygomatic arch. The skin was then reflected inferiorly and held in place by a suture. Hemostasis was obtained with bipolar and monopolar cautery. The zygomatic arch was identified and removed using a pneumatic drill. Bleeding from the bone was controlled with bone wax. The temporalis muscle was incised using a monopolar cautery in a linear fashion, perpendicular to the previous zygomatic arch, exposing the underlying cranium. After mobilizing the temporalis muscle off the cranium with a periosteal dissector, the muscle was held in place with fishhook retractors. Using a pneumatic drill, a 2 cm x 2 cm area of bone was removed at the inferior level of the temporal lobe. Care was taken to drill the cranium down to the level of the middle fossa floor so that retraction of the temporal lobe can be

minimized. The underlying dura was then coagulated with bipolar cautery and opened with either a scalpel or an insulin syringe.

A neurosurgical microscope, sterilely draped, was then brought into the surgical field for the remainder of the procedure. Using microscopic dissection techniques, the frontal lobe was gently retracted and held in place with a small brain retractor. The arachnoid over the frontal lobe was incised with an insulin syringe. The distal middle cerebral artery (MCA) was identified and traced back to the proximal or M1 segment where it divides from the internal carotid artery (ICA). Next the ophthalmic artery (OA) and anterior cerebral artery (ACA) were isolated. At this time aneurysm clips were temporarily applied to the ACA, OA and the MCA (distal to the lenticulostriate vessels). These clips remain in place for 1 hour. After placing the aneurysm clips the MCA pial collateral vessels are identified and coagulated. This step was essential to minimize collateral circulation to the intended area of infarction. Once 60 minutes passed, the 3 aneurysm clips were removed. After irrigating the surgical site, the temporalis muscle was closed with interrupted or running sutures followed by a primary skin closure using either interrupted or running sutures.

4.2.4 Virus Injection:

Animals were prepped and anesthetized in the same manner as the stroke procedure. Following exposure of the previous surgical area, the virus was prepped for injection. Each injection consisted of 0.5 µL of AAV9-GFAP(short)-Cre with either 0.5 uL of AAV9-CAG-DIO-mRuby2 or 0.5uL of AAV9-CAG-DIO-NeuroD1-T2A-mRuby2. Five injections were given surrounding the peripherals of the stroke areas at a depth of ~1cm. After the injection, the site was closed in the same manner as the stroke procedure.

4.2.5 Behavior:

To assess neurological deficits and functional recovery, a modified neurological severity score was acquired based on several neurological assessments as seen in table 4.1. All tasks were assessed by visual observation unless otherwise stated.

Test	**Scores**
Stance	(1=broad based stance, 0=normal stance)
Cerebellar Ataxia	(3 = severe gait dysmetria, 2 = moderate gait dysmetria, 1 = modest gait dysmetria, 0 = normal gait);
Unilateral Vestibular Ataxia: Leaning or Falling to one side	(3 = severe, 2 = moderate, 1 = modest, 0 = no leaning and falling)
Unilateral Vestibular Ataxia: Head Tilt	(3 = severe, 2 = moderate, 1 = modest, 0 = no head tilt)
Unilateral Vestibular Ataxia: Nystagmus	(3 = severe, 2 = moderate, 1 = modest, 0 = no nystagmus)
Bilateral Vestibular Ataxia	(3 = severe, 2 = moderate, 1 = modest, 0 = none)
Hemiparesis	(3 = severe, 2 = moderate, 1 = modest, 0 = none)
Paraparesis	(3 = severe, 2 = moderate, 1 = modest, 0 = none)
Proprioceptive Positioning: (assessed by inverting paw, placing dorsal surface in contact with ground and and timing till corrected) (left/right, fore/hind)	(2 = severe delay, 1 = moderate delay, 0 = normal)
Placing Response: (assessed by covering vision, moving limb to edge of surface, and timing till reflexively placed upright on surface) (left/right, fore)	(2 = severe delay, 1 = moderate delay, 0 = normal)
Placing Response Visual	(assessed by moving limb to edge of surface and timing till reflexively placed upright on surface) (left/right, fore) (2 = severe delay, 1 = moderate delay, 0 = normal)
Tremor	(3 = severe, 2 = moderate, 1 = modest, 0 = none)
Auditory Response	(Assessed by clapping on left or right side and recording response) (Ipsilateral/Contralateral) (1 = no response to noise, 0 = normal orientation to noise)
Best Ambulation Attempt	(8=no movement, 7=unable to right self but moves, 6=able to right self, 5=unable to stand, 4=stands w/ assistance, 3=stands w/o assistance, 2=circles but falls to side, 1=circles, 0=normal)

Vocalization	(2=none, 1=howls/grunts, 0=normal)
Consciousness	(3=does not awaken, 2=awakens w/ noxious stimulus, 1=awakens w/ minimal stimulation, 0=awake & interactive)

Table 4.1: Canine Behavioral Tests. All behavioral tests used to generate the Canine neurological severity score.

4.2.6 MRI Acquisition:

MRIs were obtained in the University of Minnesota MRI (located in the basement of the hospital which is connected to PWB RAR facility by tunnel). Animals were anesthetized with general anesthesia for MRI. The scan tools are approximately 1 hour and include T1, T2, T2* gradient echo, flair, TOF, and perfusion scans. Once stable, animals were transported from MRI to a holding cage and recovered by RAR care staff.

4.2.7 Anatomical Quantification:

To quantify stroke lesion volume, the T2 scans were loaded into 3D slicer and segmented. Segmentation was performed using “grow from seeds” with seeds being placed to identify stroke lesion areas and non-stroke areas. After seed growth, smoothing was applied, and the resulting volume was recorded. The same method was used on a separate copy of the scan to quantify ventricular volumes.

4.2.8 Tissue Processing:

All dogs were anesthetized using isoflurane and euthanized through perfusion with PBS and 4% PFA, then decapitated. After being removed, their brains were incubated in 4% PFA for 24 hours at 4°C. The next day, using a shaker, the brains were washed with PBS three times for five minutes each. The brains were immersed in 10% sucrose for 24 hours at 4°C to create a sucrose gradient. The brains were then immersed in 20%

sucrose for 24 hours at 4°C the next day. Finally, the brains were immersed in 30% sucrose for 24 hours at 4°C the following day.

4.2.9 Tissue Cryosectioning:

The dogs' brains were embedded in OCT the next day, and 20 um thick brain cryo-sections were made using a Leica CM1850 cryostat.

4.2.10 Tissue Staining:

Sections were blocked with 5% donkey serum, permeabilized with PBST (0.3% Triton X-100), and fixed with 4% PFA. After that, slices were incubated with primary antibodies against GFAP (1:500, abcam, ab278054), NeuN (1:500, abcam, ab104224), Iba1 (1:50, Wako Chemicals, 019-19751), and NeuroD1 (1:250, abcam, ab205300) overnight at 4 °C in 5% donkey serum blocking solution. Sections were washed with PBST (0.1% Triton X-100), let to sit at room temperature for an hour, and then centrifuged in 5% donkey serum blocking solution with secondary antibodies labeled with Alexa Fluor 488, 555, or 647 (1:1000, Abcam). Following rinsing, the slices were wet mounted and imaged using a Leica DMI6000 B microscope.

4.2.11 Co-Labeling:

To detect mRuby2 co-labeling, analysis of microscopy acquired images was performed using QuPath. Cell detection was performed on channel wavelength 555, to identify all mRuby2 positive cells. After identification, single measurement classifiers were used to classify if a cell was co-labled for NeuN or GFAP. Classifiers were determined per image and changed depending on staining quality. After classification, the resulting values were recorded, and statistics were performed.

4.3 Results:

4.3.1 Experimental Design:

Established reports in the scientific literature have shown beneficial effects of the use of cellular reprogramming in stroke models (Chen, Yu-Chen, et al. 2020). We decided to explore larger, more comprehensive animal stroke models with vasculature more analogous to humans (i.e. canine). For this experiment, 3 male beagle canine stroke models were used, 2 of which were given the treatment viruses “AAV9-GFAP(short)-Cre: 2.4E13 GC/mL and AAV9-CAG-DIO-NeuroD1-T2A-mRuby2: 1.0E13 GC/mL” meant to reprogram astrocytes into neurons and 1 of which was given the control viruses “AAV9-GFAP(short)-Cre: 2.4E13 GC/mL and AAV9-CAG-DIO-mRuby2: 2.5E13 GC/mL” meant to identify transduced cells. Stroke was induced at day zero, an MRI was acquired at day 1, the virus was injected at day 7, a second MRI was taken at day 28, and the animals were euthanized at day 29 (Figure 4.1). Periodically through that time behavioral data was also acquired.

Figure 4.1. Timeline for Astrocyte to Neuron Reprogramming Canine Stroke Models Experiment.

4.3.2 Stroke Lesion Volume:

Stroke lesion volume was quantified using the T2 Flair MRI scan from day 1. The quantification was performed using segmentations in 3D Slicer. This quantification revealed that two canines had large strokes while one had a significantly smaller stroke (Figure 4.2). Due to this significant difference, animal DSM21 (one of the large stroke animals) was chosen as the control animal, while the other two were administered the

treatment virus. Additionally, to account for the varying stroke lesion volumes, the data were quantified individually for each animal rather than averaged.

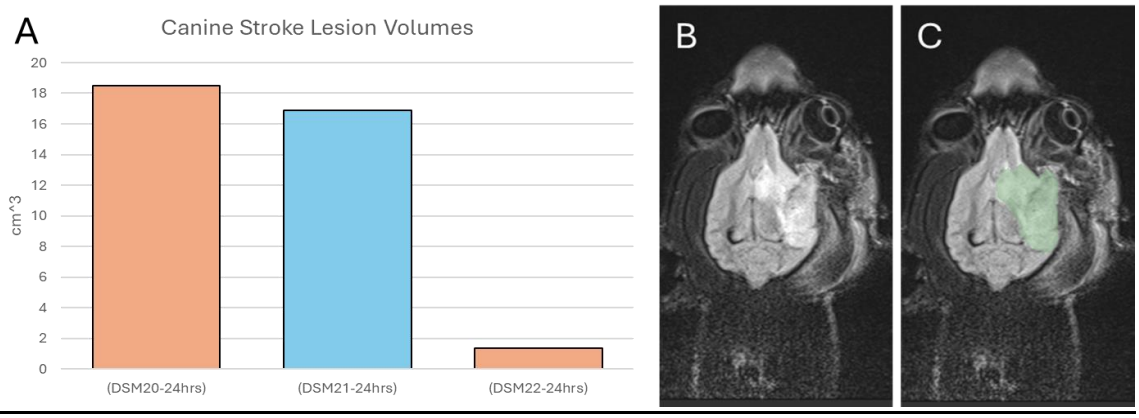

Figure 4.2: Canine Stroke Lesion Volumes. A: Volume in cm^3 of each animal's stroke. B: T2 MRI scan of canine brain 24 hours post stroke. C: Segmented stroke volume of T2 scan.

4.3.3 Hemisphere Volumes:

The left and right hemispheres of each canine were quantified using AX Recon MRI scans from day 1 and 28. Hemisphere quantification allows for the analysis of inflammation or tissue loss between the hemisphere on the ipsilateral side of the stroke and the contralateral side. The ipsilateral hemisphere from each animal and time point was normalized to the corresponding contralateral hemisphere to account for any quantification error (Figure 4.3A). This quantification revealed that the ipsilateral hemisphere of each animal was larger than the contralateral hemisphere at 1 day post-stroke. This correlates well with the existing literature (Anrather, Josef, and Costantino Iadecola. 2016), as strokes induce inflammation and swelling in the affected brain region. Prior to treatment, similar levels of swelling were observed in the large stroke animals while much less swelling was seen in the small stroke animal. Specifically, large stroke animals DSM20 and DSM21 exhibited ipsilateral hemispheres that swelled to 123% and 125% the size of their corresponding contralateral hemisphere, respectively, while the small stroke animal DSM22 showed swelling of only 106%. On day 28, after sufficient time

for brain recovery and treatment administration, the ipsilateral hemisphere in all animals was smaller than the corresponding contralateral hemisphere indicating atrophy or tissue loss within the ipsilateral hemisphere. Interestingly there was little difference between the large stroke-treated animal DSM20 and the large stroke-control animal DSM21 with their ipsilateral hemispheres being 81% and 83% the size of their corresponding contralateral hemispheres, respectively. Similarly, the small stroke-treated animal exhibited less difference in hemisphere sizes with its ipsilateral hemisphere being 93% the size of its corresponding contralateral hemisphere.

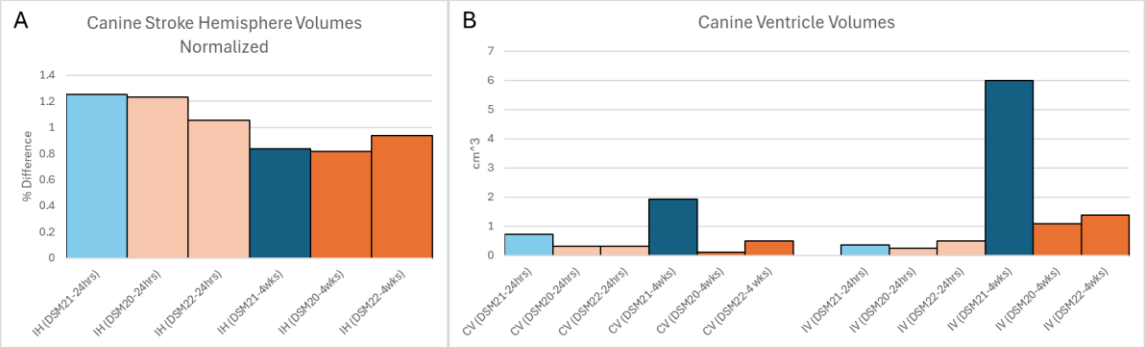

Figure 4.3: Anatomical Changes over time. A: Canine Stroke Hemisphere Volumes Normalized. The ipsilateral hemisphere was normalized against the corresponding contralateral hemisphere. IH=Ipsilateral Hemisphere. B: Canine Ventricles Volume. IV=Ipsilateral Ventricle. CV=Contralateral Ventricle.

4.3.4 Ventricle Sizes:

The left and right ventricles of each canine were quantified using the AX Recon MRI scans from days 1 and 28 (Figure 4.3B). Ventricular enlargement is often associated with tissue atrophy, blockage, and/or changes in tissue properties such as decreased diffusivity (Sayed, Mohammed A., et al. 2020, Zahr, Natalie M., et al. 2013). On day 1 post-stroke, ventricular sizes were similar between the contralateral and ipsilateral sides across all animals. However, by day 28 the ventricle on the ipsilateral side of all animals was noticeably larger than its corresponding contralateral side, indicating some degree of tissue atrophy in all animals. Interestingly, the large stroke control animal DSM21 exhibited

a substantial increase in both contralateral and ipsilateral ventricles of 2.7x and 16.2x respectively, from day 1 to day 28. However, as the hemisphere changes do not reflect this difference in the form of greater tissue loss, it can be assumed that this increase in ventricle size in the control animal is not correlated with greater tissue atrophy. This notable increase in ventricular size is more likely due to a potential ventricular blockage or detrimental changes to its tissue properties. These observations suggest that either this particular stroke resulted in an unintended blockage, or the treatment had a beneficial effect in preventing detrimental changes to tissue properties.

4.3.5 Transduced Cell Phenotypes:

To determine which cells were transduced and the rate of cellular reprogramming, tissue was cryosectioned and stained for GFAP and NeuN markers using IHC to identify astrocytes and neurons respectively (Figure 4.4D). To prevent image bleed through, slices were stained with either GFAP or NeuN, but not both. If reprogramming occurred, we would expect to see a majority of the mRuby2 co-labeled cells in the treated animals to be NeuN positive. Within treated animal DSM22, approximately ~80% of mRuby2 cells were co-labeled with NeuN. Within the treated animal DSM20, approximately ~85% of mRuby2 cells were co-labeled with NeuN. Interestingly, in control animal DSM21, despite the presence of the GFAP promoter and lack of the NeuroD1 sequence in the control virus, this animal also exhibited a high level of mRuby2 co-labeling in NeuN positive cells, at around 74%. This indicates that transduction may have targeted endogenous neurons rather than astrocytes or leakage may have occurred from the transduced astrocytes. As these experiments were conducted with high dose virus injections, these results align with previous research suggesting that injections of astrocyte-targeting viruses with higher doses often lead to more co-labeling with NeuN positive cells (Xu, Liang, et al. 2022).

There is however a noticeable increase in NeuN positive mRuby2 cells in the two treated animals with 80 and 85% vs the control animal with 74%. Since NeuN is a neuronal marker, this increase suggests that some astrocytes were successfully reprogrammed into neurons. To validate NeuroD1 was in fact being produced, staining was performed to assess NeuroD1 and mRuby2 co-labeling (Figure 4.4A-C). We confirmed that in the treated animals, NeuroD1 was present in >70% of mRuby2 positive cells. NeuroD1 was not visible in the control animal.

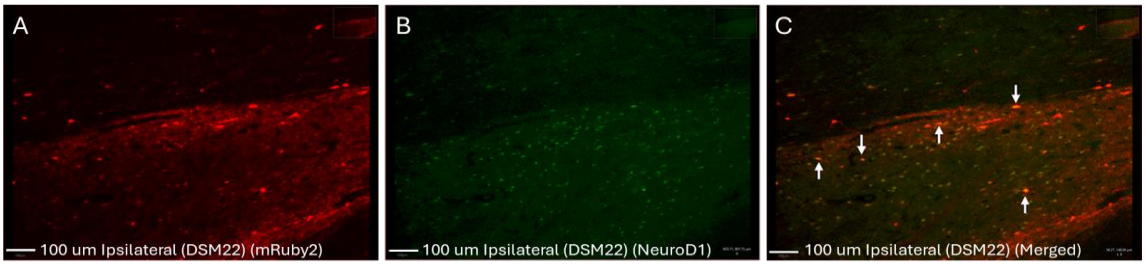

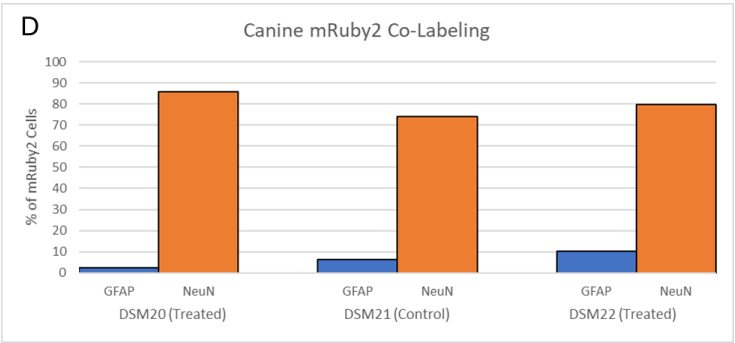

Figure 4.4. NeuroD1, NeuN, and GFAP co-labeling with mRuby2. A-C: Canine NeuroD1 & mRuby2 Co-labeling in treated animal DSM22. A: mRuby2 alone. B: NeuroD1 alone. C: Merged. QuPath quantification revealed 70.95% of mRuby2 positive cells were positive for NeuroD1. D: Canine mRuby2 Co-Labeling. Percentage of mRuby2 cells co-labled with either GFAP or NeuN.

4.3.6 Astrocyte and Microglial Activation:

To assess the immune response in all animals, sections near the stroke site stained for GFAP were quantified for astrocyte activation and microglial activation (Figure 4.5A-B, D-E). Images were acquired near the stroke lesion and the corresponding contralateral side. Five regions were quantified on both the ipsilateral and contralateral sides for each animal. Activated astrocytes tend to have enlarged soma's and processes (Pekny, Milos, et al. 2014). By comparing the astrocytes in hemispheres contralateral and ipsilateral to the

stroke in these animals, we were able to determine the average inactive astrocyte soma size and its standard deviation. With that, we estimated a soma size threshold value that was two full standard deviations above the inactive average to differentiate between inactive and active cells. We then estimated the percentage of active vs inactive astrocytes and found that the control animal had the highest rate of astrocyte activation in the ipsilateral hemisphere (19%) (Figure 4.5C). Similarly, activated microglia tend to be enlarged, and we used the detection data to estimate a threshold size value to differentiate them. The microglial activation followed the same trend as the astrocyte activation with greatest activation in the ipsilateral side of the control animal.

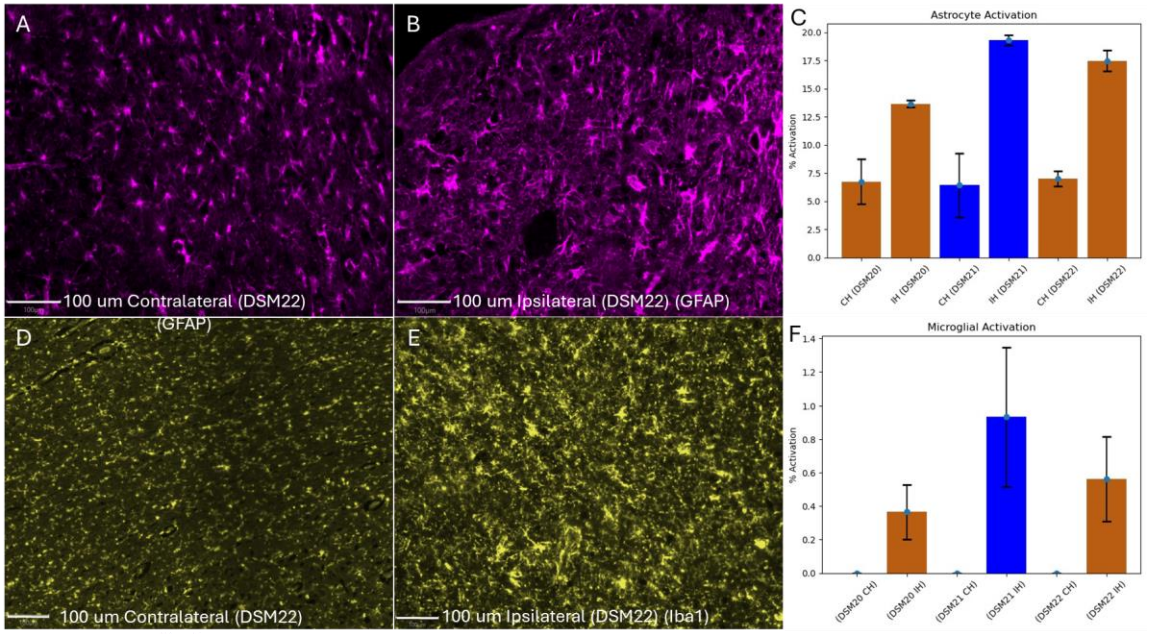

Figure 4.5: Astrocyte & Microglial Activation. A: Contralateral Hemisphere of treated canine DSM22 with GFAP Staining (minimal enlarged astrocytes present). B: Ipsilateral Hemisphere with GFAP Staining (several enlarged astrocytes present). C: Number of activated astrocytes divided by total astrocytes. D: Contralateral Hemisphere of treated canine DSM22 with Iba1 Staining (No activated microglia present). E: Ipsilateral Hemisphere with Iba1 Staining (several activated microglia present). F: Number of activated microglia divided by total microglia. CH=Contralateral Hemisphere. IH=Ipsilateral Hemisphere.

4.3.7 Behavioral Analysis:

To assess functional recovery, the behavior of each animal was evaluated using a modified neurological severity score (Figure 4.6A). All animals showed neurological impairments after stroke and had some level of recovery in the following days. As expected, the smaller stroke animal DSM22, had fewer impairments compared to the animals with larger strokes. Promisingly, the large stroke-treated animal DSM20 showed faster and greater overall recovery than the large stroke control animal DSM21. Between days 5 and 23, it can be noticed that the treated animals had a nearly identical linear recovery, with trendline slopes of -0.401 and -0.393, while the control animal remained almost stagnant in recovery with a trendline slope of -0.016. This coincides with the timing of virus injection which occurred on day 7 and suggests the treatment's presence had some beneficial neurological effects and provide a basis for future research. When comparing the average behavior score to the microglia and astrocyte activation, we get two trend lines supporting that greater inflammatory responses correlate to worse neurological severity scores.

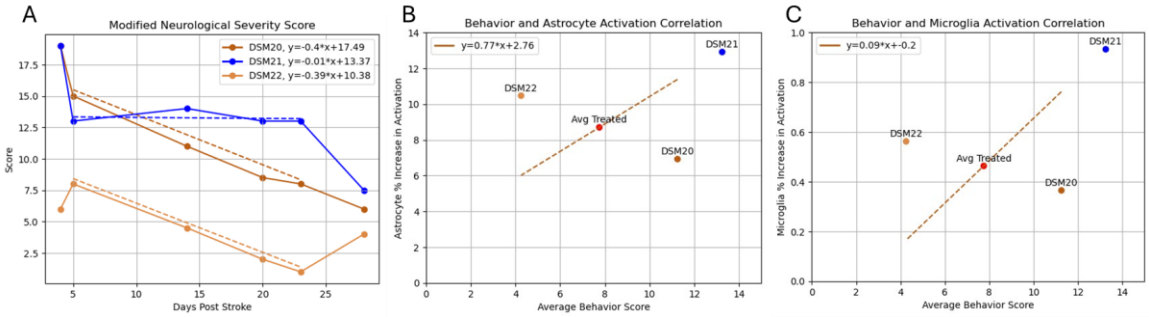

Figure 4.6: A Modified neurological severity score vs days post stroke. Trendlines generated from day 5-23 range. B. Average behavior score vs astrocyte activation. C. Average behavior score vs microglia activation.

4.4 Discussion:

4.4.1 Stroke Lesion Volume:

The stroke lesion volumes in canines were assessed using T2 FLAIR MRI scans and segmentations in 3D slicer, revealing significant differences among the subjects. This method aligns with established practices in stroke research, where precise quantification of lesion volumes is crucial for evaluating the extent of ischemia damage and its impact on treatment outcomes. Prior studies have demonstrated the reliability of MRI-based volumetric analysis in stroke models, which is critical for comparing control and treatment groups. (Heiss, Wolf-Dieter, and Olivier Zaro Weber. 2017) Given the substantial variation in lesion sizes, individualized data quantification was necessary rather than averaging.

4.4.2 Hemisphere Volumes:

The enlargement of the ipsilateral hemisphere relative to the contralateral side at 1 day post-stroke is consistent with the well documented inflammatory response following ischemic injury. This swelling, as noted, typically reduces overtime due to tissue atrophy and repair processes. The literature supports that stroke-induced inflammation and subsequent atrophy are common, contributing to volume changes in the affected hemispheres. (Anrather, Josef, and Costantino Iadecola. 2016)

4.4.3 Ventricle Sizes:

The quantification of ventricle sizes revealed the enlargement of the ipsilateral side from day 1 to 28 post-stroke, this is indicative of tissue atrophy and potential ventricular blockage. This finding correlates with studies that showed ventricular enlargement as a common consequence of brain atrophy and changes in brain tissue properties following a stroke (Sayed, Mohammed A., et al. 2020, Zahr, Natalie M., et al. 2013). The significant

increase in ventricle size in the control animal (DSM21) suggests a potential ventricular blockage or other detrimental changes not observed in the treated animals, highlighting the potential benefits of the treatment in preventing such adverse effects.

4.4.4 mRuby2 Expression and Co-labeling:

The high rate of mRuby2 co-labeling with NeuN in both treated and control animals suggests a degree of neuronal targeting by the viral vector, despite the intention to target astrocytes. This outcome may result from the use of high-dose virus injections, which can increase off-target effects. Despite the use of high dose, an increase in NeuN positive transduced cells was identified along with the expression of NeuroD1, suggesting that reprogramming occurred in the treated animals.

4.4.5 Astrocyte and Microglial Activation:

The immune response across all three animals was similar with low to no astrocyte and microglial activation in the contralateral sides and higher activation in the ipsilateral side near the stroke lesion. Interestingly, the treated animals had lower levels of activation in the ipsilateral side than the control animal. This is suggestive of the treatment being able to lower astrocyte and microglia activation, ultimately reducing the neuroinflammation in treated animals. It is possible that with the addition of NeuroD1, some of the astrocytes that would have been activated, were reprogrammed into neurons instead. Activated astrocytes produce proinflammatory cytokines such as interleukin which activate microglia. (Van Wagoner, Nicholas J., et al. 1999, Xiong, Tianqing, et al. 2022) As a consequence of less activated astrocytes, less pro-inflammatory cytokines would be present, likely leading to the reduction in microglia activation that we saw in treated animals.

4.4.6 Behavioral:

The modified neurological severity score used to assess functional recovery indicated that the treated large stroke animal (DSM20) exhibited faster rate and greater recovery compared to the control (DMS21). As expected, the treated small stroke animal had the best behavior scores with fastest and greatest levels of recovery. Although the sample size limits statistical significance, these findings provide a promising basis for further research on the efficacy of the treatment. This observation aligns with studies demonstrating that interventions aimed at reducing inflammation by blunting the activation of astrocytes and microglia, and promoting neurogenesis can improve functional outcomes after stroke, as Lee et al have shown that early intervention and targeted therapies can significantly enhance recovery in post-stroke models.

4.5 Conclusion:

This study evaluated anatomical recovery of stroke through MRI and 3D segmentation. We found that ipsilateral hemisphere enlargement in all animal models was consistent with the inflammatory response typically seen in ischemic injury. Ventricle enlargement was consistent with literature describing post ischemic injury effects, with the control animal showing greater enlargement than treated. This suggested beneficial effects of the treatment on tissue atrophy. Co-labeling studies revealed mRuby2 to be highly co-localized with NeuN in both control and treated, indicating that unintended neuronal targeting took place. This is likely due to the high dose virus injections and resulting in leakage. Although reprogramming likely still occurred in the properly targeted astrocytes that survived, we cannot be confident in attributing the beneficial effects solely to them. The inflammatory response appeared to be upregulated in the control animal while treated animals had less neuroinflammatory activation. This indicates that the treatment

is able to mitigate the astrocyte and microglia activation which could explain the lessened ventricle enlargement in treated animals. The likely mechanism behind this lessened inflammatory response is the conversion of astrocytes into neurons that otherwise would have been activated, leading to less pro-inflammatory cytokine production and less astrocyte and microglial activation. Behaviorally, the treated stroke animals recovered faster and to a greater extent compared to the control. This may also be explained by decreasing microglia and astrocyte activation where decreases in neuroinflammation are associated with improved cognitive performance. Collectively, these findings provide evidence that cell reprogramming with NeuroD1 can modulate the neuroinflammatory response associated with stroke and impact functional recovery in a canine model.

Chapter 5: Ex Vivo Method for Rapid Quantification of Post Traumatic Brain Injury Lesion Volumes Using Ultrasound

5.1 Introduction:

This chapter was adapted from a finished manuscript, published in Journal of Neuroscience Methods. Animal models of TBI play a key role in understanding the pathophysiological process of the injury, and for developing new therapies. Severe TBI can result in lesions within the brain in various animal models, and the quantification of lesion volume is a main outcome measure. Two common approaches to quantify lesion size are by MRI or by sectioning the brain tissue, staining it, and imaging through microscopy to reveal the site of the lesion for cross sectional analysis and reconstruction of the lesion volume (Niesman, Ingrid R., et al. 2014). The MRI approach has limited accessibility due to cost, storage, maintenance, and training for usage, while the microscopy approach is more widely accessible across many labs. For this study we focused on comparison of the widely accessible microscopy approach and its reconstruction of the lesion volume. This reconstruction is generally done manually or by using automated software to calculate the area of the lesion for each individual slice to reconstruct the lesion volume. This traditional histological approach for determining brain lesion volumes is labor and time intensive, typically requiring weeks to months to process the brain tissue samples.

We have recently developed an ultrasound approach to scan the brain ex vivo using the VisualSonics ultrasound imaging system (Model: Vevo 2100) and quantify brain lesion volumes using the free software “3d slicer”. We found that the determination of the lesion volume can be calculated much more efficiently and is highly correlated with lesion volumes calculated via the traditional histological approach. Moreover, using MATLAB (The Mathworks Inc., Natick, MA, USA) scripts we have written and the script,

"SPM12 Software - Statistical Parametric Mapping", the ultrasound scans can be mapped to the Allen Brain Atlas for easy region identification to determine the precise areas of the brain that have undergone degeneration following traumatic brain injury.

5.2 Methods:

5.2.1 Animals:

C57BL/6 male mice were used for this experiment with ages ranging from 2-8 months. Mouse age ranges were due to availability. All mice had TBI induced at day 0, one group of 6 mice was harvested at 1 week post TBI, and the other group of 6 (2 of were euthanized prematurely due to surgical complications) was later harvested at 3 weeks post TBI (Figure 5.1).

Figure 5.1. Timeline for TBI and Behavior.

5.2.2 Surgery to Induce Traumatic Brain Injury:

The tissue used for this quantification was mouse brain that had undergone an in-vivo controlled cortical impact. To induce the traumatic brain injury, mice were anesthetized with 2% isoflurane and placed into a stereotaxic apparatus according to protocols approved by the IACUC guidelines and policies established at the University of Minnesota. The scalp of each animal was shaved and wiped with Betadine and alcohol prep pads to prevent infections, and a midline incision was made to reflect the skin and expose the skull. A craniotomy was performed using a dental drill to expose the underlying brain. The 2mm diameter impactor probe (Leica Stereotaxic Impactor (39463920)) was positioned 1.5mm right and 0.5mm anterior bregma. The impact

parameters were selected to create a moderate brain injury and were performed at a speed of 6m/s, a depth of 1mm, and a dwell time of 100ms. Following the surgery to induce TBI, the opening in the skull was left alone without returning the skull flap to allow for brain swelling. The scalp was then sutured using simple interrupted 4-0 sutures. Animals were then removed from the stereotaxic apparatus and placed in a recovery cage and monitored for recovery. The animals were euthanized 1 or 3 weeks post TBI.

5.2.3 Tissue Fixation:

Upon euthanasia, the mouse was perfused with PBS followed by 4% PFA via transcardial perfusion. The brain was then dissected out and further fixed by immersion in 4% PFA for 24 hours at 4^{o}C. Following fixation, the tissue was submerged in 10%, 20%, and 30% sucrose solutions each for 24 hours at 4^{o}C. The tissue remained in 30% sucrose until eventually being embedded in OCT for cryosectioning.

5.2.4 Ultrasound Methods:

The ultrasound scan was acquired during the 30% sucrose step. The scan was performed by a Vevo 2100 Imaging System with a MS400 transducer attached via stereotaxic arm to a 3D acquisition motor. The brain was removed from the 30% sucrose, placed in a 1.5cm tall container, and submerged in ultrasound gel or water (Figure 5.2). The transducer was then positioned via the stereotaxic arm to generate a full image of one coronal cross section of the brain. A full scan of the brain was then acquired with a step size of 0.1mm. The scan was saved and exported as a DICOM. The scan itself takes less than 1 min while the entire process took roughly 2-10 minutes per brain depending on setup.

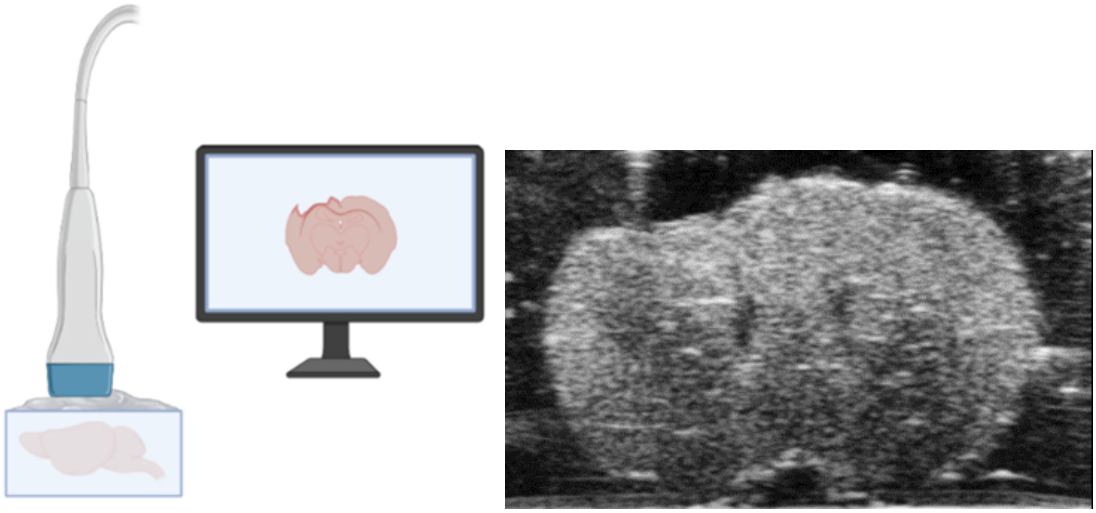

Figure 5.2: Ultrasound Demonstration Model. (sample 1006-1-C-1). Left Panel: schematic of ultrasound transducer in contact with gel in container. Right Panel: Ultrasound Cross Section

5.2.5 3d Slicer Method:

The DICOM file was imported to 3 slicer for analysis (Figure 5.3). An initial segmentation of the entire brain was generated with the threshold function with a range of max intensity to ~1/4 max intensity and manual trimming corrections. The optimal values for this threshold varied greatly depending on the scan. A new segmentation was then generated for non-solid matter with the threshold function with a range of 0 to ~1/4 max intensity. This non-brain segmentation was then manually trimmed in the 3D model mode as well as in 2D so that it only filled the missing space within the lesion volume (Figure 5.3b). Smoothing was then performed at 0.01-0.3 to fill holes within both segmentations and remove protrusions. The two segmentations could then form a binary 3D model of the sample (Figure 5.3c) and their volumetric dimensions could be exported into whatever software desired for statistical analysis. These values were exported into an Excel spreadsheet in which averages and standard deviations were calculated. This process took roughly 1.5 hours per brain.

5.2.6 MATLAB SPM Mapping Method:

The scan was additionally mapped onto a Magnetic Resonance Image (MRI) reference template from the Allen Brain Atlas (Figure 5.3g). This process is not required for total lesion quantification, but it does allow for the identification and quantification of specific regions of brain affected by brain injury. To co-register the ultrasound image with the Allen Mouse Brain Atlas, in house MATLAB scripts were written to properly format the scan and strip all non-brain substances. These scripts multiplied the binary 3D Slicer brain segmentation with the ultrasound scan to strip all the gel and air from the image. The stripped scan was then co-registered to the MRI reference using the co-register function from the free access MATLAB script, “SPM12 Software - Statistical Parametric Mapping” while also applying that same transform to the lesion segmentation.

In order to then normalize both the scan and the lesion segmentation to the Allen Brain Atlas, the co-registered lesion segmentation was added to the co-registered ultrasound scan (Figure 5.3e). This gray matter lesion filling was performed, so that the lesion segmentation itself would also be normalized. This lesion filling technique has been used and shown to be effective in improving segmentation accuracy and tissue classification (Battaglini, Marco, et al. 2012; van der Weijden, Chris W. J., et al. 2022). The combined image was then normalized (Figure 5.3f), and the same transformation was applied to the original co-registered images. Normalization allowed for any given x-y-z coordinate to be rapidly identified as a specific brain region as well as the volume lost per region to be calculated which provides even more precise information on recovery. These identifications and calculations were conducted by in house generated MATLAB scripts. This process took roughly 30 minutes per brain. The full pipeline is shown in Figure 5.4.

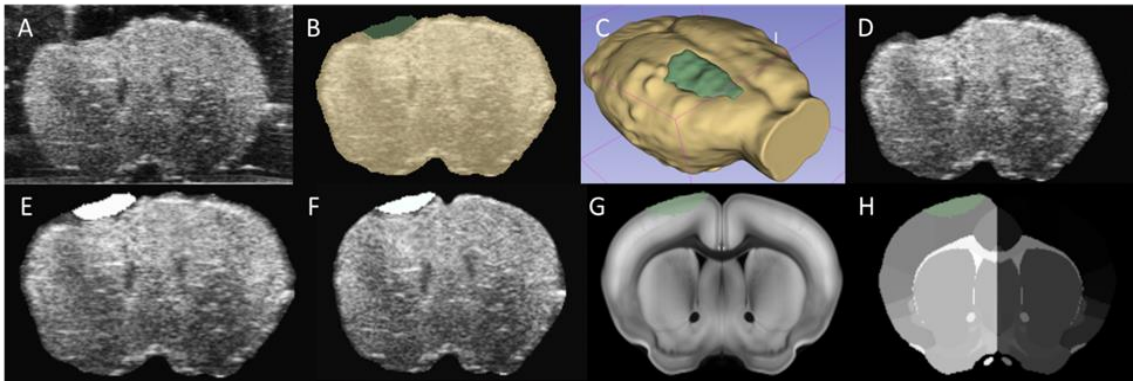

Figure 5.3: Modeling and Mapping of Ultrasound Scan. A- Original Ultrasound Scan. B- TBI Lesion Segmentation and Brain Segmentation. C- 3d Model of Segmentations. D- stripped ultrasound scan E- co-registered and filled ultrasound scan. F- Normalized combined scan. G- Allen Brain MRI Atlas with Lesion Overlapped. H- Allen Brain Annotation Atlas with Lesion Overlapped.

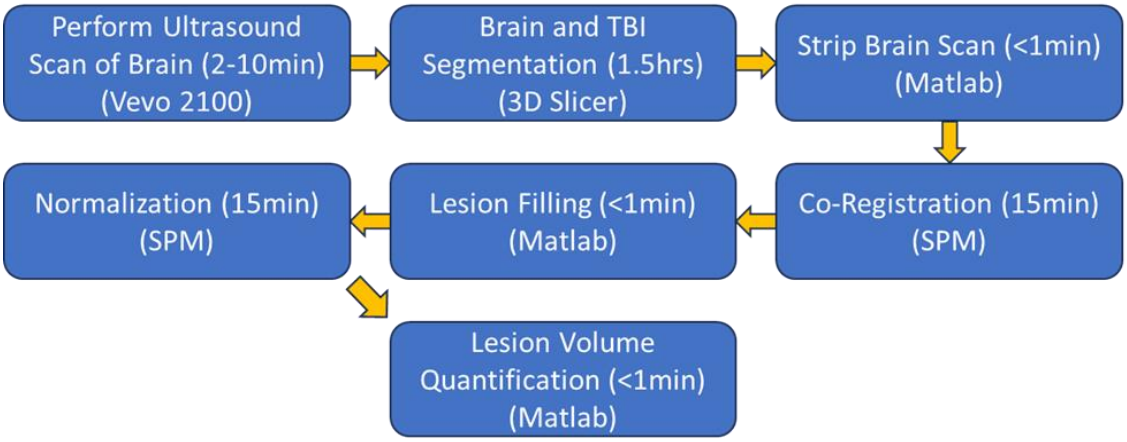

Figure 5.4: Pipeline for Processing a Full Ultrasound Brain Scan. Obtaining total TBI lesion volume, and volume lost per region.

5.2.7 Microscopy Validation:

To validate the accuracy of the TBI lesion volume calculated through Ultrasound, we also calculated it through the traditional means of cryosection and microscopy. The portion of brain affected by TBI was cryosection in 20um slices on glass slides. This process took ~2 hours per brain. The unstained slides were then imaged through microscopy, in which every 8th slice was scanned and the TBI lesion on each image was annotated in QuPath which provided the cross-sectional area (Figure 5.5A). That area was then multiplied by the slice thickness and number of slices between each imaged

slice (8 Slices * 20um) to produce a finite volume. All those volumes were then added together to determine the total lesion volume. The scanning process took ~1 hour per mouse brain, and the manual annotation process took ~3 hours per mouse brain. The full pipeline is shown in Figure 5.5B.

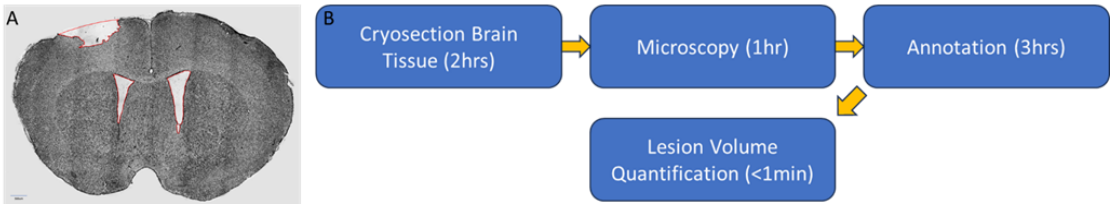

Figure 5.5: Microscopy Pipeline. A: Cryosectioned unstained slice annotated in QuPath to highlight TBI Lesion (Sample 1009-1-C-3). B: Traditional Pipeline for microscopy estimation of TBI lesion volume (excluding staining).

5.2.8 Beam Walk:

To analyze neurological deficits induced by the TBI, animals were trained on a beam walk task prior to CCI procedure. Training consisted of 4 training days starting 5 days prior to TBI. Each training day the animals would be tested on the beam walk task. On one day prior to TBI their scores were recorded as baselines. After TBI, animals were tested again 1 day post injury (dpi), 6 dpi, 13 dpi, and 20 dpi. Additionally, the mice were re-trained to ensure consistency of results on 5 dpi, 12 dpi, and 19 dpi. Testing consisted of placing the animal in a safe box on the ending side of the beam walk for 15 seconds to acclimate the animal. Afterwards the animal would be placed at the starting side of the beam walk in which a bright light was present to prompt the animal to move across to the darker side with the safe box. The beam was a rectangular 1 in by 1 in shape with a starting line and end line 2 ft apart. Time to cross would not start until the animal fully crossed the starting line and would not end until the animal fully crossed the end line.

5.2.9 Statistical Analysis:

Standard deviation, standard error, averages, and trendline values were all calculated using preloaded Excel formulas. Significance between 1- and 3-week volumes missing per region was calculated using two-sample t-test. Additionally, significance between behavior at different days post injury was also calculated using two-sample t-test. T-tests were performed using a combination of Excel and MATLAB.

5.3 Results:

5.3.1 Accuracy and Precision:

Comparing the lesion volumes calculated through Ultrasound to the same lesions calculated through microscopy, a trendline with intercept set to 0 can be drawn (Figure 5.6). The trendline has a high R^2 value which shows a high level of correlation between ultrasound and traditional slice estimation. Additionally, the slope is near 1 which shows a high level of accuracy between ultrasound and traditional slice estimation. Performing ANOVA analysis on this yields a p-value of 0.0149, providing statistically significant evidence that there is a relationship between ultrasound quantified TBI lesion size and microscopy quantified lesion size. The accuracy in terms of margin for error of both of these approaches is very similar as the slice size for Ultrasound is 100 um and the thickness per area calculated through microscopy was 8 Slices * 20um = 120 um. While the correlation between the two methodologies is very high, there are still some variations between them. This may be a result of error in the manual annotation process of microscopy/ultrasound or physical changes to the brain post ultrasound scan and pre microscopy. The total time required to process the lesion volume, without region identification, via the common microscopy approach was ~6 hours per brain, excluding freezing and staining of the tissue. The ultrasound approach to process the lesion

volume, without region identification, on the other hand is approximately 3 times faster, with its total time being ~ 2 hours.

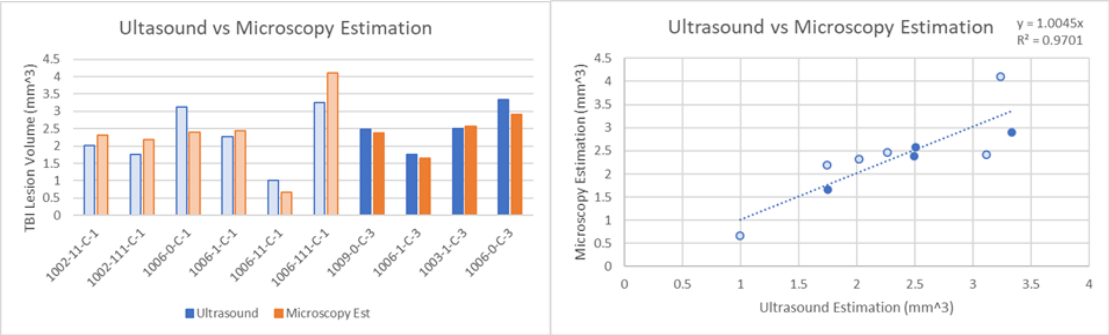

Figure 5.6: Direct Comparison of TBI Lesion Volume Estimations. From ultrasound and microscopy. Left Panel – Ultrasound and Microscopy estimated volumes for each mouse subject. 1 week post TBI shown in lighter colors and with end label designation -1. 3 weeks post TBI shown with darker colors and end label designation -3. Right Panel – Trendline with y intercept=0 and Microscopy Estimation / Ultrasound Estimation = slope. P-value = 0.0149.

5.3.2 3D Model Mapping:

With the generation of the 3D model and mapping of that model, the exact regions lost due to the TBI lesion can be identified (Figure 5.7). In the example shown, the TBI clearly targeted the primary and secondary motor areas as well as some of the primary somatosensory areas. The precise volume lost per region was calculated (Figure 5.8) and it shows that this model typically impacts the primary motor area layer 2/3 the greatest. Additionally, we can see there is no statistically significant difference between 1- and 3- weeks post injury in terms of missing volume per region. This implies that for this model and these time points, there is no significant tissue regain or further tissue loss.

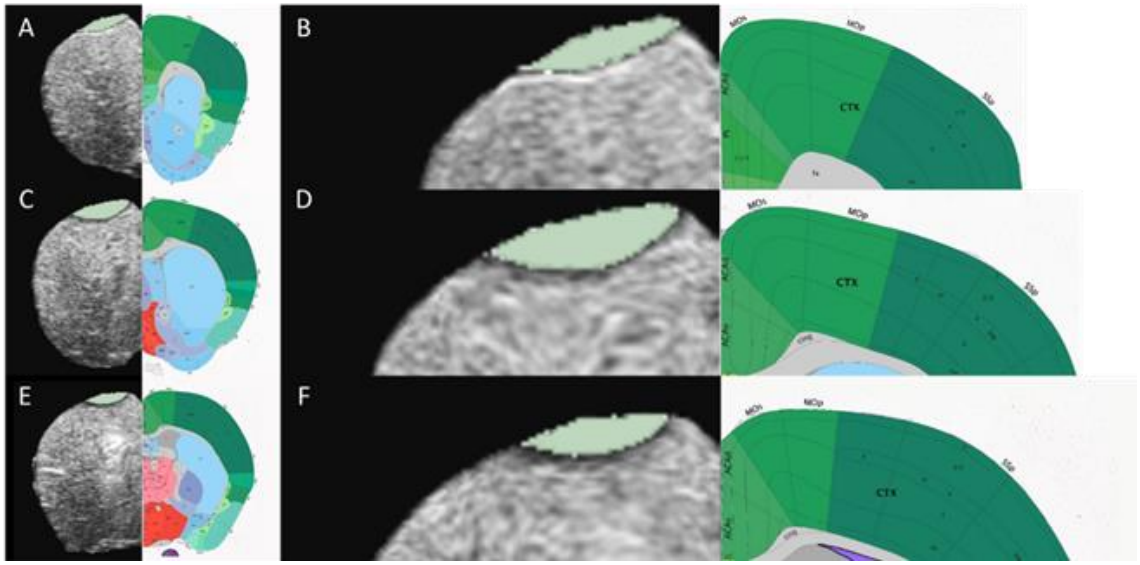

Figure 5.7: Side by Side Comparison of Normalized Ultrasound Scan and Allen Brain Annotation Atlas. Acronyms listed in Table 5.1. A-B: Anterior slice of TBI lesion. C-D: Middle slice of TBI lesion. E-F: Posterior slice of TBI lesion.

Acronym	**Name**
MOp1	Primary motor area, Layer 1
MOp2/3	Primary motor area, Layer 2/3
MOp5	Primary motor area, Layer 5
MOp6a	Primary motor area, Layer 6a
MOs1	Secondary motor area, layer 1
MOs2/3	Secondary motor area, layer 2/3
MOs5	Secondary motor area, layer 5
MOs6a	Secondary motor area, layer 6a
SSp-bfd1	Primary somatosensory area, barrel field, layer 1
SSp-bfd2/3	Primary somatosensory area, barrel field, layer 2/3
SSp-ll1	Primary somatosensory area, lower limb, layer 1
SSp-ll2/3	Primary somatosensory area, lower limb, layer 2/3
SSp-ll4	Primary somatosensory area, lower limb, layer 4
SSp-ll5	Primary somatosensory area, lower limb, layer 5
SSp-ll6a	Primary somatosensory area, lower limb, layer 6a
SSp-ul1	Primary somatosensory area, upper limb, layer 1
SSp-ul2/3	Primary somatosensory area, upper limb, layer 2/3
SSp-ul4	Primary somatosensory area, upper limb, layer 4
SSp-tr1	Primary somatosensory area, trunk, layer 1
SSp-tr2/3	Primary somatosensory area, trunk, layer 2/3
SSp-tr4	Primary somatosensory area, trunk, layer 4

SSp-tr5	Primary somatosensory area, trunk, layer 5
SSp-tr6a	Primary somatosensory area, trunk, layer 6a
SSp-un1	Primary somatosensory area, unassigned, layer 1
SSp-un2/3	Primary somatosensory area, unassigned, layer 2/3
RSPagl1	Retrosplenial area, lateral agranular part, layer 1
RSPagl2/3	Retrosplenial area, lateral agranular part, layer 2/3
RSPagl5	Retrosplenial area, lateral agranular part, layer 5
VISa1	Anterior area, layer 1
VISa2/3	Anterior area layer 2/3

Table 5.1: List of Allen Atlas Brain Acronyms.

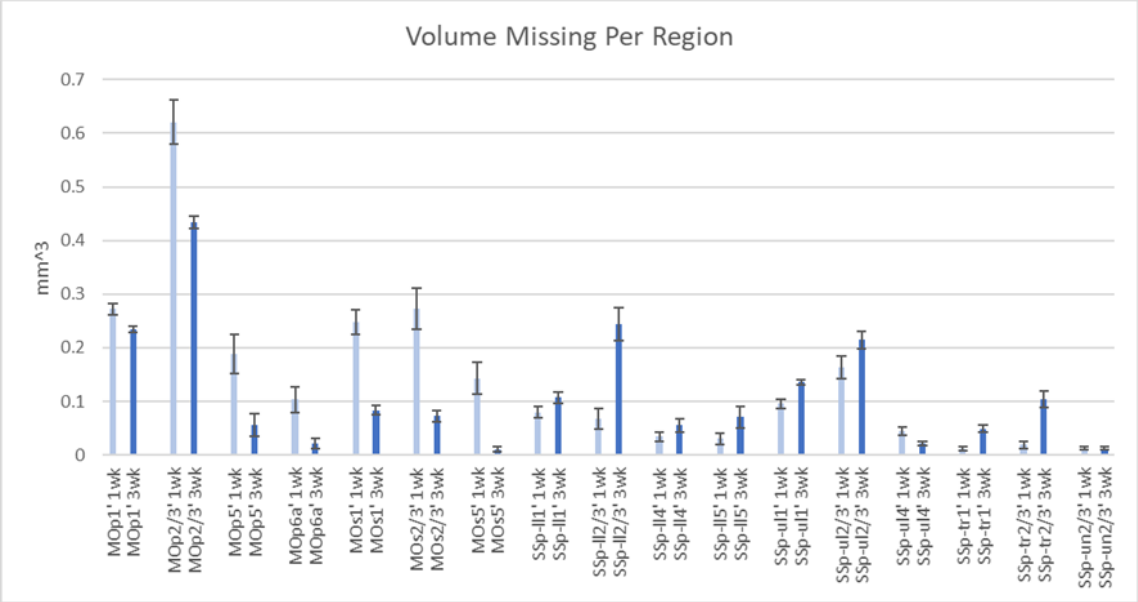

Figure 5.8: Volume Missing Per Region. Quantified through Ultrasound Estimation. Regions with average loss below .001 on 1 and/or 3 weeks not included.

5.3.3 Behavior:

The TBI model used for this study targeted the motor and sensory cortex. As such, the limbs contralateral to the injury were greatly impaired. Behavioral analysis via the beam walk task before and after TBI shows a statistically significant increase in time to cross one day post TBI (Figure 5.9). 6 dpi and longer however, the animals begin to show recovery. This recovery, however, does not correlate with any statistically significant decrease in TBI lesion size 3 weeks post injury. This lack of correlation indicates that the

recovery of neurological function is due to the plasticity of the brain rather than gross anatomical recovery of the TBI lesion.

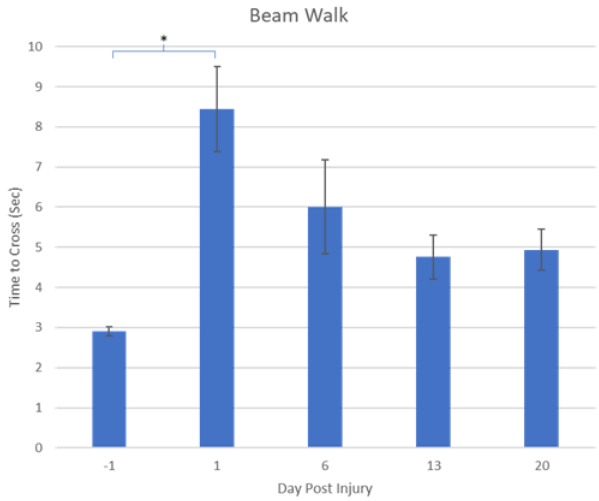

Figure 5.9: Behavioral Data Pre and Post TBI. A significant increase (p=0.0152) in time to cross is observed 1 day post TBI, by *. The increase in time to cross slowly decreases the longer time goes on.

5.3.4 TBI Lesion Volume vs Behavior:

In order to gain a better understanding of the relationship between TBI lesion volume/location and neurological deficits, comparisons were drawn between them. In general, mice with smaller lesions had smaller maximum deficits, referring to the difference between maximum time recorded to cross and the baseline (Figure 5.10). Mice with smaller lesions also had smaller final deficits, referring to the difference between the final recorded time to traverse the beam and baseline. Larger TBI lesions typically resulted in similar amounts of tissue loss for primary motor area layers 1 and 2/3; primary somatosensory area, lower limb, layer 1 and 2/3; and primary somatosensory area, upper limb, layer 1 and 2/3 when compared to smaller lesions. However, larger lesions typically resulted in tissue loss across many additional regions that smaller lesions did not always affect. This implies that the increase in deficit is due to damage in these additional regions rather than greater damage to the same regions

affected by the smaller lesions. The additional regions effected were often located deeper in the brain rather than anterior/posterior or medial/lateral to the more often effected regions. This implies that the greater lesion volume may be due to the impactor tip reaching a greater depth in those mice. While the surgical procedure is the same for each mouse, some variation between surgeries is expected. The additionally effected regions mostly consist of motor and sensory regions, however some retro splenial and visual areas were affected as well. These additionally affected regions suggest that those mice may have further deficits in cognition and sight. This, however, was not verified through any behavioral tests.

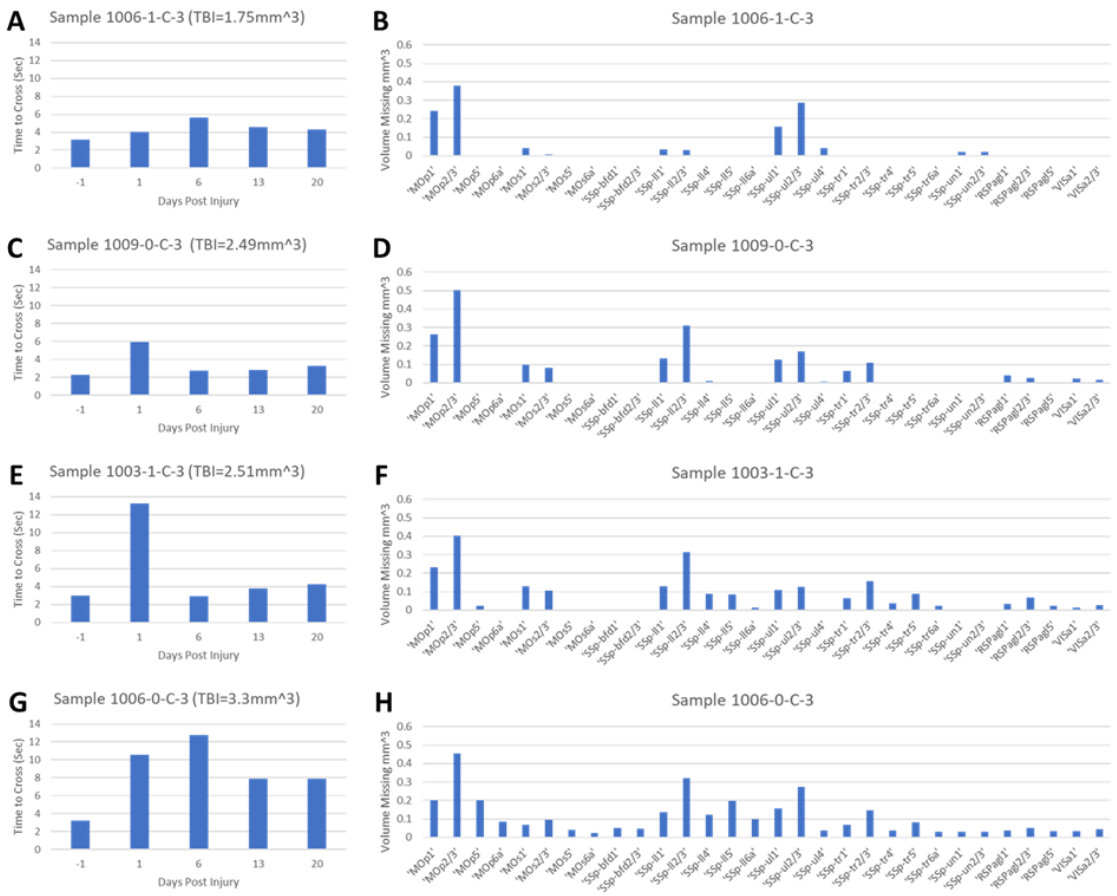

Figure 5.10: Individual Beam Walk Results. Ordered by ultrasound quantified TBI lesion size, and individual TBI location results. All regions with tissue loss included.

A-B: Sample 1006-1-C-3: TBI lesion volume of 1.75 mm^3.

C-D: Sample 1009-0-C-3: TBI lesion volume of 2.49 mm^3.

E-F: Sample 1003-1-C-3: TBI lesion volume of 2.51 mm^3.

G-H: Sample 1006-0-C-3: TBI lesion volume of 3.30 mm^3.

From the TBI lesion volume and behavioral deficits, we can also generate trendlines to determine if there is a significant correlational relationship between these two parameters. The same trends between lesion volume, maximum deficit, and final deficit mentioned earlier can be seen when comparing them directly (Figure 5.11). When making trendlines for these comparisons with intercepts set to 0, assuming no deficit with no injury, we obtain regressions that suggest TBI lesion volume can explain 87.5% of the maximum deficit and 78.9% of the final deficit. However, due to the sample size, these relationships cannot be proven as statistically significant. If this experiment were

repeated, power analysis shows that a sample size of 8 would be sufficient to prove statistical significance for both relationships. All behavioral, ultrasound, and microscopy data are available upon request of the author.

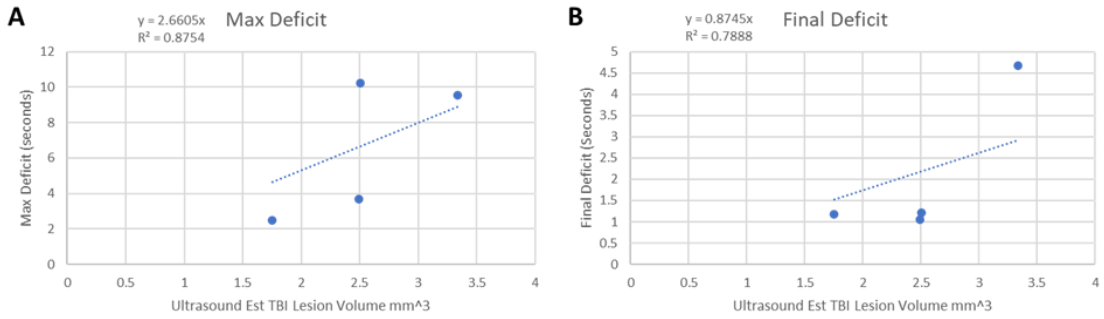

Figure 5.11: Trendlines. A: Trendline using ultrasound estimated TBI lesion volume to predict maximum deficit. Regression equation: Y=2.6605x, R^2=0.8754, P-value=0.4975. B: Trendline using ultrasound estimated TBI lesion volume to predict final deficit. Regression equation=Y=0.8745x, R^2=0.7888, P-value=0.5936.

5.4 Discussion:

5.4.1 Significance:

In early stages of TBI, the site can form hematomas and/or contusions which can be classified as “mass lesions” (Agarwal, Nitin., et al. 2020). This is caused by the initial impact which ruptures blood vessels and damages neuronal tissue as well as the secondary injury which results in tissue death overtime from ischemia and the inflammatory response. Those lesions can disable the neuronal activity within them and lead to loss of brain volume (Mckee, Ann C., and Daniel H. Daneshvar., 2015). The volume of the lesion can be correlated with degree of loss of neurological function in the form of cognitive and motor deficits (Washington, Patricia M., et al. 2012).

Many neurological diseases, disorders, or injuries also result in lesion volumes which similarly can be correlated with loss of neurological function. Hemorrhagic and ischemic stroke both lead to ischemia in the injury site which typically generates a brain lesion. Huntington’s disease can also generate lesions via the progressive degeneration

of neurons (National Institute of Neurological Disorders and Stroke. 2023). Multiple sclerosis can generate lesions through the demyelination and inflammation in the brain (Wattjes, Mikes P., et al. 2015). All these lesions generated from different diseases can be correlated with the severity of the diseases and loss of neurological function (Alexander, Lisa D., et al. 2010).

Current approaches for quantification of brain lesion volume rely on sectioning, staining, microscopy, and image processing to calculate the total volume (Washington, Patricia M., et al. 2012). There are several methods that exist to increase the efficiency of this process such as automated sectioning, automated imaging, and automated image processing, however, not all labs have access to these conveniences. This ultrasound approach provides a faster method for lesion volume quantification than the common approach and may be of great benefit to labs with access to ultrasound imaging but not automated sectioning and imaging technologies. Additionally, this approach has the potential to be modified similar to the cranial window ultrasound approaches to work in living animals (Macé, Émilie, et al. 2018). Which would allow for real time analysis of TBI lesion development and recovery.

The ultrasound approach also provides a 3D model whereas microscopy typically does not. This 3D model, paired with an appropriate reference atlas, can be used to identify which specific regions of the brain are altered or lost due to injury or disease. Knowing the specific regions affected more or less than others can help direct future research by targeting those more affected regions more accurately. In combination with more specific analysis of neurological deficits, this approach could be used to further explore how damage to non-motor and non-sensory areas results in certain deficits. For example, Barnes maze training could help determine how TBI lesion volume and damage to retrosplenial areas specifically would result in cognitive deficits.

Additionally, regions that regularly interact with the affected regions could be identified using this information and existing reports of brain connectome data. Several reports have assessed brain connectivity using resting state MRI (rs-fMRI) or Ultrasound in both control and TBI models (Huang, Shiliang, et al. 2021; Ravi, Sakthivel, et al. 2022; Macé, Émilie, et al. 2018). Specifically, Huang et al. demonstrated that with a TBI targeting the left forelimb primary sensorimotor cortex the caudate putamen, the supplementary somatosensory cortex, and the sensorimotor cortex all showed decreases in symmetrical bilateral functional connectivity. Our examples in Figures 5.6 and 5.7 show significant loss in primary and secondary motor areas as well as primary somatosensory lower limb areas. As such we could expect this model to express similar brain connectome and behavioral deficits seen by Huang et al. but potentially with more deficits to the lower limb rather than forelimb and additional alterations to the respectively connected regions. For Ultrasound, Mace et al, displayed the potential to assess connectivity in vivo with the use of a cranial window and ultrasound doppler. For labs without access to these technologies or desiring fewer surgical procedures, our ex vivo ultrasound TBI lesion quantification provides a means to determine the severity and precise location of TBI damage. Paired with research from papers such as these, behavioral data could be correlated with region specific data and future experiments could be planned out accordingly.

5.4.2 Innovation:

MRI scans have been used to examine TBI lesions since 1986 and more recently in 2013, contrast enhanced Ultrasound has been used to examine it as well. (Weiss, Nicolas, et al. 2007; He, Wen, et al. 2013) These approaches however are not accessible to all labs and sometimes require surgical procedures such as craniotomies

to generate a usable image. The simple ex-vivo ultrasound approach we have developed allows for greater accessibility and greater flexibility in research planning as it can be done any time post euthanasia and does not require an additional procedure on a live mouse.

5.4.3 Limitations:

While this study was able to provide an innovative method for TBI lesion quantification, there are several limitations. The behavioral data assessed only general motor deficits rather than specific limb or non-motor skills. As such, comprehensive results cannot be obtained, and only general conclusions can be drawn from the affected regions and their corresponding behavioral deficits. Additionally, the developed ex-vivo ultrasound method was compared only to microscopy rather than in-vivo routes such as MRI and Ultrasound through cranial windows. If compared to these additional routes, this method may be further validated.

5.4.4 Future Work:

The research in this project supports that this method is comparable to other easily accessible routes, however it does not explore other routes such as MRI. Future work that could bolster the validity of this approach, would be to run ultrasound, microscopy, and MRI scans on the TBI modeled mouse brains and compare lesion volumes quantified from all. Additionally, to account for individual mouse brain size variability, these quantifications should be further corrected by considering the volume of the entire brain. This research did not explore all categories of behavioral deficits, allowing for only general comparisons between affected brain regions. To further explore the connections between region specific TBI damage and specific deficits, experiments could be set up to induce a variety of TBI's based on location and a variety of behavioral assessments.

5.5 Conclusion:

This ultrasound approach to quantify TBI lesions has been shown to be much faster than the common microscopy approach. The accuracy of this ultrasound approach is also consistent with the common microscopy approach and has a similar margin of error considering the number of volumes calculated per slice thickness. The 3D model generated from the ultrasound approach also provides invaluable information that can be used to direct further research and further interpret existing results. After the scan is complete, the tissue can still be embedded for IHC staining, so there are no loss of histological data collections in taking this approach. This approach should prove quite useful to any labs researching injuries, diseases, or disorders that result in brain lesions.

Chapter 6: Functional Neural Connectivity of the Mouse Brain using Photoacoustic Ultrasound

6.1 Introduction:

The functional connections between different areas of the brain provide the underlying basis of brain state and behavior. The network of interconnections can be visualized across the entire brain using a variety of approaches. Researchers can analyze functional neural networks through the use of brain connectomes (Bullmore, Ed, and Olaf Sporns. 2009; Fox Michael D. 2018; Bazinet, Vincent, et al. 2009). Brain connectomes represent either physical connections of axons to dendrites or functional connections of shared activity within the brain. Activity is derived from oxygen usage, which correlates to the firing of neurons. Neuronal oxygen consumption triggers increased blood supply to active brain regions. Thus, active areas in the brain are typically surrounded by a greater amount of oxygen rich blood (Heeger, David J., and David Ress. 2022).

Functional magnetic resonance imaging (fMRI) can detect blood oxygenation levels based on the oxygen bound or unbound state of hemoglobin. The bound form of hemoglobin, oxyhemoglobin, has no unpaired electrons, which makes it diamagnetic. The diamagnetic state has no significant effect on the magnetic resonance (MR) signal. While the unbound form of hemoglobin, deoxyhemoglobin, has four unpaired electrons, which makes it paramagnetic. The paramagnetic state leads to a decreased MR signal in regions with more deoxyhemoglobin (Ogawa, S., et al. 1990). Ultimately, oxygen rich ROIs produce a more intense signal than lower oxygen areas. Oxygen activity over time can be identified, recorded, and used to generate a brain connectome (Zerbi, Valerio, et al. 2015). However, MRI is expensive, time and skill intensive, and often not portable (Arnold, Thomas Campbell, et al. 2023). As a result, this method remains inaccessible to many researchers, labs, and clinicians.

PAU is much cheaper, quicker, and typically more portable than MRI machines (Joshi, Deepa, and D. S. Mehta. 2022; Wang, Lihong V., and Junjie Yao. 2016). Similar to fMRI, PAU can detect blood oxygenation. Oxygen levels are detected by using a pulsatile emission of 750 and 850 nm light, which is absorbed by hemoglobin. The pulsatile light heats and cools the molecules that absorb it, leading them to expand and contract. The expansion and contractions result in pressure waves that can be detected via the PAU. Oxyhemoglobin tends to absorb more light at 850 nm, while deoxyhemoglobin absorbs more at 750 nm. By alternating the PAU emission wavelengths to target deoxyhemoglobin or oxyhemoglobin and comparing the resulting pressure intensities, SO2 levels can be calculated (Li, Changhui, and Lihong V. Wang. 2009).

Prior research groups have shown that brain activity and even brain connectivity can be detected using PAU (Zhang, Pengfei, et al. 2017, Nasiriavanaki, Mohammadreza, et al. 2013). Their results showed many bilateral correlations in regions such as limbic, somatosensory, and hippocampal which have all been established in prior literature. These studies used a repetition time of 10Hz, while viewing a single coronal or axial slice. In our study, rather than using a single coronal or axial slice, we used whole brain PAU scans, developed a pipeline to map them, and generated whole brain connectomes from them. We validated the identified connections using fMRI generated brain connectomes and prior literature.

6.2 Methods:

6.2.1 Animals:

Female CD1 4-8 week old mice were used in this experiment. The animals were divided into three groups: group A: 3 mice used to generate the base PAU connectomes setting,

group B: 3 mice used to generate the fMRI connectomes and group C: 4 mice used to conduct the four PAU connectomes under alternate PAU settings.

6.2.2 Ultrasound Acquisition:

CD1 mice were anesthetized with isoflurane (1-5%), then a depilatory cream was used to remove the hair on the head of the animal. All ultrasound and PAU imaging was performed with the Vevo F2 LAZR-X Imaging System (FUJIFILM, VisualSonics, Inc., Toronto, Canada). Each animal was mounted in a stereotactic frame custom-made to work with the mouse imaging platform, which is heated to maintain body temperature and has integrated ECG and respiration monitoring. The UHF29x transducer (center frequency 21 MHz) was used in combination with a linear stepper motor to acquire coronal images of the mouse brain with matrix voxels= 0.029<->0.036mm x 0.028<->0.036mm x 0.5<->2mm (medial/lateral, superior/inferior, anterior/posterior), and matrix dimensions= 384x(352<->304)x26. The sampling rate was performed at 1/42<->1/26 Hz depending on the step size varying from 0.5<->2 mm respectively. Simultaneous PAU and ultra-high frequency ultrasound images were acquired with OxhyHemo Mode, which uses images taken at two wavelengths (750nm and 850nm) to calculate the oxygen saturation of the blood at each pixel and display this as a parametric map. Images were exported separately as B-mode ultrasound images and PAU OxyHemo images as a TIFF stack.

6.2.3 fMRI Acquisition:

All MR experiments were performed using a horizontal 9.4 T magnet interfaced to a Varian DirectDrive console. Mice were anesthetized with isoflurane (1-5%) and secured in an animal cradle. Radio frequency transmission and signal reception were carried out using an RF surface coil with a 1.4-2.0 cm loop diameter (High Field Imaging, Minneapolis, MN). T2 weighted anatomical images were acquired with repetition/echo time

(TR/TE) = 4000/10 ms, matrix voxels= 0.25mm x 0.25mm x 0.5mm (medial/lateral, superior/inferior, anterior/posterior), and matrix dimensions= 96x48x16. Gradient echo (GE)-echo planar imaging (EPI) based fMRI images were obtained with those same parameters.

6.2.4 Scan Mapping and Processing:

Ultrasound scans were exported in the form of .tif files, each representing a single slice at a single time point. An in-house MATLAB script was created to convert the .tif files into a 4D matrix including xyz coordinates, as well as time. The resulting 4D matrix was permuted and flipped to the desired orientation, matching the Allen Brain Atlas. After orientation, the matrix was saved as a .nii file and given the proper dimensional information. The same procedure was performed on the PAU data.

fMRI and MRI data were exported after acquisition as .nii files. At this point, ultrasound, PAU, MRI, and fMRI data were all in the same format and spatial orientation allowing them to be processed in the same way. With proper orientation and dimension information, copies of the Allen Brain MRI and Annotation Atlas were scaled to match the dimensions of the ultrasound and MRI scans. Tissue probability maps (TPM) were also generated from the scaled Annotation Atlas'. The fMRI and PAU images were corrected for motion using "SPM12 Software - Statistical Parametric Mapping" (SPM12) re-alignment with Quality=.9; Separation=.5; Smoothing=1; Num Passes= "Register to 1st"; Resliced Images="All Images (1..n)"; and Masking="Don't Mask Images".

The ultrasound and MRI scans were analyzed using 3D Slicer to create segmentations for all brain matter. To generate these segmentations, manual outlining of the brain tissue was used followed by using "grow from seeds" and smoothing functions. Those segmentations were then saved as binary .nii files. In MATLAB, the segmentations

were then multiplied element wise to each timepoint of their corresponding scans and to the corresponding realigned fMRI/PAU scans. This stripped all non-brain material from the scan. The resulting stripped ultrasound and MRI scans were then co-registered to the Allen Brain MRI Atlas via SPM12 with separation = .1, while keeping the fMRI and PAU scans in alignment. After registration, the ultrasound and MRI images were normalized to the custom TPMs using SPM12 normalization and that transformation was applied to the PAU and fMRI scans. The parameters alternated from default were Affine Regularization=European Brains, sampling distance = .1, and bounding box and voxel sizes relevant to the scaled atlas's. The fMRI and PAU images were then gaussian filtered using a FWHM equal to 3 times the average voxel width. Lastly, the fMRI data was temporally filtered via a highpass butterworth filter with a filter order of 2 and cutoff frequency of .01Hz.

6.2.5 Scan Connectome Generation:

Prior to connectome generation, the annotation matrix was scrubbed such that certain subregions were lumped into larger regions. This ensured the same regions would be considered when comparing the ultrasound generated connectome with an MRI-generated connectome. Additionally, this method could be used to ensure regions smaller than the voxel size would not be considered. With both the ultrasound and photoacoustic data registered to the Allen Brain Atlas, the oxygenation signal was then averaged for each respective region represented in the scrubbed annotation matrix. Those region-averaged signals were then correlated against each other within the annotation matrix to produce an adjacency matrix.

6.2.6 Ultrasound Connectome Accuracy Validation:

To validate the accuracy of the ultrasound brain connectome generated, we compared it to a traditional fMRI generated connectome as well as conducted a search of the scientific literature regarding reports of anatomically and functionally identified neuronal connections. A comparison to the traditional fMRI-generated connectome was performed by calculation of the mean squared error for all correlations. This was calculated for each connectome generated. Literature analysis was performed only on the averaged connectome generated from 3 mice scans with step sizes of 0.5mm and a sampling rate of 1/42 seconds.

6.2.7 Scientific Literature Analysis:

To further investigate the validity of the PAU connectome, ROIs with a signal correlation value greater than 0.6 were identified and searched for physical or functional connectivity. Physical connections were identified using the Allen Connectivity Atlas. Pubmed searches were conducted in order to determine if the suspected connected ROIs shared a previously established functional network.

6.3 Results:

6.3.1 Mapping & Filtering:

To ensure the scans occupied the same 3D space, all scans were mapped to the Allen Brain Atlas. Four types of scans were acquired, two structural scans including MRI and ultrasound, and two functional scans including fMRI and PAU. These scans were successfully mapped to the Allen Brain Atlas (Figure 6.1). The PAU scan acquired in the initial study had a finer spatial resolution than the fMRI scan with a voxel size of 0.000407529045 mm^3 compared to 0.03125 mm^3, yet there is a clear distinction between structural image detail in the PAU scan compared to the fMRI scan. These

structural image detail differences can be attributed to differences in the point spread function, noise to signal ratio, and signal sensitivity due to alternate acquisition methods (Chen, Chuan, et al 2020). PAU images acquired at greater depths and/or with structures between the points of interest and the transducer (such as the skull), will alter the point spread function and the noise to signal ratio can increase. Additionally, due to PAU's simultaneous acquisition of deoxy and oxy hemoglobin, it has the potential of greater sensitivity which may explain its focus on image contrast over structural detail. In the ultrasound, fMRI and MRI scans, there is a clear distinction between the cranial cavity and non-brain matter. However, this is not true of the PAU scan. We can be certain though that the stripped and mapped PAU scan reflects the blood oxygenation signals within the cranial cavity as it was aligned with the ultrasound scan during stripping. The normalized ultrasound scan is significantly stretched/compressed to fit the atlas, which indicates scaling issues in the original scan and/or anatomical differences between the ultrasound scan and the atlas. Mild stretching/compressing is also observed in the normalized MRI and fMRI scans, indicating those same issues to a lesser extent. These issues are intrinsic to the normalization process, which ensures the scans are in alignment despite scaling or anatomical differences.

Figure 6.1: Ultrasound Processing Images. A-B: Ultrasound Scan Pre and Post Mapping. (Animal_ID:02-18-17-00-03). C-D: PAU scan pre and post mapping. E: Allen Brain Annotation Atlas. F-G: T2 MRI scan pre and post mapping (Animal_ID:run-29). H: Allen Brain MRI Atlas. I-J: fMRI scan pre and post mapping

To explore a variety of processing parameters, data sets were filtered with different sampling rates, sample sizes, as well as with and without temporal smoothing. The fMRI and PAU data both had standard motion correction applied through SPM realignment and gaussian smoothing with full width at half maximum equal to three times the average voxel length. Temporal smoothing was applied to the fMRI data through a high pass butterworth filter with cutoff .01 Hz. Due to the sampling rate and temporal sample size, the butterworth filter could not be applied to the PAU data and result in viable data.

The original sampling rate of the PAU scans were 1/42 Hz in which a total of 8 time samples were acquired while the fMRI scans were acquired at 1 Hz with a total of 300 samples for one imaging run. We decided to compare samples with the same parameters, and thus a copy of the original fMRI data was downsampled from 1Hz to 1/42 Hz and only the first 8 data points of that downsampled data were kept.

6.3.2 Alternate Filtered Connectomes:

The downsampled, non-temporally filtered, and temporally filtered fMRI data as well as the PAU data all had adjacency correlation matrices generated from them based on the ROIs present in the fMRI area scanned limited by the fMRI surface coil. Those adjacency matrices were averaged accounting for the 3 scanned mice and the correlation matrices were then compared (figure 6.2). The correlation matrix generated from the fully filtered fRMI data was presumed to be the most accurate and most devoid of false positives, therefore acting as the control for the PAU generate connectome. We see significantly more functional connectivity in the PAU generated connectome with 4046 connections (r=having a correlation value above 0.5) compared to the fully filtered fMRI connectome only having 62 connections (r=with a correlation value above 0.5). The mean squared error (MSE) between the PAU and fMRI connectome was 0.0444. This result suggests either many additional false positives in the PAU connectome or a greater sensitivity of PAU allowing for identification of connections unidentifiable through fMRI.

Due to the temporal sample size, the PAU data could not be temporally filtered. As such we expected it to share greater similarities with non-temporally filtered data. When PAU data was compared to non-temporally filtered data, a smaller MSE of .0306 was found. As the PAU data additionally had a lower sampling rate and smaller temporal sample size, we would expect fMRI data with the same parameters to generate a

connectome most similar to the PAU data. However, this is not the case as the resulting connectome had a MSE of .0356. This implies that when downsampled the fMRI data may have some artifacts introduced or the inherent differences between oxygen detection from fMRI and PAU are more apparent at this sample size.

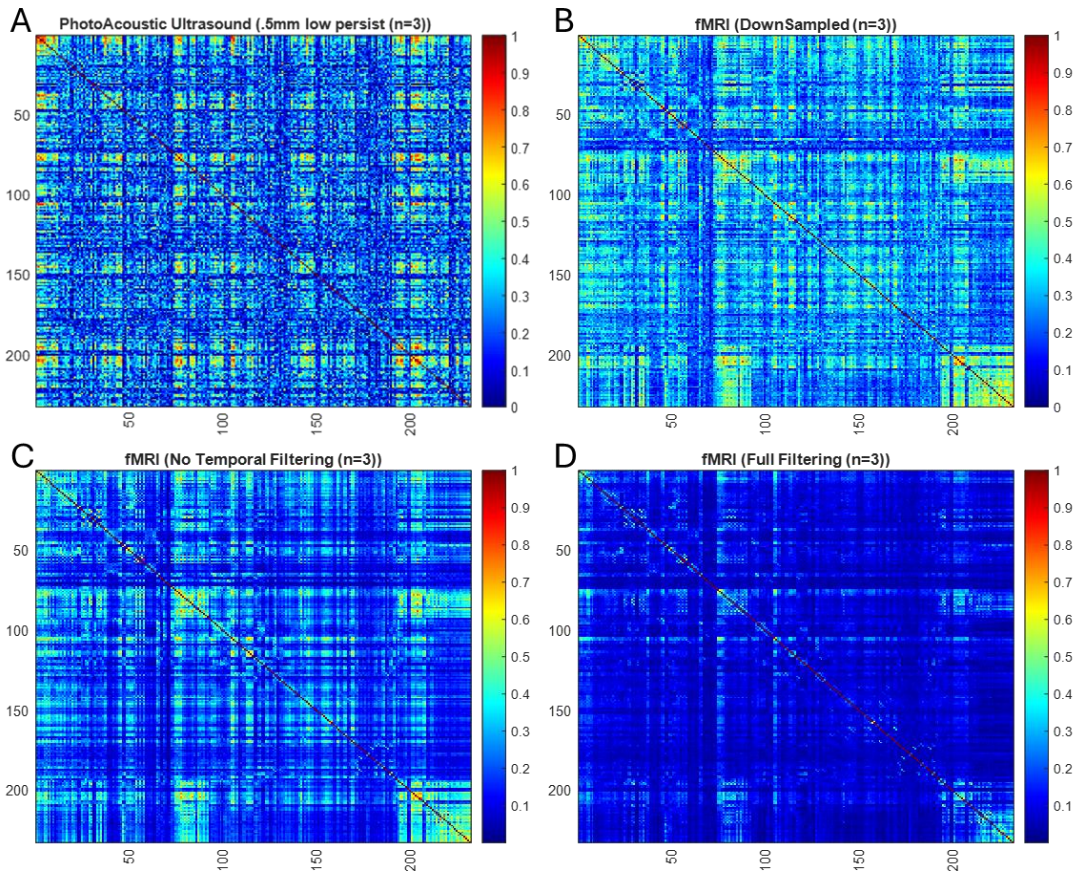

Figure 6.2: Adjacency Connectome Matrices. Generated from alternated scans and processing methods. A: PhotoAcoustic Ultrasound generated Connectome. B: DownSampled fMRI generated connectome. C: Non-Temporally filtered fMRI generated Connectome. D: Fully Filtered fMRI generated Connectome.

6.3.3 Regions of Interest:

The connectomes generated by PAU and fMRI reveal select ROIs with similar connectivity patterns. For instance: the primary motor area (right), Ammon's horn (right), and the periaqueductal gray (right). These connectivity patterns for the specific ROIs are shown in figure 6.3. When analyzing these specific ROIs, we found that all connectomes identified

connectivity between specific ROIs such as the motor cortex and ammon's horn. This supports the known functional connection between these ROIs through the somatomotor network. Of note, the fully filtered fMRI scan showed the least number of connections of the fMRI generated connectomes, indicating that the other fMRI variations may have many false positives. The PAU generated connectome also showed many additional connections that the fMRI did not. Whether these connections are true or not was further evaluated in our literature analysis.

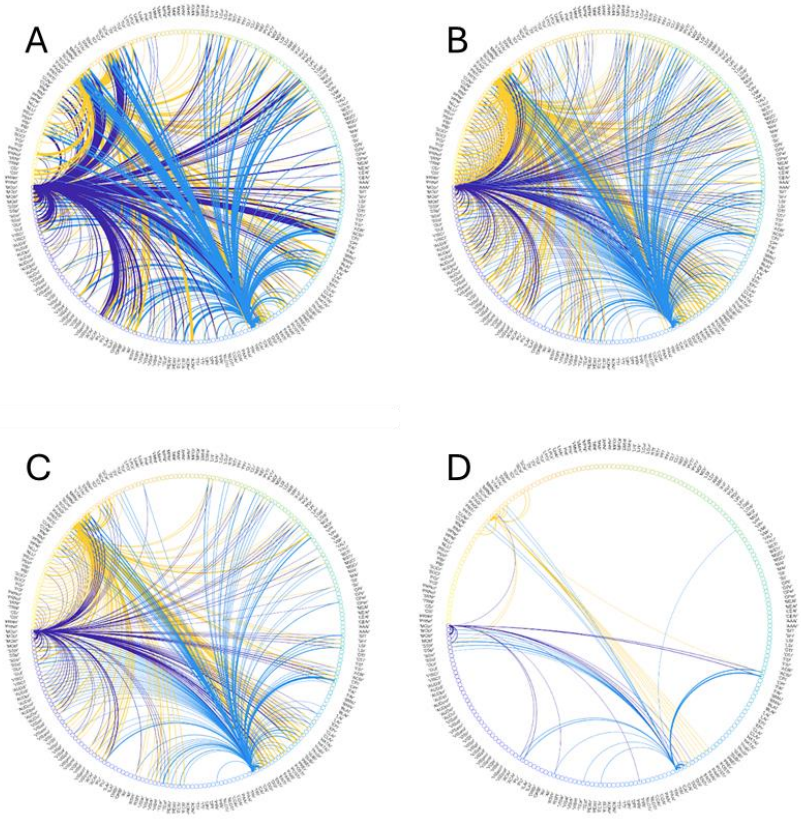

Figure 6.3: Circular Graphs of Areas with High Connectivity. Primary motor area, Ammon's horn, Periaqueductal gray, All graphs show connectivity between the Primary motor area and the Ammon's horn. A: PAU generated circular graph. B: DownSampled fMRI generated circular graph. C: Non-Temporally filtered fMRI generated circular graph. D: Fully Filtered fMRI generated circular graph.

6.3.4 Full Connectome Range:

One limitation often present in fMRI scans is physical range. The fMRI data acquired in this study made use of an RF surface coil in this study to properly transmit and receive the radio waves, which limited the data acquisition area covering the brain. The PAU scan did not have this limitation, and therefore was able to acquire oxygenation signals throughout the entire brain (Figure 6.4). The analysis of these additional ROIs provides the opportunity to further understand the networks throughout the brain and their extent. For the purposes of this paper, the validation of these additional ROIs was saved for future research.

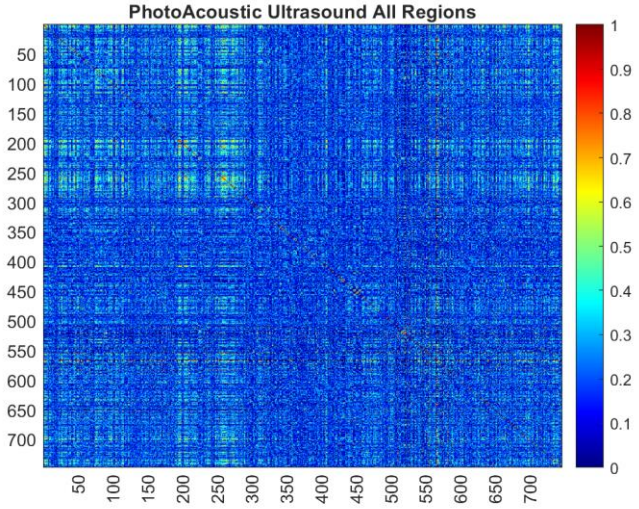

Figure 6.4: Expanded PhotoAcoustic Ultrasound Connectome.

6.3.5 Alternate PAU Acquisition Parameters:

The original parameters of the PAU had a step size of .5mm, sample rate of 1/42 seconds, wavelengths emitted 750nm & 850nm, and low frame averaging (persists). To generate the most accurate PAU connectome, we adjusted these parameters and assessed the resulting errors in comparison with the connectome generated from the fully filtered fMRI scan (Figure 6.5). Low persistence decreased the MSE more than no persistence with the largest difference being present in the .5mm step size scans. By changing the step size,

there was a noted sizable effect on the MSE with the lowest MSE being present on .5mm step size scans. When a wavelength of 850 nm was used rather than 750 and 850 nm, the resulting error was greater. The averaged connectome had the smallest MSE, which is representative of a larger sample size improving the accuracy and reliability of the results.

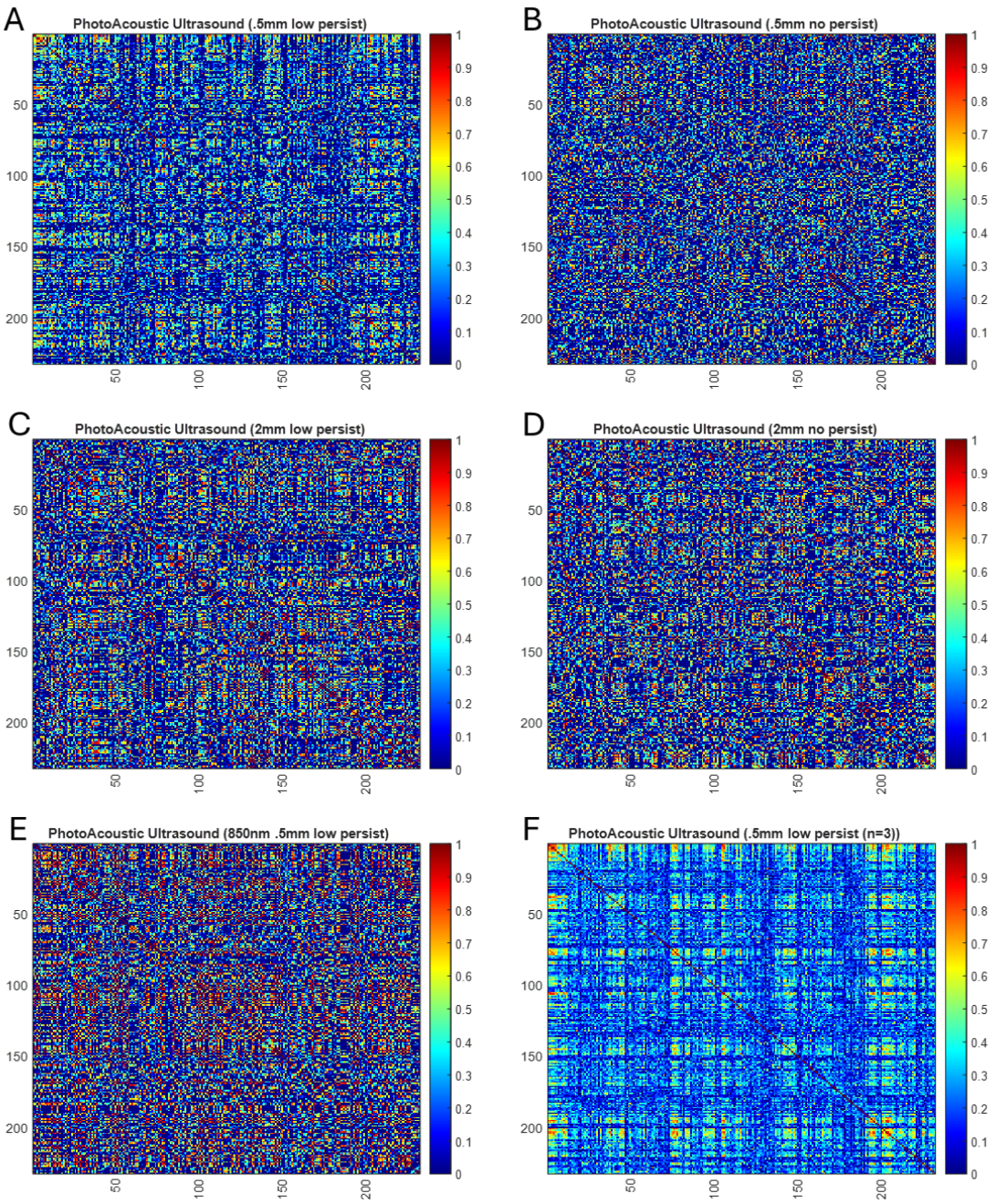

Figure 6.5: PAU Generated Connectome with Alternate Acquisition Parameters. A: 0.5mm step size with low persists. B: 0.5mm step size with no persist. C: 2mm step size with low persists. D: 2mm step size with no persists. E: 0.5mm step size with low persists and only 850nm wavelength emission. F: Average of 3 samples with 0.5mm step size with low persists.

6.3.6 Scientific Literature Analysis:

To assist in ruling out false positives, we conducted a literature review of the more strongly connected PAU ROIs with correlation .6 or greater in Table 6.1. This value was chosen as it allowed us to focus on the highest ~3% of correlation coefficients in the PAU connectome, increasing the confidence of a true connection. Firstly, it was recorded whether the corresponding fMRI correlation coefficient was .2 or greater. This value was chosen, as similarly, it corresponded to the highest ~3% of correlation coefficients in the fMRI connectome. We searched through the Allen Connectivity Atlas to determine if direct connections existed between the suspected ROIs. Additionally, we identified which networks, circuits, loops, or systems the seed and suspected ROIs were associated with and if they both shared any in common. Approximately 85% of the PAU suspected connections had either a corresponding fMRI correlation value greater than .2, projections connecting or passing directly between them according to the Allen Connectivity Atlas, and/or literary research showing a shared functional connection via a shared network. The remaining ~15% of these strong connections were highlighted as either potential false positives or connections that PAU had an increased sensitivity and ability to detect that should be further investigated in future research.

Seed	Connections	PAU-CC	fMRI-CC	Projection Overlap (>=.01)	Shared Network	Connection Reference	Seed Reference
Primary somatosensory area	Supplemental somatosensory area	0.66	0.45	Yes	Somatomotor Network	Disbrow, E., et al 2000	Biswal, B., et al. 1995
[]	Anterior cingulate area	0.79	0.35	Yes	Somatomotor Network	Seeley, William W., et al. 2007	Biswal, B., et al. 1995
[]	Ammon's horn	0.61	0.48	No	Somatomotor Network	Burman, Douglas D. 2019	Biswal, B., et al. 1995

[]	Dentate gyrus	0.66	0.48	No	Somatomotor Network	Burman, Douglas D. 2019	Biswal, B., et al. 1995
[]	Basolateral amygdalar nucleus	0.62	0.13	No	N/A		
[]	Caudoputamen	0.75	0.41	Yes	Somatomotor Network	Calabresi, Paolo, et al. 2007	Biswal, B., et al. 1995
[]	Substantia innominata	0.69	0.19	No	N/A		
[]	Lateral posterior nucleus of the thalamus	0.73	0.24	No	N/A		
[]	Zona incerta	0.67	0.19	Yes	Somatomotor Network	Chometton, Sandrine, et al. 2021	Biswal, B., et al. 1995
[]	Inferior colliculus	0.77	0.28	Yes	Auditory Network	Liu, Mengting, et al. 2024	Wu, Calvin, et al. 2015
[]	Midbrain reticular nucleus	0.69	0.34	Yes	N/A		
[]	Superior colliculus, motor related	0.73	0.29	Yes	Somatomotor Network	Barth, T. M., and T. Schallert. 1987	Biswal, B., et al. 1995
Anterior area	Lateral hypothalamic area	0.66	0.16	No	N/A		
Dorsal peduncular area	Medial amygdalar nucleus	0.61	0.03	Yes	Limbic Network	Botterill, Justin J., et al. 2024	Morgane, Peter J., et al. 2005
Cortical amygdalar area	Lateral hypothalamic area	0.74	0.04	Yes	Limbic Network	Morgane, Peter J., et al. 2005	Morgane, Peter J., et al. 2005
[]	Dentate gyrus	0.66	0.57	Yes	Limbic Network	Morgane, Peter J., et al. 2005	Morgane, Peter J., et al. 2005
[]	Presubiculum	0.60	0.25	No	Limbic Network	O'Mara, Shane. 2005	Morgane, Peter J., et al. 2005
[]	Lateral amygdalar nucleus	0.65	0.13	Yes	Limbic Network	Morgane, Peter J., et al. 2005	Morgane, Peter J., et al. 2005
[]	Caudoputamen	0.65	0.54	Yes	N/A		

[]	Dorsal part of the lateral geniculate complex	0.65	0.26	No	Limbic Network	Botterill, Justin J., et al. 2024	Morgane, Peter J., et al. 2005
[]	Lateral posterior nucleus of the thalamus	0.61	0.30	Yes	Limbic Network	Morgane, Peter J., et al. 2005	Morgane, Peter J., et al. 2005
[]	Zona incerta	0.69	0.26	Yes	N/A		
[]	Superior colliculus, sensory related	0.63	0.16	No	N/A		
[]	Inferior colliculus	0.77	0.17	Yes	Limbic Network	Garcia-Cairasco, Norberto 2002	Morgane, Peter J., et al. 2005
[]	Midbrain reticular nucleus	0.69	0.31	Yes	Limbic Network	Morgane, Peter J., et al. 2005	Morgane, Peter J., et al. 2005
[]	Superior colliculus, motor related	0.75	0.27	No	N/A		
[]	Periaqueductal gray	0.72	0.26	No	Stress Network	Durieux, Laura, et al. 2022	Durieux, Laura, et al. 2022
[]	Pontine reticular nucleus, caudal part	0.64	0.12	No	N/A		
Lateral dorsal nucleus of thalamus	Anterior hypothalamic nucleus	0.69	0.06	No	N/A		
Mediodorsal nucleus of thalamus	Parabrachial nucleus	0.66	0.07	Yes	N/A		
Central lateral nucleus of the thalamus	Parabrachial nucleus	0.63	0.04	Yes	Reward Circuit	Berridge, Kent C., and Morten L. Kringelbach. 2015	Berridge, Kent C., and Morten L. Kringelbach. 2015
[]	Principal sensory nucleus of the trigeminal	0.61	0.05	No	N/A		

[]	Pretectal region	0.86	0.20	Yes	N/A		
[]	Parabrachial nucleus	0.62	0.48	Yes	Reward Circuit	Berridge, Kent C., and Morten L. Kringelbach. 2015	Berridge, Kent C., and Morten L. Kringelbach. 2015
Superior colliculus, motor related	Periaqueductal gray	0.68	0.43	Yes	N/A		
[]	Pretectal region	0.68	0.17	Yes	N/A		
[]	Parabrachial nucleus	0.65	0.14	No	N/A		
[]	Pontine reticular nucleus, caudal part	0.65	0.14	Yes	Somatomotor Network	Tsang, E. W., et al. 2010	Barth, T. M., and T. Schallert. 1987
Periaqueductal gray	Pontine reticular nucleus, caudal part	0.74	0.19	No	N/A		
[]	Superior central nucleus raphe	0.64	0.16	Yes	Autonomic Network	Cersosimo, Maria G., and Eduardo E. Benarroch. 2013	Cersosimo, Maria G., and Eduardo E. Benarroch. 2013
Pretectal region	Parabrachial nucleus	0.60	0.09	No	N/A		
Principal sensory nucleus of the trigeminal	Parabrachial nucleus	0.62	0.43	Yes	Somatomotor Network	Howard, Matthew A., et al. 2011	Hong, Woo Taik, et al. 2019
Parabrachial nucleus	Pontine reticular nucleus, caudal part	0.68	0.39	No	N/A		
[]	Lateral posterior nucleus of the thalamus	0.60	0.20	No	Autonomic Network	Cersosimo, Maria G., and Eduardo E. Benarroch. 2013	Cersosimo, Maria G., and Eduardo E. Benarroch. 2013

[]	Lateral habenula	0.64	0.13	No	N/A		
[]	Inferior colliculus	0.90	0.16	No	N/A		
[]	Midbrain reticular nucleus	0.76	0.21	Yes	N/A		
[]	Superior colliculus, motor related	0.73	0.25	Yes	N/A		
[]	Periaqueductal gray	0.64	0.23	Yes	Autonomic Network	Cersosimo, Maria G., and Eduardo E. Benarroch. 2013	Cersosimo, Maria G., and Eduardo E. Benarroch. 2013
Dentate gyrus	Caudoputamen	0.73	0.50	No	N/A		
	Dorsal part of the lateral geniculate complex	0.60	0.18	No	N/A		
	Lateral posterior nucleus of the thalamus	0.71	0.26	No	N/A		
	Posterior complex of the thalamus	0.68	0.20	No	N/A		
[]	Zona incerta	0.69	0.19	Yes	N/A		
[]	Inferior colliculus	0.76	0.18	No	N/A		
[]	Midbrain reticular nucleus	0.79	0.29	No	N/A		
[]	Superior colliculus, motor related	0.70	0.27	No	N/A		
[]	Pretectal region	0.78	0.28	No	N/A		
Entorhinal area	Superior colliculus, sensory related	0.64	0.12	No	N/A		

Presubiculum	Endopiriform nucleus	0.60	0.06	No	N/A		
[]	Basolateral amygdalar nucleus	0.67	0.06	No	N/A		
[]	Dorsal part of the lateral geniculate complex	0.62	0.04	No	N/A		
[]	Inferior colliculus	0.70	0.20	No	N/A		
[]	Midbrain reticular nucleus	0.65	0.34	No	N/A		
Endopiriform nucleus	Periaqueductal gray	0.63	0.13	No	N/A		
Lateral amygdalar nucleus	Dorsal part of the lateral geniculate complex	0.64	0.13	No	N/A		
Basolateral amygdalar nucleus	Midbrain reticular nucleus	0.63	0.05	Yes	N/A		
Caudoputamen	Substantia innominata	0.60	0.23	Yes	Limbic Network	Vattoth, Surjith, and Sheza Mariya. 2023	Buot, A., and J. Yelnik. 2012
[]	Lateral posterior nucleus of the thalamus	0.83	0.29	No	Limbic Network	Morgane, Peter J., et al. 2005	Buot, A., and J. Yelnik. 2012
[]	Inferior colliculus	0.81	0.14	No	N/A		
[]	Substantia nigra, reticular part	0.60	0.22	Yes	Limbic Network	Mann, Leah G., and Daniel O. Claassen. 2024	Buot, A., and J. Yelnik. 2012
[]	Pretectal region	0.74	0.33	No	N/A		
Nucleus accumbens	Ventral medial nucleus of the thalamus	0.75	0.08	Yes	Reward Circuit	Yager, Lindsay M., et al. 2015	Berridge, Kent C., and Morten L. Kringelbach. 2015

Globus pallidus, external segment	Nucleus of the lateral lemniscus	0.62	0.06	No	N/A		
Ventral medial nucleus of the thalamus	Inferior colliculus	0.66	0.07	No	N/A		
Dorsal part of the lateral geniculate complex	Lateral posterior nucleus of the thalamus	0.62	0.25	Yes	Visual Network	Usrey, W. Martin, and Henry J. Alitto. 2015	Usrey, W. Martin, and Henry J. Alitto. 2015
[]	Midbrain reticular nucleus	0.72	0.09	No	N/A		
Reticular nucleus of the thalamus	Periaqueductal gray	0.66	0.10	No	Pain Matrix	Wu, Dali, et al. 2014	Wu, Dali, et al. 2014
[]	Parabrachial nucleus	0.61	0.06	No	Reward Circuit	Berridge, Kent C., and Morten L. Kringelbach. 2015	Berridge, Kent C., and Morten L. Kringelbach. 2015
[]	Pontine reticular nucleus	0.63	0.05	No	N/A		
Posterior hypothalamic nucleus	Nucleus of the lateral lemniscus	0.62	0.02	No	N/A		
Tuberal nucleus	Superior central nucleus raphe	0.62	0.03	Yes	Autonomic Network	Cersosimo, Maria G., and Eduardo E. Benarroch. 2013	Cersosimo, Maria G., and Eduardo E. Benarroch. 2013
Zona incerta	Inferior colliculus	0.60	0.08	Yes	N/A		
[]	Midbrain reticular nucleus	0.68	0.13	Yes	N/A		
[]	Pretectal region	0.67	0.14	Yes	N/A		

Superior colliculus, sensory related	Inferior colliculus	0.68	0.16	Yes	N/A		
[]	Midbrain reticular nucleus	0.69	0.08	Yes	N/A		
[]	Superior colliculus, motor related	0.83	0.26	Yes	Somatomotor Network	Barth, T. M., and T. Schallert. 1987	Barth, T. M., and T. Schallert. 1987
[]	Periaqueductal gray	0.72	0.15	Yes	N/A		
[]	Red nucleus	0.61	0.03	No	N/A		
[]	Pontine reticular nucleus, caudal part	0.68	0.03	Yes	N/A		
Inferior colliculus	Midbrain reticular nucleus	0.77	0.37	Yes	N/A		
[]	Superior colliculus, motor related	0.88	0.30	Yes	N/A		
[]	Periaqueductal gray	0.73	0.36	Yes	N/A		
Secondary motor area	Primary somatosensory area	0.78	0.27	Yes	Somatomotor Network	Biswal, B., et al. 1995	Biswal, B., et al. 1995
[]	Anterior cingulate area	0.61	0.35	Yes	Somatomotor Network	Barthas, Florent, and Alex C. Kwan. 2017	Biswal, B., et al. 1995
[]	Ammon's horn	0.65	0.34	No	Somatomotor Network	Burman, Douglas D. 2019	Biswal, B., et al. 1995
[]	Dentate gyrus	0.81	0.26	No	Somatomotor Network	Rajmohan, V., and E. Mohandas. 2007	Biswal, B., et al. 1995
[]	Presubiculum	0.67	0.11	No	N/A		
[]	Caudoputamen	0.73	0.38	Yes	Somatomotor Network	Hintiryan, Houri, et al. 2016	Biswal, B., et al. 1995

[]	Ventral posterior complex of the thalamus	0.64	0.13	No	Somatomotor Network	Purves, Dale, et al. 2001	Biswal, B., et al. 1995
Supplemental somatosensory area	Visceral area	0.69	0.29	Yes	N/A		
[]	Anterior cingulate area	0.77	0.21	No	N/A		
[]	Caudoputamen	0.61	0.40	Yes	Somatomotor Network	Parent, André, and Lili-Naz Hazrati. 1995	Biswal, B., et al. 1995
[]	Lateral posterior nucleus of the thalamus	0.66	0.18	No	Somatomotor Network	Foster, Nicholas N., et al. 2021	Biswal, B., et al. 1995
Gustatory areas	Caudoputamen	0.67	0.29	Yes	N/A		
Visceral area	Anterior cingulate area	0.68	0.13	No	Autonomic Network	Cersosimo, Maria G., and Eduardo E. Benarroch. 2013	Cersosimo, Maria G., and Eduardo E. Benarroch. 2013
[]	Caudoputamen	0.63	0.27	Yes	N/A		
[]	Lateral posterior nucleus of the thalamus	0.68	0.13	No	N/A		
[]	Lateral hypothalamic area	0.72	0.12	Yes	Autonomic Network	Cersosimo, Maria G., and Eduardo E. Benarroch. 2013	Cersosimo, Maria G., and Eduardo E. Benarroch. 2013
Primary auditory area	Septofimbrial nucleus	0.64	0.05	No	N/A		
Anterolateral visual area	Lateral visual area	0.70	0.25	Yes	Visual Network	Baker, Cordell M., et al. 2018	Baker, Cordell M., et al. 2018
Anterior cingulate area	Caudoputamen	0.78	0.37	Yes	N/A		

[]	Lateral posterior nucleus of the thalamus	0.74	0.19	Yes	Pain Matrix	Xue, Man, et al. 2022	Xue, Man, et al. 2022
[]	Lateral habenula	0.63	0.16	No	Reward Circuit	Baker, Phillip M., et al. 2016	Baker, Phillip M., et al. 2016
[]	Posterior hypothalamic nucleus	0.63	0.13	Yes	Autonomic Network	Rolls, Edmund T. 2019	Rolls, Edmund T. 2019
[]	Inferior colliculus	0.68	0.13	No	N/A		
[]	Midbrain reticular nucleus	0.64	0.23	Yes	N/A		
[]	Superior colliculus, motor related	0.73	0.22	Yes	Pain Matrix	Shi, Wantong, et al. 2022	
Orbital area	Presubiculum	0.67	0.04	No	Reward Circuit	Martin-Fardon, Rémi, et al. 2008	Berridge, Kent C., and Morten L. Kringelbach. 2015
[]	Endopiriform nucleus	0.69	0.06	Yes	N/A		
[]	Pontine reticular nucleus	0.64	0.03	Yes	N/A		
Agranular insular area	Postsubiculum	0.62	0.13	No	N/A		
[]	Inferior colliculus	0.62	0.12	No	N/A		
[]	Midbrain reticular nucleus	0.62	0.17	No	N/A		
[]	Superior colliculus, motor related	0.67	0.16	No	Visual Network	Liu, Xue, et al. 2022	Liu, Xue, et al. 2022
[]	Pretectal region	0.63	0.20	No	N/A		
Fundus of striatum	Substantia nigra, reticular part	0.69	0.10	No	N/A		
Anterior amygdalar area	Anteroventral nucleus of thalamus	0.65	0.04	No	Reward Circuit	Berridge, Kent C., and Morten	Berridge, Kent C., and Morten

						L. Kringelbach. 2015	L. Kringelbach. 2015
Substantia innominata	Zona incerta	0.72	0.10	Yes	N/A		
[]	Pretectal region	0.62	0.11	No	N/A		
Ventral posterior complex of the thalamus	Tuberal nucleus	0.61	0.10	No	Reward Circuit	Berridge, Kent C., and Morten L. Kringelbach. 2015	Berridge, Kent C., and Morten L. Kringelbach. 2015
Medial geniculate complex	Pedunculopontine nucleus	0.62	0.07	No	N/A		
Lateral posterior nucleus of the thalamus	Lateral hypothalamic area	0.66	0.10	No	Reward Circuit	Berridge, Kent C., and Morten L. Kringelbach. 2015	Berridge, Kent C., and Morten L. Kringelbach. 2015
[]	Inferior colliculus	0.67	0.07	No	N/A		
[]	Midbrain reticular nucleus	0.81	0.12	Yes	N/A		
[]	Superior colliculus, motor related	0.71	0.13	Yes	Visual Network	Liu, Xue, et al. 2022	Usrey, W. Martin, and Henry J. Alitto. 2015
[]	Pretectal region	0.65	0.23	No	N/A		
Primary motor area	Secondary motor area	0.83	0.57	Yes	Somatomotor Network	Biswal, B., et al. 1995	Biswal, B., et al. 1995
[]	Primary somatosensory area	0.80	0.43	Yes	Somatomotor Network	Biswal, B., et al. 1995	Biswal, B., et al. 1995
[]	Gustatory areas	0.70	0.26	Yes	Somatomotor Network	de Araujo, Ivan E., and Sidney A. Simon. 2005	Biswal, B., et al. 1995
[]	Anterior cingulate area	0.80	0.33	Yes	Somatomotor Network	Gordon, Evan M., et al. 2023	Biswal, B., et al. 1995

[]	Ammon's horn	0.65	0.39	Yes	N/A		
[]	Dentate gyrus	0.68	0.36	No	Somatomotor Network	Muñoz-Castañeda, Rodrigo, et al. 2021	Biswal, B., et al. 1995
[]	Caudoputamen	0.86	0.40	Yes	Somatomotor Network	Parent, André, and Lili-Naz Hazrati. 1995	Biswal, B., et al. 1995
[]	Fundus of striatum	0.62	0.14	Yes	Somatomotor Network	Barbier, Marie, et al. 2020	Biswal, B., et al. 1995
[]	Lateral posterior nucleus of the thalamus	0.74	0.20	No	Somatomotor Network	Foster, Nicholas N., et al. 2021	Biswal, B., et al. 1995
[]	Inferior colliculus	0.86	0.22	No	N/A		
[]	Midbrain reticular nucleus	0.71	0.28	Yes	N/A		
[]	Superior colliculus, motor related	0.76	0.30	No	Somatomotor Network	Barth, T. M., and T. Schallert. 1987	Biswal, B., et al. 1995
[]	Ventral posterior complex of the thalamus	0.66	0.09	Yes	Somatomotor Network	Foster, Nicholas N., et al. 2021	Biswal, B., et al. 1995

Table 6.1: Literature Search Results. Column 1 = Seed ROI, Column 2 = Suspected Connected ROI, Column 3 = PAU Correlation Coefficient, Column 4 = fMRI Correlation Coefficient, Column 5 = Existence of projection overlap from seed through/to suspected, Column 6 = Seed and Suspected Connection Shared Network, Column 7 = Reference for Suspected Connection Shared Network, Column 8 = Reference for Seed Shared Network. Highlighted rows represent connections not established by any of the three established routes.

6.4 Discussion:

6.4.1 Mapping & Filtering:

Pipelines exist to map and process fMRI mouse brain data, however a pipeline to map and process ultrasound and photoacoustic data for the purpose of whole-brain connectome generation has not previously been established. In this project we established that nearly the same pipeline used in fMRI mapping can be used to map and process PAU and ultrasound data; with the exception of temporal filtering and an additional step of converting exported .tif files to a single .nii file. This pipeline could be further streamlined for PAU and ultrasound data by extracting the SPM scripts used and implementing them into a single program. The segmentation process of the ultrasound data also has the potential to be automated if an appropriate artificial intelligence model was trained.

6.4.2 Functional Connectome:

Our analysis of connectomes generated from fMRI compared to PAU revealed that the greatest similarities were present between the non-temporally filtered fMRI connectome and the PAU connectome. This suggests that, due to the inability to temporally filter the PAU data, the resulting connectome has similar false positives to the non-temporally filtered fMRI data that are present due to motion and low wavelength fluctuations. Additionally, the PAU connectome identified stronger and more functional connections. This difference may be due to the inherent nature of how oxygenation levels are detected in fMRI vs PAU. The fMRI only detects how the presence or absence of deoxyhemoglobin affects the MR signal, while PAU detects a signal change directly from deoxyhemoglobin and a separate signal change directly from oxyhemoglobin. The detection difference may give PAU a slight advantage in accuracy, which could account for the additional identified connections.

This fMRI mapping was limited in its physical range owing to the use of an RF surface coil which prevented analysis of more comprehensive brain activity. PAU also on the other hand does not require a surface coil for signal transmission and reception, and as such is not limited to acquisitions in those areas. The expanded view PAU offers allows for greater investigation into the brain networks inaccessible to many fMRI setups. The validation of these additional ROIs is crucial for confirming the accuracy and consistency of the PAU generated connectomes. This will be done in future research through additional literature review and alternate coil positions or improved coil ranges for fMRI acquisition.

The alternate parameter experiments revealed that, with the present technology, a step size of 0.5mm with low persists and both 750 nm and 850 nm emissions is able to provide optimal scans for connectome generation. The parameters that stand to see the greatest improvement when comparing PAU to fMRI is the sampling rate and temporal sample size. The difference in sampling rate between 1/42 Hz to 1 Hz prevented temporal filtering on the PAU data and introduced a large margin of error. The relevant brain activity frequencies for functional connectivity range from 0-0.1Hz (Cordes, Dietmar, et al. 2001). Thus, this ultrasound approach is only gathering the lower relevant frequencies and not the full range. If the sampling rate could be increased to a minimum of 1/5 Hz, all of the relevant frequencies could be adequately captured and temporal filtering could be performed. With an increase such as that, we would expect the elimination of many potential false positives resulting from motion or high frequency noise that could previously not be filtered.

6.4.3 Scientific Literature Review:

Our literature review confirmed the existence of functional connectivity between many of the strong connections identified with PAU. Similar to the findings of Zhang et al. and

Nasiriavanaki et al., our research strongly suggests that PAU is a viable approach for the generation of brain connectomes. The connections that could not be confirmed through the corresponding fMRI data, physical connections, or functional connectivity in literature suggest the possibility of previously unidentified connections or false positives. These connections could be further researched through experiments using fMRI with greater spatial resolution and increased sensitivity, additional PAU experiments with larger sample sizes, and PAU experiments with improved acquisition parameters such as faster sampling rate.

6.5 Conclusion:

In conclusion, we have successfully established a pipeline for mapping and processing PAU data for the intended purpose of connectome generation similar to existing pipelines used for fMRI data. Our analysis demonstrated that the PAU generated connectomes, which modeled the entire brain, were comparable to fMRI connectomes. They most closely resembled connectomes derived from non-temporally filtered fMRI. That resemblance is indicative of similar false positives present in both data forms due to motion and low frequency noise that was not filtered out. PAU identified many connections that fMRI did not, and these connections were verified through literary research of several previously studied and recorded functional connections. This ability of PAU to detect connections established in literature that our fMRI data could not is likely due to an increased or alternate form of sensitivity via PAU's dual detection of deoxyhemoglobin and oxyhemoglobin signals. Additionally, PAU's lack of reliance on a surface coil enabled a broader physical range that can be used for more comprehensive brain connectome analysis. Future research of this modality as a viable alternative to fMRI should focus on the validation of the connections identified in PAU, the optimization and improvement of

sampling rates, literature review of PAU connections beyond the physical range of our fMRI scan, and alternate experimental setups further comparing PAU and fMRI. Our findings strongly suggest that PAU is a viable alternative approach for generation of brain connectomes, with the potential to uncover previously unidentified functional connections and allow for more comprehensive brain analysis than traditional fMRI methodologies.

Chapter 7: Conclusion/Discussion

7.1 Summary of Results:

This thesis showed beneficial neurological effects of NeuroD1 based treatments in both TBI and stroke models. This was achieved through use of TBI and stroke animal models and administration of viral mediated treatments to promote NeuroD1 production. We found that anatomical structure was largely unaffected by the treatment, suggesting that restoration of brain architecture was not necessary for the functional recovery that was observed. Additionally, we demonstrated the importance of optimizing parameters for these treatments, with the dose in particular being a crucial consideration. Specifically, if targeting astrocytes, doses of 10^11 GC/mL improve specificity of virus transduction.

We developed a novel ex vivo ultrasound approach to TBI lesion quantification. This was done through the use of a Vevo 2100, 3D Slicer software, in-house generated matlab scripts, and SPM software. This method was shown to be faster than existing techniques while still retaining consistent comparable results. In addition, this method provided the benefit of a 3D model, which could be used to further specify the regions damaged.

Lastly, we developed a pipeline to generate brain connectomes from whole brain PAU scans. This was done through acquisition with a Vevo F2 LAZR-X ultrasound, compared with an MRI with 9.4 T magnet, processing with 3D slicer, in-house matlab scripts, and SPM software. Through an extensive literature review, we confirmed ~85% of the strong connections identified with PAU could be found in prior literature.

7.2 Limitations and Future Directions of Research:

This thesis had numerous limitations that should be considered when viewing the results and determining future directions. The dose used in the neuroprotection mouse TBI

models was of levels that prior literature suggested to be toxic in cells. As such the results may be hindered with decreased transduction specificity. Additionally, the behavior tests for the mouse TBI models assessed general neurological function rather than specific deficits, which limited what specific conclusions could be drawn from the results. Furthermore, the tests used to assess recovery in cell reprogramming mouse TBI models were not the same between low and high dose treatments. As such direct comparison between the benefits of the different dose treatments in this model is not yet possible. Future work should include additional behavioral tests to assess more specific neurological functions, retrograde labeling to assess transduction specificity, cell death analysis to determine presence if toxicity due to the high dose increases apoptosis in the samples, as well as consistent tests across alternate dose experiments to ensure proper comparison.

In the canine stroke models, the sample size was insufficient to obtain any statistically significant results. Similar to some of the mouse TBI model studies, the dose in this study was higher, which could reduce cell transduction specificity and increase apoptosis. For future work, optimization of parameters should be considered as well as a larger sample size should be used to ensure significant differences.

In the TBI lesion quantification studies, the method was only assessed with general neurological deficits, and compared only to microscopy. Future studies should further validate this method across alternate lesion quantification routes and assess more specific neurological deficits to confirm what correlations exist between regions damaged and deficits observed.

Lastly, for the PAU studies, the sample size of standard PAU and fMRI analyzed animals was three per group and standard deviation was not calculated for each correlation. The sampling frequency was also much slower in the PAU scans compared

to the fMRI scans which could lead to an increase in false positives. These issues should be addressed with future research using larger sample sizes and technological advances allowing for faster sampling rates.

7.3 Conclusion:

This thesis showed potential benefits of NeuroD1 based treatments while emphasizing the importance of parameter optimization. Additionally, our research developed novel pipelines that can be used to further improve efficiency of TBI related research and allow greater accessibility to whole brain connectome analysis. This study has provided invaluable contributions that can be used to further the research of treatments and diagnosis methods for ABI's.

References:

1. (Feigin, Valery L., et al. 2010) Feigin, Valery L., et al. “Epidemiology of Ischaemic Stroke and Traumatic Brain Injury.” *Best Practice & Research Clinical Anaesthesiology*, vol. 24, no. 4, Dec. 2010, pp. 485–94. *ScienceDirect*, https://doi.org/10.1016/j.bpa.2010.10.006.
2. (Goldman, Liam, et al. 2022) Goldman, Liam, et al. “Understanding Acquired Brain Injury: A Review.” Biomedicines, vol. 10, no. 9, Sept. 2022, p. 2167. PubMed Central, https://doi.org/10.3390/biomedicines10092167.
3. (Tsao CW, Aday AW, Almarzooq ZI, et al. 2023). Tsao CW, Aday AW, Almarzooq ZI, et al. Heart disease and stroke statistics—2023 update: a report from the American Heart Association. Circulation. 2023;147:e93–e621.
4. (Taylor, Christopher A. 2017). Taylor, Christopher A. “Traumatic Brain Injury–Related Emergency Department Visits, Hospitalizations, and Deaths — United States, 2007 and 2013.” MMWR. Surveillance Summaries, vol. 66, 2017. www.cdc.gov, https://doi.org/10.15585/mmwr.ss6609a1.
5. (Jain, Shobhit, and Lindsay M. Iverson. 2025). Jain, Shobhit, and Lindsay M. Iverson. “Glasgow Coma Scale.” StatPearls, StatPearls Publishing, 2025. PubMed, http://www.ncbi.nlm.nih.gov/books/NBK513298/.
6. (Steyerberg, Ewout W., et al. 2008). Steyerberg, Ewout W., et al. “Predicting Outcome after Traumatic Brain Injury: Development and International Validation of Prognostic Scores Based on Admission Characteristics.” PLoS Medicine, edited by Mervyn Singer, vol. 5, no. 8, Aug. 2008, p. e165. DOI.org (Crossref), https://doi.org/10.1371/journal.pmed.0050165.
7. (“Traumatic Brain Injury in Adults”). “Traumatic Brain Injury in Adults.” American Speech-Language-Hearing Association, American Speech-Language-Hearing Association, https://www.asha.org/practice-portal/clinical-topics/traumatic-brain-injury-in-adults/?srsltid=AfmBOoplRoC2KNW9LgjhEsRW__xHN3dG0eTwnRPsJlsfkYbTcFduPDO1. Accessed 10 Feb. 2025.
8. (Frey, Lauren C. 2003). Frey, Lauren C. “Epidemiology of Posttraumatic Epilepsy: A Critical Review.” Epilepsia, vol. 44, no. s10, 2003, pp. 11–17. Wiley Online Library, https://doi.org/10.1046/j.1528-1157.44.s10.4.x.
9. (Dewan, Michael C., et al. 2018). Dewan, Michael C., et al. Estimating the Global Incidence of Traumatic Brain Injury. Apr. 2018. thejns-org.ezp3.lib.umn.edu, https://doi.org/10.3171/2017.10.JNS17352.
10. (Najem, Dema, et al. 2018). Najem, Dema, et al. “Traumatic Brain Injury: Classification, Models, and Markers.” Biochemistry and Cell Biology, vol. 96, no. 4, Aug. 2018, pp. 391–406. cdnsciencepub-com.ezp3.lib.umn.edu (Atypon), https://doi.org/10.1139/bcb-2016-0160.
11. (Dheen, S. Thameem, et al. 2007). Dheen, S. Thameem, et al. “Microglial Activation and Its Implications in the Brain Diseases.” Current Medicinal Chemistry, vol. 14, no. 11, 2007, pp. 1189–97. PubMed, https://doi.org/10.2174/092986707780597961.
12. (Mesfin, Fassil B., et al. 2025). Mesfin, Fassil B., et al. “Diffuse Axonal Injury.” StatPearls, StatPearls Publishing, 2025. PubMed, http://www.ncbi.nlm.nih.gov/books/NBK448102/.

13. (Wang, Fei, et al. 2023). Wang, Fei, et al. “Gliotransmission and Adenosine Signaling Promote Axon Regeneration.” Developmental Cell, vol. 58, no. 8, Apr. 2023, pp. 660-676.e7. www.cell.com, https://doi.org/10.1016/j.devcel.2023.03.007.
14. (Yiu, Glenn, and Zhigang He. 2006). Yiu, Glenn, and Zhigang He. “Glial Inhibition of CNS Axon Regeneration.” Nature Reviews. Neuroscience, vol. 7, no. 8, Aug. 2006, pp. 617–27. PubMed Central, https://doi.org/10.1038/nrn1956.
15. (Conforti, Laura, et al. 2014). Conforti, Laura, et al. “Wallerian Degeneration: An Emerging Axon Death Pathway Linking Injury and Disease.” Nature Reviews. Neuroscience, vol. 15, no. 6, June 2014, pp. 394–409. PubMed, https://doi.org/10.1038/nrn3680.
16. (Mckee, Ann C., and Daniel H. Daneshvar., 2015). MCKEE, ANN C., and DANIEL H. DANESHVAR. “The Neuropathology of Traumatic Brain Injury.” Handbook of Clinical Neurology, vol. 127, 2015, pp. 45–66. PubMed Central, https://doi.org/10.1016/B978-0-444-52892-6.00004-0.
17. (Bangar, Annu, et al. 2024). Bangar, Annu, et al. “Understanding Mechanistic Aspect of the Therapeutic Role of Herbal Agents on Neuroplasticity in Cerebral Ischemic-Reperfusion Injury.” Journal of Ethnopharmacology, vol. 319, Jan. 2024, p. 117153. ScienceDirect, https://doi.org/10.1016/j.jep.2023.117153.
18. (Ho, Mai-Lan, et al. 2012). Ho, Mai-Lan, et al. “Cerebral Edema.” American Journal of Roentgenology, vol. 199, no. 3, Sept. 2012, pp. W258–73. www-ajronline-org.ezp3.lib.umn.edu (Atypon), https://doi.org/10.2214/AJR.11.8081.
19. (Hochstetler, Alexandra, et al. 2022). Hochstetler, Alexandra, et al. “Hydrocephalus: Historical Analysis and Considerations for Treatment.” European Journal of Medical Research, vol. 27, Sept. 2022, p. 168. PubMed Central, https://doi.org/10.1186/s40001-022-00798-6.
20. (Hayes, Jasmeet P., et al. 2016). Hayes, Jasmeet P., et al. “Traumatic Brain Injury as a Disorder of Brain Connectivity.” Journal of the International Neuropsychological Society : JINS, vol. 22, no. 2, Feb. 2016, pp. 120–37. PubMed Central, https://doi.org/10.1017/S1355617715000740.
21. (Iraji, Armin, et al. 2015). Iraji, Armin, et al. “Resting State Functional Connectivity in Mild Traumatic Brain Injury at the Acute Stage: Independent Component and Seed-Based Analyses.” Journal of Neurotrauma, vol. 32, no. 14, July 2015, pp. 1031–45. PubMed Central, https://doi.org/10.1089/neu.2014.3610.
22. (Knight-Greenfield, Ashley, et al. 2019). Knight-Greenfield, Ashley, et al. “Causes of Acute Stroke.” Radiologic Clinics of North America, vol. 57, no. 6, Nov. 2019, pp. 1093–108. PubMed Central, https://doi.org/10.1016/j.rcl.2019.07.007.
23. (NIH Stroke Scale 2024). NIH Stroke Scale | National Institute of Neurological Disorders and Stroke. https://www.ninds.nih.gov/health-information/stroke/assess-and-treat/nih-stroke-scale. Accessed 17 Feb. 2025.
24. (Kogan, Emily, et al. 2020). Kogan, Emily, et al. “Assessing Stroke Severity Using Electronic Health Record Data: A Machine Learning Approach.” BMC Medical Informatics and Decision Making, vol. 20, Jan. 2020, p. 8. PubMed Central, https://doi.org/10.1186/s12911-019-1010-x.
25. (Ames, A., and F. B. Nesbett. 1983). Ames, A., and F. B. Nesbett. “Pathophysiology of Ischemic Cell Death: I. Time of Onset of Irreversible Damage; Importance of the Different Components of the Ischemic Insult.” Stroke, vol. 14, no. 2, 1983, pp. 219–26. PubMed, https://doi.org/10.1161/01.str.14.2.219.

26. (Mulder, Maxim J. H. L., et al. 2018). Mulder, Maxim J. H. L., et al. “Time to Endovascular Treatment and Outcome in Acute Ischemic Stroke.” Circulation, vol. 138, no. 3, July 2018, pp. 232–40. ahajournals.org (Atypon), https://doi.org/10.1161/CIRCULATIONAHA.117.032600.
27. (Widimsky, Petr, et al. 2022). Widimsky, Petr, et al. “Acute Ischaemic Stroke: Recent Advances in Reperfusion Treatment.” European Heart Journal, vol. 44, no. 14, Dec. 2022, pp. 1205–15. PubMed Central, https://doi.org/10.1093/eurheartj/ehac684.
28. (Gao, Zhengliang, et al. 2009). Gao, Zhengliang, et al. “Neurod1 Is Essential for the Survival and Maturation of Adult-Born Neurons.” Nature Neuroscience, vol. 12, no. 9, Sept. 2009, pp. 1090–92. PubMed Central, https://doi.org/10.1038/nn.2385.
29. (Lai, Muhua, et al. 2020). Lai, Muhua, et al. “NeuroD1 Overexpression in Spinal Neurons Accelerates Axonal Regeneration after Sciatic Nerve Injury.” Experimental Neurology, vol. 327, May 2020, p. 113215. ScienceDirect, https://doi.org/10.1016/j.expneurol.2020.113215.
30. (Clark, Isaac H., et al. 2022). Clark, Isaac H., et al. “Cell Reprogramming for Regeneration and Repair of the Nervous System.” Biomedicines, vol. 10, no. 10, Oct. 2022, p. 2598. PubMed Central, https://doi.org/10.3390/biomedicines10102598.
31. (Kim, Woo-Young, et al. 2001). Kim, Woo-Young, et al. “NeuroD-Null Mice Are Deaf Due to a Severe Loss of the Inner Ear Sensory Neurons during Development.” Development (Cambridge, England), vol. 128, no. 3, Feb. 2001, pp. 417–26.
32. (Seo, Seongjin, et al. 2007). Seo, Seongjin, et al. “Neurogenin and NeuroD Direct Transcriptional Targets and Their Regulatory Enhancers.” The EMBO Journal, vol. 26, no. 24, Dec. 2007, pp. 5093–108. PubMed Central, https://doi.org/10.1038/sj.emboj.7601923.
33. (Herculano-Houzel, Suzana. 2014). Herculano-Houzel, Suzana. “The Glia/Neuron Ratio: How It Varies Uniformly across Brain Structures and Species and What That Means for Brain Physiology and Evolution.” Glia, vol. 62, no. 9, 2014, pp. 1377–91. Wiley Online Library, https://doi.org/10.1002/glia.22683.
34. (Ge, Woo-Ping, et al. 2012). Ge, Woo-Ping, et al. “Local Generation of Glia Is a Major Astrocyte Source in Postnatal Cortex.” Nature, vol. 484, no. 7394, Apr. 2012, pp. 376–80. www.nature.com, https://doi.org/10.1038/nature10959.
35. (Dimou, Leda, and Magdalena Götz. 2014). Dimou, Leda, and Magdalena Götz. “Glial Cells as Progenitors and Stem Cells: New Roles in the Healthy and Diseased Brain.” Physiological Reviews, vol. 94, no. 3, July 2014, pp. 709–37. journals.physiology.org (Atypon), https://doi.org/10.1152/physrev.00036.2013.
36. (Carter, Barrie J. 2004). Carter, Barrie J. “Adeno-Associated Virus and the Development of Adeno-Associated Virus Vectors: A Historical Perspective.” Molecular Therapy, vol. 10, no. 6, Dec. 2004, pp. 981–89. www.cell.com, https://doi.org/10.1016/j.ymthe.2004.09.011.
37. (Hordeaux, Juliette, et al. 2020). Hordeaux, Juliette, et al. “MicroRNA-Mediated Inhibition of Transgene Expression Reduces Dorsal Root Ganglion Toxicity by AAV Vectors in Primates.” Science Translational Medicine, vol. 12, no. 569, Nov. 2020, p. eaba9188. science.org (Atypon), https://doi.org/10.1126/scitranslmed.aba9188.

38. (Friston, Karl J. 1994). Friston, Karl J. “Functional and Effective Connectivity in Neuroimaging: A Synthesis.” Human Brain Mapping, vol. 2, no. 1–2, 1994, pp. 56–78. Wiley Online Library, https://doi.org/10.1002/hbm.460020107.
39. (Johnson, Brian P., and Leonardo G. Cohen. 2023). Johnson, Brian P., and Leonardo G. Cohen. “Chapter 30 - Applied Strategies of Neuroplasticity.” Handbook of Clinical Neurology, edited by David S. Younger, vol. 196, Elsevier, 2023, pp. 599–609. ScienceDirect, https://doi.org/10.1016/B978-0-323-98817-9.00011-9.
40. (Su, YouRong Sophie, et al. 2016). Su, YouRong Sophie, et al. “Neuroplasticity after Traumatic Brain Injury.” Translational Research in Traumatic Brain Injury, CRC Press/Taylor and Francis Group, 2016. www-ncbi-nlm-nih-gov.ezp3.lib.umn.edu, https://www.ncbi.nlm.nih.gov/books/NBK326735/.
41. (Paredes, Mercedes F., et al. 2015). Paredes, Mercedes F., et al. “Brain Size and Limits to Adult Neurogenesis.” The Journal of Comparative Neurology, vol. 524, no. 3, Sept. 2015, p. 646. pmc.ncbi.nlm.nih.gov, https://doi.org/10.1002/cne.23896.
42. (Maas, Andrew I R et al. 2017). Maas, Andrew I R et al. “Traumatic brain injury: integrated approaches to improve prevention, clinical care, and research.” The Lancet. Neurology vol. 16,12 (2017): 987-1048. doi:10.1016/S1474-4422(17)30371-X.
43. (Gao, Zhengliang et al. 2008). Gao, Zhengliang et al. “Neurod1 is essential for the survival and maturation of adult-born neurons.” Nature neuroscience vol. 12,9 (2009): 1090-2. doi:10.1038/nn.2385
44. (Liu, Hong, et al. 2008). Liu, Hong, et al. “NeuroD1 Regulates Expression of Thyroid Hormone Receptor 2 and Cone Opsins in the Developing Mouse Retina.” The Journal of Neuroscience: The Official Journal of the Society for Neuroscience, vol. 28, no. 3, Jan. 2008, pp. 749–56. PubMed, https://doi.org/10.1523/JNEUROSCI.4832-07.2008.
45. (Matsuda-Ito, Kanae et al. 2022). Matsuda-Ito, Kanae et al. “Expression level of the reprogramming factor NeuroD1 is critical for neuronal conversion efficiency from different cell types.” Scientific reports vol. 12,1 17980. 26 Oct. 2022, doi:10.1038/s41598-022-22802-z
46. (Chen, Yu-Chen, et al. 2020). Chen, Yu-Chen et al. “A NeuroD1 AAV-Based Gene Therapy for Functional Brain Repair after Ischemic Injury through In Vivo Astrocyte-to-Neuron Conversion.” Molecular therapy : the journal of the American Society of Gene Therapy vol. 28,1 (2020): 217-234. doi:10.1016/j.ymthe.2019.09.003
47. (Ma, Ning-Xin et al. 2022). Ma, Ning-Xin et al. “Transcriptomic analyses of NeuroD1-mediated astrocyte-to-neuron conversion.” Developmental neurobiology vol. 82,5 (2022): 375-391. doi:10.1002/dneu.22882
48. (Guillemot, François, and Bassem A Hassan. 2017). Guillemot, François, and Bassem A Hassan. “Beyond proneural: emerging functions and regulations of proneural proteins.” Current opinion in neurobiology vol. 42 (2017): 93-101. doi:10.1016/j.conb.2016.11.011
49. (Falk, Sven, and Magdalena Götz. 2017). Falk, Sven, and Magdalena Götz. “Glial Control of Neurogenesis.” Current Opinion in Neurobiology, vol. 47, Dec. 2017, pp. 188–95. PubMed, https://doi.org/10.1016/j.conb.2017.10.025.

50. (Issa, Shaza S., et al. 2023). Issa, Shaza S., et al. “Various AAV Serotypes and Their Applications in Gene Therapy: An Overview.” Cells, vol. 12, no. 5, Mar. 2023, p. 785. PubMed, https://doi.org/10.3390/cells12050785.
51. (Guo, Ziyuan, et al. 2014). Guo, Ziyuan, et al. “In Vivo Direct Reprogramming of Reactive Glial Cells into Functional Neurons after Brain Injury and in an Alzheimer’s Disease Model.” Cell Stem Cell, vol. 14, no. 2, Feb. 2014, pp. 188–202. PubMed, https://doi.org/10.1016/j.stem.2013.12.001.
52. (Pataskar, Abhijeet, et al. 2016). Pataskar, Abhijeet, et al. “NeuroD1 Reprograms Chromatin and Transcription Factor Landscapes to Induce the Neuronal Program.” The EMBO Journal, vol. 35, no. 1, Jan. 2016, pp. 24–45. PubMed Central, https://doi.org/10.15252/embj.201591206.
53. (Kredel, Simone, et al. 2009). Kredel, Simone, et al. “mRuby, a Bright Monomeric Red Fluorescent Protein for Labeling of Subcellular Structures.” PLoS ONE, vol. 4, no. 2, Feb. 2009, p. e4391. PubMed Central, https://doi.org/10.1371/journal.pone.0004391.
54. (Nagy A. 2000). Nagy, A. “Cre Recombinase: The Universal Reagent for Genome Tailoring.” Genesis (New York, N.Y.: 2000), vol. 26, no. 2, Feb. 2000, pp. 99–109.
55. (Dou, Yuanyuan, et al. 2020). Dou, Yuanyuan, et al. “The CAG Promoter Maintains High-level Transgene Expression in HEK293 Cells.” FEBS Open Bio, vol. 11, no. 1, Dec. 2020, pp. 95–104. PubMed Central, https://doi.org/10.1002/2211-5463.13029.
56. (Fedorov, Andriy, et al. 2012). Fedorov, Andriy, et al. “3D Slicer as an Image Computing Platform for the Quantitative Imaging Network.” Magnetic Resonance Imaging, vol. 30, no. 9, Nov. 2012, pp. 1323–41. ScienceDirect, https://doi.org/10.1016/j.mri.2012.05.001.
57. (Lai, Muhua, et al. 2020) Lai, Muhua, et al. “NeuroD1 Overexpression in Spinal Neurons Accelerates Axonal Regeneration after Sciatic Nerve Injury.” Experimental Neurology, vol. 327, May 2020, p. 113215. ScienceDirect, https://doi.org/10.1016/j.expneurol.2020.113215.
58. (Clark, Isaac H., et al. 2024). Clark, Isaac H., et al. “Ex Vivo Method for Rapid Quantification of Post Traumatic Brain Injury Lesion Volumes Using Ultrasound.” Journal of Neuroscience Methods, vol. 407, Apr. 2024, p. 110140. PubMed, https://doi.org/10.1016/j.jneumeth.2024.110140.
59. (Naumann, Thomas, et al. 2000). Naumann, Thomas, et al. “Retrograde Tracing with Fluoro-Gold: Different Methods of Tracer Detection at the Ultrastructural Level and Neurodegenerative Changes of Back-Filled Neurons in Long-Term Studies.” Journal of Neuroscience Methods, vol. 103, no. 1, Nov. 2000, pp. 11–21. ScienceDirect, https://doi.org/10.1016/S0165-0270(00)00292-2.
60. (Johnson, Victoria E., et al. 2013). Johnson, Victoria E., et al. “Inflammation and White Matter Degeneration Persist for Years after a Single Traumatic Brain Injury.” Brain, vol. 136, no. 1, Jan. 2013, pp. 28–42. PubMed Central, https://doi.org/10.1093/brain/aws322.
61. (Bankhead, Peter, et al. 2017). Bankhead, Peter, et al. “QuPath: Open Source Software for Digital Pathology Image Analysis.” Scientific Reports, vol. 7, no. 1, Dec. 2017, p. 16878. www.nature.com, https://doi.org/10.1038/s41598-017-17204-5.
62. (Chen, Gong, et al. 2020). Chen, Gong, et al. Comment on “Rapid and Efficient in Vivo Astrocyte-to-Neuron Conversion with Regional Identity and Connectivity?”

bioRxiv, 3 Sept. 2020, p. 2020.09.02.279273. bioRxiv, https://doi.org/10.1101/2020.09.02.279273.
63. (Xu, Liang, et al. 2022). Xu, Liang, et al. Enhancing NeuroD1 Expression to Convert Lineage-Traced Astrocytes into Neurons. bioRxiv, 24 June 2022, p. 2022.06.21.496971. bioRxiv, https://doi.org/10.1101/2022.06.21.496971.
64. (Tsao, Connie W., et al. 2023). Tsao, Connie W., et al. “Heart Disease and Stroke Statistics—2023 Update: A Report From the American Heart Association.” Circulation, vol. 147, no. 8, Feb. 2023, pp. e93–621. www-ahajournals-org.ezp3.lib.umn.edu (Atypon), https://doi.org/10.1161/CIR.0000000000001123.
65. (Lv, Xianli, et al. 2020). Lv, Xianli, et al. “The Intracranial Vasculature of Canines Represents a Model for Neurovascular Ischemia and Training Residents and Fellows in Endovascular Neurosurgery.” The Neuroradiology Journal, vol. 33, no. 4, Aug. 2020, pp. 292–96. PubMed Central, https://doi.org/10.1177/1971400920920787.
66. (van Strien, Miriam E., et al. 2011). van Strien, Miriam E., et al. “Migrating Neuroblasts in the Adult Human Brain: A Stream Reduced to a Trickle.” Cell Research, vol. 21, no. 11, Nov. 2011, pp. 1523–25. www.nature.com, https://doi.org/10.1038/cr.2011.101.
67. (Cameron, Heather A., and Lucas R. Glover. 2015). Cameron, Heather A., and Lucas R. Glover. “Adult Neurogenesis: Beyond Learning and Memory.” Annual Review of Psychology, vol. 66, Jan. 2015, pp. 53–81. PubMed, https://doi.org/10.1146/annurev-psych-010814-015006.
68. (Peng, Zhouzhou, et al. 2022). Peng, Zhouzhou, et al. “Astrocyte Reprogramming in Stroke: Opportunities and Challenges.” Frontiers in Aging Neuroscience, vol. 14, May 2022, p. 885707. PubMed Central, https://doi.org/10.3389/fnagi.2022.885707.
69. (Hinderer, Christian, et al. 2018) Hinderer, Christian, et al. “Severe Toxicity in Nonhuman Primates and Piglets Following High-Dose Intravenous Administration of an Adeno-Associated Virus Vector Expressing Human SMN.” *Human Gene Therapy*, vol. 29, no. 3, Mar. 2018, pp. 285–98. *PubMed Central*, https://doi.org/10.1089/hum.2018.015.
70. (Vasquez, Ciro A., et al. 2019). Vasquez, Ciro A., et al. “Development of a Novel Canine Model of Ischemic Stroke: Skull Base Approach with Transient Middle Cerebral Artery Occlusion.” World Neurosurgery, vol. 127, July 2019, pp. e251–60. PubMed, https://doi.org/10.1016/j.wneu.2019.03.082.
71. (Anrather, Josef, and Costantino Iadecola. 2016). Anrather, Josef, and Costantino Iadecola. “Inflammation and Stroke: An Overview.” Neurotherapeutics, vol. 13, no. 4, Oct. 2016, pp. 661–70. PubMed Central, https://doi.org/10.1007/s13311-016-0483-x.
72. (Sayed, Mohammed A., et al. 2020). Sayed, Mohammed A., et al. “Stroke Promotes the Development of Brain Atrophy and Delayed Cell Death in Hypertensive Rats.” Scientific Reports, vol. 10, Nov. 2020, p. 20233. PubMed Central, https://doi.org/10.1038/s41598-020-75450-6.
73. (Zahr, Natalie M., et al. 2013). Zahr, Natalie M., et al. “A Mechanism of Rapidly Reversible Cerebral Ventricular Enlargement Independent of Tissue Atrophy.” Neuropsychopharmacology, vol. 38, no. 6, May 2013, pp. 1121–29. www.nature.com, https://doi.org/10.1038/npp.2013.11.

74. (Heiss, Wolf-Dieter, and Olivier Zaro Weber. 2017). Heiss, Wolf-Dieter, and Olivier Zaro Weber. “Validation of MRI Determination of the Penumbra by PET Measurements in Ischemic Stroke.” Journal of Nuclear Medicine: Official Publication, Society of Nuclear Medicine, vol. 58, no. 2, Feb. 2017, pp. 187–93. PubMed, https://doi.org/10.2967/jnumed.116.185975.
75. (Pekny, Milos, et al. 2014). Pekny, Milos, et al. “The Dual Role of Astrocyte Activation and Reactive Gliosis.” Neuroscience Letters, vol. 565, Apr. 2014, pp. 30–38. ScienceDirect,
76. (Van Wagoner, Nicholas J., et al. 1999). Van Wagoner, Nicholas J., et al. “Interleukin-6 (IL-6) Production by Astrocytes: Autocrine Regulation by IL-6 and the Soluble IL-6 Receptor.” The Journal of Neuroscience, vol. 19, no. 13, July 1999, pp. 5236–44. PubMed Central, https://doi.org/10.1523/JNEUROSCI.19-13-05236.1999.
77. (Xiong, Tianqing, et al. 2022). Xiong, Tianqing, et al. “Interleukin-33 Regulates the Functional State of Microglia.” Frontiers in Cellular Neuroscience, vol. 16, Nov. 2022, p. 1012968. PubMed Central, https://doi.org/10.3389/fncel.2022.1012968.
78. (Niesman, Ingrid R., et al. 2014). Niesman, Ingrid R., et al. “Traumatic Brain Injury Enhances Neuroinflammation and Lesion Volume in Caveolin Deficient Mice.” Journal of Neuroinflammation, vol. 11, no. 1, Mar. 2014, p. 39. BioMed Central, https://doi.org/10.1186/1742-2094-11-39.
79. (Agarwal, Nitin., et al. 2020). Agarwal, Nitin., et al. Traumatic Brain Injury – Causes, Symptoms and Treatments. https://www.aans.org/. 2020.
80. (Mckee, Ann C., and Daniel H. Daneshvar., 2015). MCKEE, ANN C., and DANIEL H. DANESHVAR. “The Neuropathology of Traumatic Brain Injury.” Handbook of Clinical Neurology, vol. 127, 2015, pp. 45–66. PubMed Central, https://doi.org/10.1016/B978-0-444-52892-6.00004-0.
81. (Washington, Patricia M., et al. 2012). Washington, Patricia M., et al. “The Effect of Injury Severity on Behavior: A Phenotypic Study of Cognitive and Emotional Deficits after Mild, Moderate, and Severe Controlled Cortical Impact Injury in Mice.” Journal of Neurotrauma, vol. 29, no. 13, Sept. 2012, pp. 2283–96. PubMed Central, https://doi.org/10.1089/neu.2012.2456.
82. (National Institute of Neurological Disorders and Stroke. 2023). “Huntington’s Disease.” National Institute of Neurological Disorders and Stroke, https://www.ninds.nih.gov/health-information/disorders/huntingtons-disease. Accessed 2 Aug. 2023.
83. (Wattjes, Mikes P., et al. 2015). Wattjes, Mike P., et al. “Evidence-Based Guidelines: MAGNIMS Consensus Guidelines on the Use of MRI in Multiple Sclerosis--Establishing Disease Prognosis and Monitoring Patients.” Nature Reviews. Neurology, vol. 11, no. 10, Oct. 2015, pp. 597–606. PubMed, https://doi.org/10.1038/nrneurol.2015.157.
84. (Alexander, Lisa D., et al. 2010). Alexander, Lisa D., et al. “Correlating Lesion Size and Location to Deficits after Ischemic Stroke: The Influence of Accounting for Altered Peri-Necrotic Tissue and Incidental Silent Infarcts.” Behavioral and Brain Functions : BBF, vol. 6, Jan. 2010, p. 6. PubMed Central, https://doi.org/10.1186/1744-9081-6-6.
85. (Huang, Shiliang, et al. 2021). Huang, Shiliang, et al. “Resting-State Functional Magnetic Resonance Imaging of Interhemispheric Functional Connectivity in

Experimental Traumatic Brain Injury." Neurotrauma Reports, vol. 2, no. 1, 2021, pp. 526–40. PubMed, https://doi.org/10.1089/neur.2021.0023
86. (Ravi, Sakthivel, et al. 2022). Ravi, Sakthivel, et al. Repetitive Mild Traumatic Brain Injury Impairs Resting State fMRI Connectivity and Alters Protein Profile Signaling Networks. bioRxiv, 1 Oct. 2022, p. 2022.09.21.508917. bioRxiv, https://doi.org/10.1101/2022.09.21.508917.
87. (Battaglini, Marco, et al. 2012). Battaglini, Marco, et al. "Evaluating and Reducing the Impact of White Matter Lesions on Brain Volume Measurements." Human Brain Mapping, vol. 33, no. 9, 2012, pp. 2062–71. Wiley Online Library, https://doi.org/10.1002/hbm.21344.
88. (van der Weijden, Chris W. J., et al. 2022). van der Weijden, Chris W. J., et al. "The Effect of Lesion Filling on Brain Network Analysis in Multiple Sclerosis Using Structural Magnetic Resonance Imaging." Insights into Imaging, vol. 13, no. 1, Mar. 2022, p. 63. BioMed Central, https://doi.org/10.1186/s13244-022-01198-4.
89. (Macé, Émilie, et al. 2018). Macé, Émilie, et al. "Whole-Brain Functional Ultrasound Imaging Reveals Brain Modules for Visuomotor Integration." Neuron, vol. 100, no. 5, Dec. 2018, pp. 1241-1251.e7. PubMed Central, https://doi.org/10.1016/j.neuron.2018.11.031
90. (Weiss, Nicolas, et al. 2007). Weiss, Nicolas, et al. "Clinical Review: Prognostic Value of Magnetic Resonance Imaging in Acute Brain Injury and Coma." Critical Care, vol. 11, no. 5, Oct. 2007, p. 230. BioMed Central, https://doi.org/10.1186/cc6107.
91. (He, Wen, et al. 2013). He, Wen, et al. "Intraoperative Contrast-Enhanced Ultrasound in Traumatic Brain Surgery." Clinical Imaging, vol. 37, no. 6, 2013, pp. 983–88. PubMed, https://doi.org/10.1016/j.clinimag.2013.08.001.
92. (Arnold, Thomas Campbell, et al. 2023). Arnold, Thomas Campbell, et al. "Low-Field MRI: Clinical Promise and Challenges." Journal of Magnetic Resonance Imaging, vol. 57, no. 1, 2023, pp. 25–44. Wiley Online Library, https://doi.org/10.1002/jmri.28408.
93. (Bazinet, Vincent, et al. 2009). Bazinet, Vincent, et al. "Towards a Biologically Annotated Brain Connectome." Nature Reviews Neuroscience, vol. 24, no. 12, Dec. 2023, pp. 747–60. www.nature.com, https://doi.org/10.1038/s41583-023-00752-3.
94. (Bullmore, Ed, and Olaf Sporns. 2009). Bullmore, Ed, and Olaf Sporns. "Complex Brain Networks: Graph Theoretical Analysis of Structural and Functional Systems." Nature Reviews Neuroscience, vol. 10, no. 3, Mar. 2009, pp. 186–98. www.nature.com, https://doi.org/10.1038/nrn2575.
95. (Fox Michael D. 2018). Fox Michael D. "Mapping Symptoms to Brain Networks with the Human Connectome." New England Journal of Medicine, vol. 379, no. 23, Dec. 2018, pp. 2237–45. Taylor and Francis+NEJM, https://doi.org/10.1056/NEJMra1706158.
96. (Heeger, David J., and David Ress. 2022). Heeger, David J., and David Ress. "What Does fMRI Tell Us about Neuronal Activity?" Nature Reviews Neuroscience, vol. 3, no. 2, Feb. 2002, pp. 142–51. www.nature.com, https://doi.org/10.1038/nrn730.
97. (Joshi, Deepa, and D. S. Mehta. 2022). Joshi, Deepa, and D. S. Mehta. "Recent Trends and Diversity in Ultrasonics." Handbook of Metrology and Applications,

edited by Dinesh K. Aswal et al., Springer Nature, 2022, pp. 1–18. Springer Link, https://doi.org/10.1007/978-981-19-1550-5_43-1.
98. (Wang, Lihong V., and Junjie Yao. 2016). Wang, Lihong V., and Junjie Yao. “A Practical Guide to Photoacoustic Tomography in the Life Sciences.” Nature Methods, vol. 13, no. 8, Aug. 2016, pp. 627–38. www.nature.com, https://doi.org/10.1038/nmeth.3925.
99. (Zerbi, Valerio, et al. 2015). Zerbi, Valerio, et al. “Mapping the Mouse Brain with Rs-fMRI: An Optimized Pipeline for Functional Network Identification.” NeuroImage, vol. 123, Dec. 2015, pp. 11–21. ScienceDirect, https://doi.org/10.1016/j.neuroimage.2015.07.090.
100. (Ogawa, S., et al. 1990). Ogawa, S., et al. “Brain Magnetic Resonance Imaging with Contrast Dependent on Blood Oxygenation.” Proceedings of the National Academy of Sciences of the United States of America, vol. 87, no. 24, Dec. 1990, pp. 9868–72. PubMed, https://doi.org/10.1073/pnas.87.24.9868.
101. (Chen, Chuan, et al 2020). Chen, Chuan, et al. “Point Spread Function Formation in Plane-Wave Imaging: A Theoretical Approximation in Fourier Migration.” IEEE Transactions on Ultrasonics, Ferroelectrics, and Frequency Control, vol. 67, no. 2, Feb. 2020, pp. 296–307. IEEE Xplore, https://doi.org/10.1109/TUFFC.2019.2944191.
102. (Disbrow, E., et al 2000). Disbrow, E., et al. “Somatotopic Organization of Cortical Fields in the Lateral Sulcus of Homo Sapiens: Evidence for SII and PV.” The Journal of Comparative Neurology, vol. 418, no. 1, Feb. 2000, pp. 1–21. PubMed, https://doi.org/10.1002/(sici)1096-9861(20000228)418:1<1::aid-cne1>3.0.co;2-p.
103. (Biswal, B., et al. 1995). Biswal, B., et al. “Functional Connectivity in the Motor Cortex of Resting Human Brain Using Echo-Planar MRI.” Magnetic Resonance in Medicine, vol. 34, no. 4, Oct. 1995, pp. 537–41. PubMed, https://doi.org/10.1002/mrm.1910340409.
104. (Seeley, William W., et al. 2007). Seeley, William W., et al. “Dissociable Intrinsic Connectivity Networks for Salience Processing and Executive Control.” The Journal of Neuroscience: The Official Journal of the Society for Neuroscience, vol. 27, no. 9, Feb. 2007, pp. 2349–56. PubMed, https://doi.org/10.1523/JNEUROSCI.5587-06.2007.
105. (Burman, Douglas D. 2019). Burman, Douglas D. “Hippocampal Connectivity with Sensorimotor Cortex during Volitional Finger Movements: Laterality and Relationship to Motor Learning.” PLoS ONE, vol. 14, no. 9, Sept. 2019, p. e0222064. PubMed Central, https://doi.org/10.1371/journal.pone.0222064.
106. (Calabresi, Paolo, et al. 2007). Calabresi, Paolo, et al. “Dopamine-Mediated Regulation of Corticostriatal Synaptic Plasticity.” Trends in Neurosciences, vol. 30, no. 5, May 2007, pp. 211–19. PubMed, https://doi.org/10.1016/j.tins.2007.03.001.
107. (Chometton, Sandrine, et al. 2021). Chometton, Sandrine, et al. “Chapter 11 - The Zona Incerta System: Involvement in Attention and Movement.” Handbook of Clinical Neurology, edited by Dick F. Swaab et al., vol. 180, Elsevier, 2021, pp. 173–84. ScienceDirect, https://doi.org/10.1016/B978-0-12-820107-7.00011-2.
108. (Wu, Calvin, et al. 2015). Wu, Calvin, et al. “Listening to Another Sense: Somatosensory Integration in the Auditory System.” Cell and Tissue Research,

vol. 361, no. 1, July 2015, pp. 233–50. PubMed Central, https://doi.org/10.1007/s00441-014-2074-7.
109. (Liu, Mengting, et al. 2024). Liu, Mengting, et al. “Research Progress of the Inferior Colliculus: From Neuron, Neural Circuit to Auditory Disease.” Brain Research, vol. 1828, Apr. 2024, p. 148775. ScienceDirect, https://doi.org/10.1016/j.brainres.2024.148775.
110. (Barth, T. M., and T. Schallert. 1987). Barth, T. M., and T. Schallert. “Somatosensorimotor Function of the Superior Colliculus, Somatosensory Cortex, and Lateral Hypothalamus in the Rat.” Experimental Neurology, vol. 95, no. 3, Mar. 1987, pp. 661–78. PubMed, https://doi.org/10.1016/0014-4886(87)90307-4.
111. (Cersosimo, Maria G., and Eduardo E. Benarroch. 2013). Cersosimo, Maria G., and Eduardo E. Benarroch. “Central Control of Autonomic Function and Involvement in Neurodegenerative Disorders.” Handbook of Clinical Neurology, vol. 117, 2013, pp. 45–57. PubMed, https://doi.org/10.1016/B978-0-444-53491-0.00005-5.
112. (Durieux, Laura, et al. 2022). Durieux, Laura, et al. “Functional Brain-Wide Network Mapping during Acute Stress Exposure in Rats: Interaction between the Lateral Habenula and Cortical, Amygdalar, Hypothalamic and Monoaminergic Regions.” The European Journal of Neuroscience, vol. 56, no. 8, Oct. 2022, pp. 5154–76. PubMed, https://doi.org/10.1111/ejn.15803.
113. (Foster, Nicholas N., et al. 2021). Foster, Nicholas N., et al. “The Mouse Cortico-Basal Ganglia-Thalamic Network.” Nature, vol. 598, no. 7879, Oct. 2021, pp. 188–94. PubMed, https://doi.org/10.1038/s41586-021-03993-3.
114. (Morgane, Peter J., et al. 2005). Morgane, Peter J., et al. “A Review of Systems and Networks of the Limbic Forebrain/Limbic Midbrain.” Progress in Neurobiology, vol. 75, no. 2, Feb. 2005, pp. 143–60. PubMed, https://doi.org/10.1016/j.pneurobio.2005.01.001.
115. (Buot, A., and J. Yelnik. 2012). Buot, A., and J. Yelnik. “Functional Anatomy of the Basal Ganglia: Limbic Aspects.” Revue Neurologique, vol. 168, no. 8–9, 2012, pp. 569–75. PubMed, https://doi.org/10.1016/j.neurol.2012.06.015.
116. (Botterill, Justin J., et al. 2024). Botterill, Justin J., et al. “Dorsal Peduncular Cortex Activity Modulates Affective Behavior and Fear Extinction in Mice.” Neuropsychopharmacology: Official Publication of the American College of Neuropsychopharmacology, vol. 49, no. 6, May 2024, pp. 993–1006. PubMed, https://doi.org/10.1038/s41386-024-01795-5.
117. (O’Mara, Shane. 2005). O’Mara, Shane. “The Subiculum: What It Does, What It Might Do, and What Neuroanatomy Has yet to Tell Us.” Journal of Anatomy, vol. 207, no. 3, Sept. 2005, pp. 271–82. PubMed, https://doi.org/10.1111/j.1469-7580.2005.00446.x.
118. (Garcia-Cairasco, Norberto 2002). Garcia-Cairasco, Norberto. “A Critical Review on the Participation of Inferior Colliculus in Acoustic-Motor and Acoustic-Limbic Networks Involved in the Expression of Acute and Kindled Audiogenic Seizures.” Hearing Research, vol. 168, no. 1–2, June 2002, pp. 208–22. PubMed, https://doi.org/10.1016/s0378-5955(02)00371-4.
119. (Berridge, Kent C., and Morten L. Kringelbach. 2015). Berridge, Kent C., and Morten L. Kringelbach. “Pleasure Systems in the Brain.” Neuron, vol. 86, no. 3, May 2015, pp. 646–64. PubMed, https://doi.org/10.1016/j.neuron.2015.02.018.

120. (Tsang, E. W., et al. 2010). Tsang, E. W., et al. “Involvement of the Human Pedunculopontine Nucleus Region in Voluntary Movements(e–Pub Ahead of Print).” Neurology, vol. 75, no. 11, Sept. 2010, pp. 950–59. PubMed Central, https://doi.org/10.1212/WNL.0b013e3181f25b35.
121. (Howard, Matthew A., et al. 2011). Howard, Matthew A., et al. “Beyond Patient Reported Pain: Perfusion Magnetic Resonance Imaging Demonstrates Reproducible Cerebral Representation of Ongoing Post-Surgical Pain.” PloS One, vol. 6, no. 2, Feb. 2011, p. e17096. PubMed, https://doi.org/10.1371/journal.pone.0017096.
122. (Hong, Woo Taik, et al. 2019). Hong, Woo Taik, et al. “Trigeminal Somatosensory Evoked Potential Test as an Evaluation Tool for Infraorbital Nerve Damage.” Archives of Craniofacial Surgery, vol. 20, no. 4, Aug. 2019, pp. 223–27. PubMed Central, https://doi.org/10.7181/acfs.2019.00234.
123. (Vattoth, Surjith, and Sheza Mariya. 2023). Vattoth, Surjith, and Sheza Mariya. “Practical Microscopic Neuroanatomy of the Limbic System and Basal Forebrain Identifiable on Clinical 3T MRI.” The Neuroradiology Journal, vol. 36, no. 5, Oct. 2023, pp. 506–14. PubMed, https://doi.org/10.1177/19714009221122250.
124. (Mann, Leah G., and Daniel O. Claassen. 2024). Mann, Leah G., and Daniel O. Claassen. “Mesial Temporal Dopamine: From Biology to Behaviour.” The European Journal of Neuroscience, vol. 59, no. 6, Mar. 2024, pp. 1141–52. PubMed, https://doi.org/10.1111/ejn.16209.
125. (Yager, Lindsay M., et al. 2015). Yager, Lindsay M., et al. “The Ins and Outs of the Striatum: Role in Drug Addiction.” Neuroscience, vol. 301, Aug. 2015, pp. 529–41. PubMed Central, https://doi.org/10.1016/j.neuroscience.2015.06.033.
126. (Usrey, W. Martin, and Henry J. Alitto. 2015). Usrey, W. Martin, and Henry J. Alitto. “Visual Functions of the Thalamus.” Annual Review of Vision Science, vol. 1, Nov. 2015, pp. 351–71. PubMed Central, https://doi.org/10.1146/annurev-vision-082114-035920.
127. (Wu, Dali, et al. 2014). Wu, Dali, et al. “Reciprocal Interactions between the Human Thalamus and Periaqueductal Gray May Be Important for Pain Perception.” Experimental Brain Research, vol. 232, no. 2, Feb. 2014, pp. 527–34. PubMed, https://doi.org/10.1007/s00221-013-3761-4.
128. (Barthas, Florent, and Alex C. Kwan. 2017). Barthas, Florent, and Alex C. Kwan. “Secondary Motor Cortex: Where ‘Sensory’ Meets ‘Motor’ in the Rodent Frontal Cortex.” Trends in Neurosciences, vol. 40, no. 3, Mar. 2017, pp. 181–93. PubMed Central, https://doi.org/10.1016/j.tins.2016.11.006.
129. (Rajmohan, V., and E. Mohandas. 2007). Rajmohan, V., and E. Mohandas. “The Limbic System.” Indian Journal of Psychiatry, vol. 49, no. 2, Apr. 2007, pp. 132–39. PubMed, https://doi.org/10.4103/0019-5545.33264.
130. (Hintiryan, Houri, et al. 2016). Hintiryan, Houri, et al. “The Mouse Cortico-Striatal Projectome.” Nature Neuroscience, vol. 19, no. 8, Aug. 2016, pp. 1100–14. PubMed Central, https://doi.org/10.1038/nn.4332.
131. (Purves, Dale, et al. 2001). Purves, Dale, et al. “The Nociceptive Components of the Thalamus and Cortex.” Neuroscience. 2nd Edition, Sinauer Associates, 2001. www.ncbi.nlm.nih.gov, https://www.ncbi.nlm.nih.gov/books/NBK10997/.

132. (Parent, André, and Lili-Naz Hazrati. 1995). Parent, André, and Lili-Naz Hazrati. “Functional Anatomy of the Basal Ganglia. I. The Cortico-Basal Ganglia-Thalamo-Cortical Loop.” Brain Research Reviews, vol. 20, no. 1, Jan. 1995, pp. 91–127. ScienceDirect, https://doi.org/10.1016/0165-0173(94)00007-C.
133. (Baker, Cordell M., et al. 2018). Baker, Cordell M., et al. “A Connectomic Atlas of the Human Cerebrum—Chapter 9: The Occipital Lobe.” Operative Neurosurgery, vol. 15, no. suppl_1, Dec. 2018, p. S372. journals.lww.com, https://doi.org/10.1093/ons/opy263.
134. (de Araujo, Ivan E., and Sidney A. Simon. 2005). de Araujo, Ivan E., and Sidney A. Simon. “The Gustatory Cortex and Multisensory Integration.” International Journal of Obesity (2005), vol. 33, no. Suppl 2, June 2009, pp. S34–43. PubMed Central, https://doi.org/10.1038/ijo.2009.70.
135. (Xue, Man, et al. 2022). Xue, Man, et al. “Mapping Thalamic-Anterior Cingulate Monosynaptic Inputs in Adult Mice.” Molecular Pain, vol. 18, Apr. 2022, p. 17448069221087034. PubMed Central, https://doi.org/10.1177/17448069221087034.
136. (Baker, Phillip M., et al. 2016). Baker, Phillip M., et al. “The Lateral Habenula Circuitry: Reward Processing and Cognitive Control.” The Journal of Neuroscience, vol. 36, no. 45, Nov. 2016, pp. 11482–88. PubMed Central, https://doi.org/10.1523/JNEUROSCI.2350-16.2016.
137. (Rolls, Edmund T. 2019). Rolls, Edmund T. “The Cingulate Cortex and Limbic Systems for Emotion, Action, and Memory.” Brain Structure & Function, vol. 224, no. 9, 2019, pp. 3001–18. PubMed Central, https://doi.org/10.1007/s00429-019-01945-2.
138. (Shi, Wantong, et al. 2022). Shi, Wantong, et al. “Whole-Brain Mapping of Efferent Projections of the Anterior Cingulate Cortex in Adult Male Mice.” Molecular Pain, vol. 18, May 2022, p. 17448069221094529. PubMed Central, https://doi.org/10.1177/17448069221094529.
139. (Liu, Xue, et al. 2022). Liu, Xue, et al. “The Superior Colliculus: Cell Types, Connectivity, and Behavior.” Neuroscience Bulletin, vol. 38, no. 12, Apr. 2022, pp. 1519–40. PubMed Central, https://doi.org/10.1007/s12264-022-00858-1.
140. (Gordon, Evan M., et al. 2023). Gordon, Evan M., et al. “A Somato-Cognitive Action Network Alternates with Effector Regions in Motor Cortex.” Nature, vol. 617, no. 7960, May 2023, pp. 351–59. www.nature.com, https://doi.org/10.1038/s41586-023-05964-2.
141. (Muñoz-Castañeda, Rodrigo, et al. 2021). Muñoz-Castañeda, Rodrigo, et al. “Cellular Anatomy of the Mouse Primary Motor Cortex.” Nature, vol. 598, no. 7879, Oct. 2021, pp. 159–66. PubMed, https://doi.org/10.1038/s41586-021-03970-w.
142. (Barbier, Marie, et al. 2020). Barbier, Marie, et al. “A Basal Ganglia-like Cortical–Amygdalar–Hypothalamic Network Mediates Feeding Behavior.” Proceedings of the National Academy of Sciences of the United States of America, vol. 117, no. 27, July 2020, pp. 15967–76. PubMed Central, https://doi.org/10.1073/pnas.2004914117.
143. (Martin-Fardon, Rémi, et al. 2008). Martin-Fardon, Rémi, et al. “The Dorsal Subiculum Mediates the Acquisition of Conditioned Reinstatement of Cocaine-Seeking.” Neuropsychopharmacology, vol. 33, no. 8, July 2008, pp. 1827–34. www.nature.com, https://doi.org/10.1038/sj.npp.1301589.

144. (Zhang, Pengfei, et al. 2017). Zhang, Pengfei, et al. “High-Resolution Deep Functional Imaging of the Whole Mouse Brain by Photoacoustic Computed Tomography in Vivo.” Journal of Biophotonics, vol. 11, no. 1, 2018, p. e201700024. Wiley Online Library, https://doi.org/10.1002/jbio.201700024.
145. (Nasiriavanaki, Mohammadreza, et al. 2013). Nasiriavanaki, Mohammadreza, et al. “High-Resolution Photoacoustic Tomography of Resting-State Functional Connectivity in the Mouse Brain.” Proceedings of the National Academy of Sciences of the United States of America, vol. 111, no. 1, Dec. 2013, p. 21. pmc-ncbi-nlm-nih-gov.ezp3.lib.umn.edu, https://doi.org/10.1073/pnas.1311868111.
146. (Cordes, Dietmar, et al. 2001). Cordes, Dietmar, et al. “Frequencies Contributing to Functional Connectivity in the Cerebral Cortex in ‘Resting-State’ Data.” AJNR: American Journal of Neuroradiology, vol. 22, no. 7, Aug. 2001, p. 1326.